Fault Detection, Isolation and Identification of Formation Flying Satellites using Wavelet-Entropy and Neural Networks

Farshid Faal

A Thesis
In
The Department
of
Electrical and Computer Engineering

Presented in Partial Fulfillment of the Requirements
For the Degree of Master of Applied Science (Electrical Engineering) at
Concordia University
Montréal, Québec, Canada

April 2013

Concordia University

School of Graduate Studies

This is to certify that the thesis prepared

By: **Farshid Faal**

Entitled: **Fault Detection, Isolation and Identification of Formation Flying Satellites using Wavelet-Entropy and Neural Networks**

and submitted in partial fulfillment of the requirements for the degree of

Master of Applied Science

complies with the regulations of this University and meets the accepted standards with respect to originality and quality.

Signed by the final examining committee:

Prof. Ferhat Khendek _____ Chair

Dr. Ramin Sedaghati _____ External Examiner

Dr. Luiz Lopes _____ Examiner

Prof. Khashayar Khorasani _____ Supervisor

Approved by _____

Chair of Department or Graduate Program Director

_____

Dean of Faculty

Date _____

Abstract

Fault Detection, Isolation and Identification of Formation Flying Satellites using Wavelet-Entropy and Neural Networks

Farshid Faal

The main objective of this thesis is to develop a fault detection, isolation and identification (FDII) scheme based on Wavelet Entropy (WE) and Artificial Neural Network (ANN) for reaction wheels (RW) that are employed as actuators in the attitude control subsystem (ACS) of a satellites to perform the formation flying (FF) missions. In this thesis two FDII approaches are proposed, i) Spacecraft-level fault diagnosis and ii) Formation-level fault diagnosis.

In the "spacecraft-level" fault diagnosis scheme in order to analysis faults, absolute attitude and angular measurements from a satellite are considered as diagnostic signals. In order to detect the fault, the wavelet-entropy technique is employed on diagnostic signals and the sum of the absolute wavelet entropies (SAWE) of the diagnostic signals are obtained and compared with an appropriately selected threshold. If the SAWE passes the threshold the faulty condition is established. In order to isolate the fault in a satellite the angular velocity measurements in a satellite are considered as diagnostic signals and the relative wavelet energy (RWE) of these signals are obtained and compared to a threshold. In our proposed fault identification scheme, the attitude measurements in a satellite are considered and the detail and approximation coefficients of the wavelet signals are obtained and these coefficients are used as inputs to an artificial neural network to identify the type of the fault in a satellite. Using a confusion matrix evaluation system we demonstrate that our spacecraft-level FDII can detect, isolate and identify the high severity faults in a satellite however this scheme cannot detect low severity faults in a satellite.

Our proposed "formation-level" FDII scheme utilizes data collected from the relative attitudes and relative angular velocity measurements of the formation flying satellites. In this fault diagnosis scheme, the relative attitude and relative angular velocity measurements in a satellite with respect to each its neighbor's in a formation are considered as diagnostic signals. In order to detect the fault, the relative attitude measurements in a satellite are considered as diagnostic signals. The wavelet-entropy technique is utilized on diagnostic signals and the SAWEs with respect to each satellite's neighbor are obtained. These SAWEs are then compared with an appropriately selected threshold. The faulty satellite is determined if these SAWEs pass the thresholds. In order to isolate the fault in a faulty satellite, the relative angular velocity measurements are considered as diagnostic signals. The RWE of these signals are obtained and compared to a threshold. In our proposed fault identification scheme, the relative attitude measurements in a satellite are considered as diagnostic signals. In this scheme, the RWEs of the diagnostic signals are obtained and used as inputs to an artificial neural network to identify the type of the fault in a satellite. According to the simulation results, our proposed FDII scheme can detect, isolate and identified both low severity and high severity faults in the reaction wheels of satellite.

Acknowledgments

It is with immense gratitude that I acknowledge the help of my Professor Dr. K. Khorasani for his direction with this research. I would also like to thank my parents for their unending love and support.

Contents

List of Figures

List of Tables

Chapter 1

Introduction

1.1 Statement of the Problem

The concept and associated challenges of spacecraft flying in formation have been studied since the early days of the space program. Only recently, however, has the idea of formation flying been applied to autonomous satellites [1,2,3,4,5,6,7,8]. The development of multiple cooperating spacecraft has the potential to significantly expand the functionality, performance and reduce the overall operational costs. For instance, a formation of interferometric imaging spacecraft can achieve an optical imaging system with an aperture of kilometers long yielding the resolution that is required to image planets in the other solar systems.

A formation of small satellites would be cheaper to develop and launch, but could still perform the tasks of a large, single satellite mission through proper task distribution [9,10,11,12,13,14,15,16]. The system would exhibit gradual performance degradations as individual satellites fail and tasks are redistributed, rather than the total mission termination that is faced by single satellites during component failures.

By adding inexpensive replacement satellites, the cluster could be returned to full mission specifications. In addition, reconfiguring the relative positions of the constituent satellites in situ would permit a formation to engage in multiple mission objectives. Finally, the capability of obtaining multiple simultaneous measurements along a large baseline would enable satellite formations to accomplish goals that are

difficult or impossible to achieve with a single satellite [100].

There are a number of formation flying missions for deep space environment (such as ST-3, TPF, LISA, DARWIN [17,18,19] and formation flying missions for near-Earth environment (EO-1, ION-F, PRISMA, CLS3, SMART-2 [19,20,21,22,23,24,25]). In formation flying spacecraft, precise formation keeping during the execution of the mission and collision avoidance between the agents of the formation during maneuvers are some of the important and critical issues that must be considered in all missions. These issues can be fulfilled with appropriate control laws and precise sensors and actuators.

However, malfunction of any of these components can affect the performance of the formation. Thus, early detection of faults is mandatory for this type of mission. In general, faults are defined as deviations from the normal behavior in the plant or its instruments. A fault detection system is making a binary decision that indicates the system is working in normal (healthy) condition or something is going wrong with the monitored system. Fault isolation is determination of the location of a fault in the monitored system and fault identification determine and identify type of the fault in a monitored system. A system with detection, isolation and identification capabilities is known as Fault Detection, Isolation and Identification (FDII) system.

FDII systems for attitude control subsystems of spacecraft have been developed in the past decade. There are different approaches that have been developed in the literatures on FDII systems for faulty components such as sensors, actuators and controllers ([25,26,27,28,29,30,31,32]).

However, majority of these works have been developed on a single spacecraft and there is not as much as works on FDII for formation flying spacecraft in literatures. Since there are complexities that are involved with formation flying missions, there is an important area of research regarding the FDII in spacecraft formation flying.

In this thesis, FDII problem in spacecraft formation flying is considered in two levels, spacecraft-level and formation-level fault diagnosis. In spacecraft-level fault diagnosis, FDII is related to subsystem component fault diagnosis. Typically, subsystem components are the sensors and actuators within the subsystems. For instance,

in the case of attitude control subsystem, reaction wheels, thrusters, and attitude sensors are the components. Our proposed spacecraft-level FDII, detects faults in the reaction wheel actuator in a satellite and isolate the faulty reaction wheel in a satellite and also identifies th type of faults in the reaction wheel.

The formation-level FDII is unique to multi-platform missions. Individual spacecraft in the formation are considered as different "components" of the formation flying system. Therefore, at this level, fault detection is essentially the binary decision making about whether or not any fault exist in the formation components, i.e., in one or more satellites in the formation. Consequently, the objective of fault isolation, in this level, is to identify particular spacecraft that are faulty. In our proposed formation-level fault diagnosis, fault in the formation platform will be detected and faulty satellite will be isolated, then the faulty reaction wheel in that satellite is isolated and the type of fault in the reaction wheel will be identified as well.

In our proposed spacecraft-level FDII scheme, the absolute attitude measurements in each satellite are considered as diagnostic signals. We will show that spacecraft-level FDII can only detect and isolate high severity faults in the reaction wheel and low severity faults can not detect in this FDII scheme. Hence, we will propose the formation-level FDII scheme. In this scheme, the relative attitude measurements in one satellite with respect to each of its neighbors in a formation are considered as diagnostic signals. We will show that this FDII scheme can detect and isolate both high severity and low severity faults in the reaction wheel actuator in a satellite.

There are different types of sensors and actuators that are utilized in the spacecraft that depend on the mission objectives. For attitude maneuvers, magnetic torque, reaction wheel and thrusters are actuators that are utilized in spacecraft for attitude maneuvers.

Reaction wheel is the most commonly used actuator in spacecraft. It is a precise and reliable actuator. There are different approaches that are proposed in fault detection and isolation for reaction wheel actuators in single spacecraft but the development of an FDII system for detecting and isolating faults in reaction wheel of spacecraft especially in formation of flying spacecraft is still a challenging problem.

The desired FDII in formation flying spacecraft must have the capability of detecting the faults in formation and isolating the faulty satellite and also identifying the type of faults in the reaction wheels within a proper constraint.

1.2 Literature Review

Research into formation flying of satellites has gained in popularity during the 1990's and over the past decade and during these years numerous formation flying missions have been conceived. Two such missions are ESA's CLUSTER mission [97] and the ESA/NASA GRACE mission [98].

CLUSTER comprises of four identical spacecraft launched into large, highly elliptical polar orbits around the Earth. These satellites fly in pre-determined relative orbits designed so as to allow scientists to measure subtle changes in the interaction between the Earth and the Sun. The CLUSTER satellites were launched in August 2000 for nine years and its mission is extended until 31 December 2014 [97,95].

Another mission that implements a formation flying technology is the GRACE mission. The GRACE mission features two identical satellites in a leader-follower formation (GRACE A and GRACE B) orbiting the Earth on the same orbital plane. The purpose of this mission is to generate high-fidelity modeling of Earth's gravitational field. A secondary experiment that GRACE performs is examining how the atmosphere affects GPS signals. The initial altitude of GRACE A and GRACE B above the Earth was close to 500 km. Due to atmospheric drag, it will decrease to about 300 km towards the end of the mission. It is originally funded for a five-year period (2002 to 2007) however the mission was been further extended to 2009. As the orbit decay has been slower than initially thought and the satellite's current fuel supply is expected to last another few years at the very least, the mission is likely to continue until 2015 [98,95].

Another two ESA formation flying missions are PRISMA [99] and PROBA-3 [100]. PRISMA is a Swedish-led satellite project with the objective to develop and qualify new technology necessary for future formation flying science missions. PRISMA con-

sists of two spacecraft, with a total mass of about 200 kg. It contains several new technologies within autonomous formation flying and rendezvous, small rocket engines and Micro Electro Mechanical Systems (MEMS). The PRISMA satellites were launched from Dnepr-1, Russia, on 15 June 2010 [95]. PROBA-3 [100] is the ESA formation flying mission that is scheduled to be launched in 2017 for future formation flying missions. The PROBA-3 mission will demonstrate algorithms, sensors, propulsion systems and other technologies needed for formation flying.

An important joint NASA/ESA mission, implementing a number of critical formation flying technologies is the Laser Interferometer Space Antenna (LISA) [101]. LISA is designed to detect "ripples" in space-time, as predicted by Einstein's general theory of relativity. LISA's three spacecraft will form an equilateral triangle with an arm length of about 5 million km. Each spacecraft houses two free floating cubes made of a gold-platinum alloy inside the spacecraft, shielded from adverse effects of being in interplanetary space. The distance between the cubes in different spacecraft is monitored using highly accurate laser-based techniques [101,95].

NASA has proposed many formation flying missions. Some of these missions are currently under development, while others are in conceptual stages. One of NASA's main formation flying missions is the Magnetospheric Multiscale Mission (MMS) [102]. MMS includes four identical spacecraft in a variably spaced tetrahedron with a planned two-year mission lifetime. The system includes inter-spacecraft ranging, communication and instrumentation, designed to measure magnetic and electric fields using electron and ion plasma spectrometers, providing high temporal and spatial resolution. MMS is currently in the preliminary design stage and its launch is planned for 2014.

The NASA's future formation flying missions are the Stellar Imager (SI) [103] and Milli-Arc-Second Structure Imager (MASSIM) [104] that all planned for the third decade of the 21st century. The SI mission is a space-based ultraviolet (UV)/optical interferometer with over 200 times the resolution of the Hubble space telescope. The proposed MASSIM mission will image in X-rays the structure of astrophysical objects with an angular resolution three orders of magnitude better than the present state of

the art. An optics spacecraft carrying an array of diffractive/refractive lenses focuses X-rays onto detectors on a spacecraft 1000 km behind.

1.3 Objective of the Thesis

The main objective of this thesis is to propose a fault detection, isolation and identification (FDII) scheme for attitude control subsystem of formation flying of satellites. In this scheme, the reaction wheel is chosen as an actuator in order to verify the FDII scheme in formation flying missions. In order to fulfill this objective, the dynamics of actuator are presented and the formation flying control architectures are provided and described in detail. Different fault scenarios in the reaction wheel actuators are described and considered in this research. A hierarchical level FDII scheme based on discrete wavelet transform and neural networks are proposed in this thesis that consist of the spacecraft-level FDII scheme and the formation-level FDII scheme. These two approaches are developed, described and evaluated for formation flying satellites and extensive simulation results are also provided as well.

1.4 Contributions of the Thesis

The main contributions of this thesis are described as follows:

- A novel fault detection, isolation and identification scheme for a reaction wheel that is used as an actuator in the attitude control subsystem of satellite is proposed by employing wavelet entropy and neural networks. The proposed scheme is capable of successfully detecting, isolating and identifying three classes of commonly occurring faults in reaction wheel actuators.

- The results that are obtained through simulations indicate that formation flying fault analysis scheme can detect, isolate and identify both low severity and high severity faults in the reaction wheels however, single satellite fault diagnosis scheme can only detect and isolate high severity faults in the reaction wheels.

Hence, by employing formation-level fault diagnosis scheme, the accuracy and precision of the fault analysis in formation flying of satellites is shown to be improved.

- The results obtained through a large number of simulation scenarios demonstrate a high level of accuracy and precision and classification accuracy. The capability of the wavelet entropy and neural networks schemes in the fault diagnosis problem was successfully demonstrated.

There are several advantages to using spacecraft formation flying such as increased reliability, accuracy, robustness, flexibility, cost energy efficiency and probability of success. The proposed scheme for fault detection and isolation is capable of detecting and isolating the faults autonomously and reducing significant amount of hours that could have otherwise be spend by the ground station personal in order to analysis the faults. The reliability and performance of the formation flying mission can also be significantly improved.

1.5 Outline of the Thesis

The organization of this thesis is described as follows:

- In Chapter 2, the fault detection and isolation problems are presented and two main categories of fault analysis methods are discussed. Furthermore, different approaches in the literatures for FDII in satellites are presented.

- In Chapter 3, the concept of coordinate systems and different attitude representations are provided and, then the concept of spacecraft dynamics and formation flying of spacecraft control architectures are explained. Furthermore, in this chapter different types of sensors and actuators that are utilized in the spacecraft are described and the mathematical model of the reaction wheel actuator is explained and finally, the mathematical models for the attitude disturbances in the satellites are provided.

- In Chapter 4, the wavelet-entropy fault detection scheme for single spacecraft is proposed and developed. In this scheme the absolute attitude measurements in the satellite are considered for fault diagnosis and different fault scenarios in the reaction wheel actuators are explained and considered. The fault isolation scheme based on relative wavelet energy is proposed and the fault identification scheme based on discrete wavelet transform and neural networks for a single satellite are developed and the metrics of accuracy and precision (from the confusion matrix) are provided for the FDII scheme.

- In Chapter 5, the FDII scheme in the formation flying is proposed and developed. In this scheme the relative attitude measurements are considered for fault diagnosis purposes. In order to evaluate this scheme in the formation flying, the fault scenarios in the reaction wheels that are considered in Chapter 4 are simulated and the accuracy and the precision of the proposed fault detection scheme are evaluated and compared to the proposed FDII scheme in a single spacecraft that is explained in Chapter 4. Then, the fault isolation and identification schemes for the formation flying are developed and evaluated.

- In Chapter 6, conclusions and the main contributions of this research are described and possible future work based on these contributions are provided.

Chapter 2

Fault Detection and Isolation Problem

There is an increasing demand for modern control systems such as autonomous spacecraft to operate autonomously in the presence of faults and failures in sensors, actuators, and components. This requires a fault diagnosis system that is capable of detecting plant, actuator and sensor faults when they occur and isolating the faulty component. The main tasks of fault diagnosis are to detect and isolate occurring faults in order to avoid overall failure of the monitored system. Fault diagnosis is an essential component of an autonomous system. Hence, a high demand exists for the development of intelligent systems that are able to autonomously detect the presence and isolate the location of faults occurring in different components of complex dynamical systems. Especially faults in a control loop are of particular importance as they may instantly result in instability of the controlled system. Thus, it is crucial that faults are efficiently and timely detected and isolated while the system is in operation.

2.1 Classification of Fault Diagnosis Systems

The fault diagnosis (that is fault detection, isolation and identification) techniques in the literature can be divided into model-based and history-based categories [59]. The model-based can be broadly classified as qualitative or quantitative. The model is

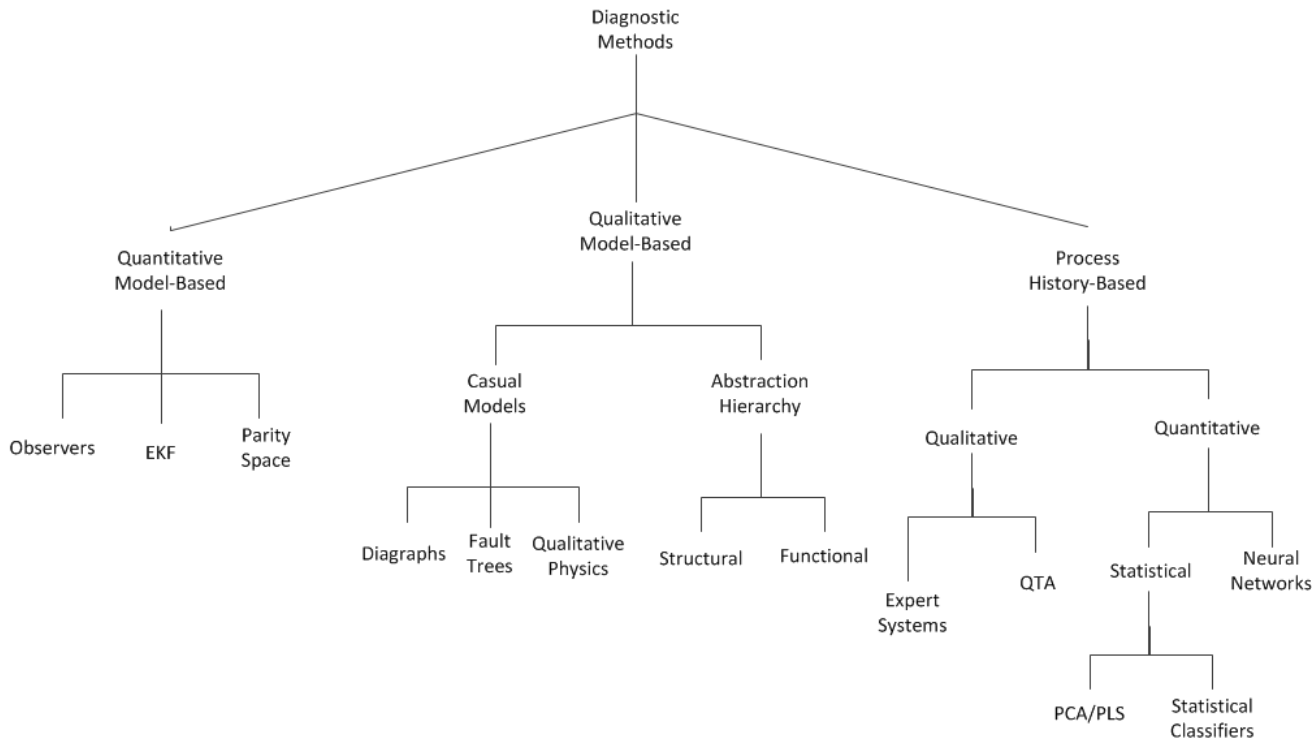

Figure 2.1: Classification of fault diagnosis systems [59].

usually developed based on some fundamental understanding of the physics of the process. In quantitative models this understanding is expressed in terms of mathematical functional relationships between the inputs and outputs of the system. However, in qualitative model these relationships are expressed in terms of qualitative functions centered on different units in a process. In process history based methods only the availability of large amount of historical process data is assumed. There are different ways to transform and present these to a diagnostic system. This is known as the feature extraction process from the process history data, and is done to facilitate subsequent diagnosis. This extraction process can mainly proceed as either quantitative or qualitative feature extractions. In quantitative feature extraction one can perform either a statistical or a non-statistical feature extraction. The classification of diagnostic systems is shown in Figure 2.1.

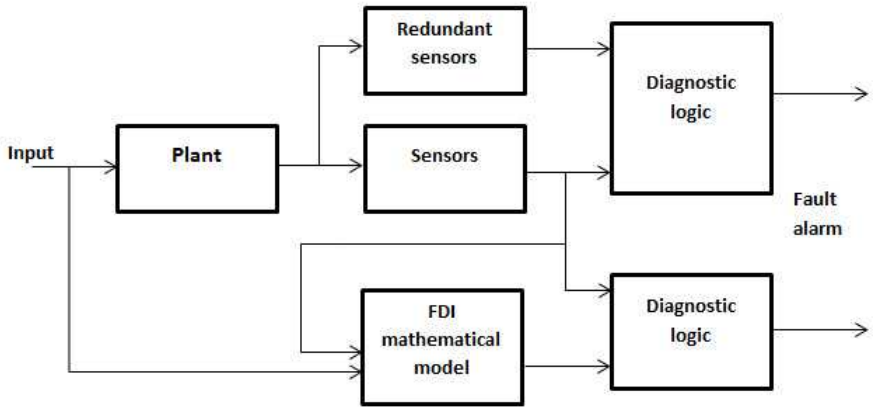

Figure 2.2: Hardware and analytical redundancy schemes [117].

2.1.1 Model-Based Fault Diagnosis

A traditional approach to fault diagnosis is based on the hardware redundancy method which uses multiple sensors, actuators, computers and software to measure or control a particular system [33]. The major problems encountered with hardware redundancy are the extra equipment, maintenance cost and the additional space required to accommodate the redundant components. An alternative approach for fault diagnosis is based on analytical redundancy which uses the redundant analytical relationships among system inputs and measured system outputs to generate residual signals where no extra hardware is required in this approach. In analytical redundancy schemes, the resulting difference that is generated from consistency checks of different variables is called a residual signal. Analytical redundancy schemes make use of a mathematical model of the monitored system and is often referred to as the model-based approach to fault diagnosis. Figure 2.2 illustrates the concepts of hardware and analytical redundancy [33]. The principle of model based fault detection and isolation is depicted in Figure 2.3. As mentioned before, model based fault diagnosis is divided into two categories, quantitative approaches and qualitative approaches. The quantitative model-based method utilizes a mathematical model. The techniques commonly used are based on observer approach, parameter estimation, parity space, and combination of the first three [49,50,51].

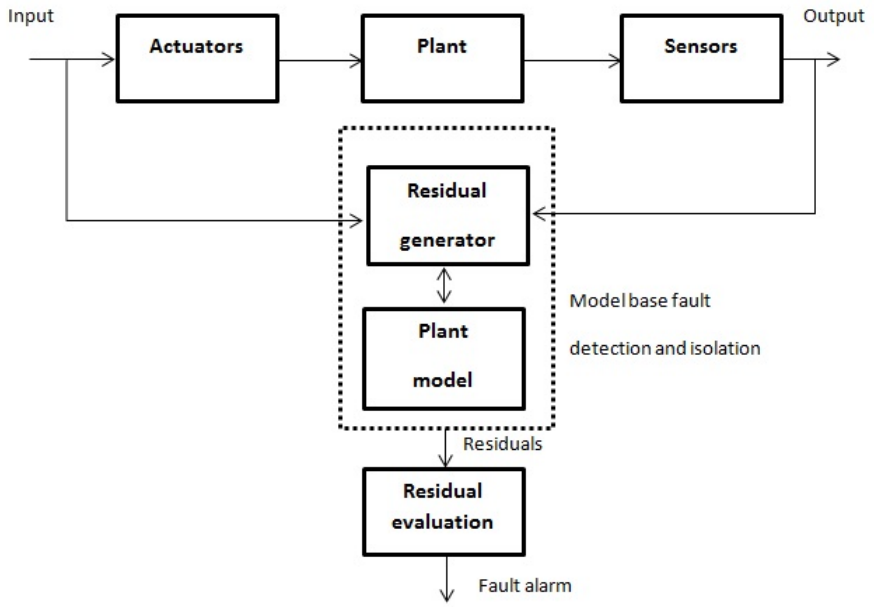

Figure 2.3: Model based fault detection and isolation approach [117].

In observer or state estimation approaches, two observer methods are used to estimate the outputs of the system Luenberger observers in the deterministic setting [34,35,36,37,38,39,40,41] or Kalman filters in a stochastic setting [42,43,44]. The popularity of state-space models as well as the wide usage of observers in modern control theory and applications has made the observer based fault diagnosis approach as one of the most common approaches in this domain. In parity space approach, the system input and output data checks over a given time window and the residual signals (or parity vectors) are generated [45,46,47,48]. The Parameter estimation method [52,53] is based on system identification techniques. This method is based on the concept that faults typically affect the physical coefficients of the process such as friction, mass, viscosity, resistance, etc. In this approach the parameters of the actual process are estimated on-line and the results are compared with the parameters of the reference model that is obtained under the healthy condition.

In recent years, fault diagnosis schemes for nonlinear systems have been widely investigated. Most techniques in the literature utilize the extension of the methods that are described above for linear systems. Many nonlinear observer schemes

were proposed and developed in the literature for solving the nonlinear system fault diagnosis problem [54,55,56,57,58].

As mentioned before, in quantitative model-based methods, the understanding of model is expressed in terms of mathematical functional relationships between the inputs and outputs of the system. In contrast, in qualitative models the relationships among system variables and parameters are used to describe the system behavior in qualitative terms such as causalities and IF-THEN rules. The qualitative model can be developed either as qualitative casual models or abstraction hierarchies. The knowledge in the casual models can be represented qualitatively in various forms, such as digraphs, fault trees or qualitative physics [60].

2.1.2 History-Based Fault Diagnosis

Model-based fault diagnosis approaches rely on the key assumption that a perfectly accurate and complete mathematical model of the system under supervision is available. However, such an assumption may not always be valid in practice. This problem has contributed to the development of history-based FDII methods. Fuzzy logic, neural networks and wavelet transform are three history-based approaches that have been utilized in literature for fault diagnosis schemes.

These approaches become increasingly more appealing for situations where high-fidelity mathematical model of the monitored system does not exist or is extremely difficult to obtain. The main challenge though is to ensure that sufficient amount of data from the healthy operational mode of the system is available. Fuzzy logic is now being investigated as powerful modeling and decision making tool for nonlinear fault diagnosis systems [61]. Fuzzy logic method for fault diagnosis problem belongs to the sub-class of rule-based expert systems and it can express expert knowledge in terms of natural language statements. It has the potential to formulate the qualitative relationships among the model variables of the process being monitored using IF-THEN rules.

Fuzzy sets perform a smooth interface between the qualitative variables involved in the rules and the numerical data at the inputs and outputs of the model. The

appealing feature of fuzzy logic is that its ability to deal with imprecise facts or noisy data, and is therefore suited for application where complete information about fault and system is not available to the fault diagnosis designer [62,63]. Whenever expert knowledge is not available and the fuzzy rules are obtained using qualitative physics, neural networks are profoundly used for learning (or determining) the parameters of those rules from historical input−output data of the system, hence the name neuro-fuzzy systems [63,64].

As mentioned above, neural networks are among the most widely used intelligent techniques for fault diagnosis. This is mainly due to their distinguished ability to approximate, to an arbitrary level of accuracy, any continuous nonlinear function, given suitable network parameters (or weights), architecture, and learning algorithm [65,66]. Indeed, neural networks are able to learn nonlinear functions from examples. They have the ability to make intelligent decisions even in cases where system data are corrupted with noise. They also have a highly parallel structure, which is expected to achieve a higher degree of fault-tolerance than conventional function approximation schemes and, last but not the least, they are readily applicable to multi-variable systems. Neural networks can also be applied to process health monitoring, where the focus is on identification of small irreversible changes in the process that may develop into bigger faults [67,68,69,70,71].

The capability of wavelet in feature extraction of diagnosis signals in time and frequency domain, leads to utilize this method in fault diagnosis schemes. Wavelet decomposition has the property of well-localized in time and frequency domain and time-frequency window can be adjusted with the practical signals. Furthermore, wavelet-entropy represents the degree of chaos of the measured signal which can provide useful information about the faults in the system. Many approaches have been developed in the literature based on wavelet decomposition for fault diagnosis of nonlinear systems [72,73,74,75,76,77,78].

2.1.3 Hybrid Methods

One of the important points in fault diagnosis schemes is that no single method is adequate to handle all the requirements for a diagnostic system. Though all the methods are restricted, in the sense that they are only as good as the quality of information provided, it was shown that some methods might better suit the knowledge available than others. Some of these methods can complement one another resulting in better diagnostic systems. Integrating these complementary features is one way to develop hybrid methods that could overcome the limitations of individual solution strategies. Hence, hybrid approaches where different methods work in conjunction with one other to solve parts of the problem are attractive.

Wavelet decomposition has strong capability in dealing with signals in time and frequency domains and can detect anomalies in signals and neural networks is a strong nonlinear classifier and it has a strong capability in pattern recognition and pattern classification. Hence, combining these two methods gives us a strong fault detection and isolation scheme for nonlinear systems [72,73,74,76].

2.2 Desired Characteristics of Fault Diagnosis Systems

In order to compare various diagnostic approaches, it is useful to identify a set of desirable characteristics that a diagnostic system should possess. According to [59] the ideal fault detection and isolation (FDI) system must have the following characteristics:

- Quick detection, isolation and identification

  Quickness is a critical factor for fault diagnosis systems. The diagnosis system must respond quickly in detection, isolating and identification malfunctions in monitored system.

- Isolability

Isolability is the ability of the diagnostic system in classification of different faults in system. This ability depends to a great extend on the monitored system characteristics.

- Robustness

  Robustness with respect to noise, disturbances, uncertainties and unmodeled dynamics is a desirable feature in fault diagnosis systems.

- Novelty identifiability

  The FDI system must be able to decide if the monitored system works in normal or abnormal condition and if abnormal, whether the cause is a known fault or unknown fault.

- Classification error estimate

  The FDI system must provide the classification error in monitored system. Such error is useful to give the level of reliability of the FDI system.

- Adaptability

  The monitored system may change due to structural changes or disturbances and also changing in environmental condition. Thus the diagnostic system must be adaptable to these changes.

- Explanation facility

  The diagnostic system must also provide the explanation on the origination of the faults in monitored system. This requires the reasoning ability on causes and effects relationships in a system.

- Modeling requirements

  For development of diagnosis classifier to perform in real-time the modeling effort must be as minimal as possible.

- Storage and computational requirements

The fault diagnosis system must implement algorithms that are computationally not too complex and have high capability of storing relevant information.

- Multiple fault identifiability

  The ability of detecting and isolating multiple faults is an important and also difficult task in diagnostic systems.

2.3 Previous Work on Fault Diagnosis of Attitude Control Subsystem (ACS) of Spacecraft

In recent years, there has been a special interest in developing autonomous fault diagnostic approaches for actuators of the attitude control subsystem (ACS) of spacecraft. As mentioned previously, the research is focused on two major approaches, model based and history based methods.

Reference [31] proposed a reliable failure classification system based on the fault-tree method. This methods was tested with data extracted from a reaction wheel actuator of a simulated attitude control subsystem of a satellite.

In [85], a neural network observer-based scheme for the actuator fault detection and isolation in the spacecraft attitude control subsystem is presented. This FDI system consists of three Elman recurrent neural networks and each of them is specific for modeling the dynamics of the wheel on each axis separately and independently.

In [86], an actuator fault detection and isolation system for the ACS of a satellite is proposed. This FDI system uses a recurrent adaptive time delay neural network and has robustness and insensitivity characteristics due to the external disturbances and noise.

In [26], a dynamic neural network residual generator based on the dynamic multilayer perceptron network (DMLP) is proposed. The developed neural observer is applied to the reaction wheel model and the results are compared to the linear model-based observer acting as a residual generator. Also, adaptive neural network classifier based on learning vector quantization (LVQ) network is proposed in order to isolate

the faults.

In [32], fault detection and isolation systems based on dynamic neural networks for the pulsed plasma thrusters (PPTs) that are used in the ACS of a satellite in a formation flying are proposed. In this work, three FDI schemes are developed: "low-level" FDI, "high-level" FDI and "integrated" FDI. The low-level scheme utilizes the absolute measurements from the actuator and the high-level used relative attitude measurements in a satellite and the integrated scheme utilizes both previous schemes in order to improve the results.

Reference [84] deals with the real-time fault diagnosis in the ACS of a satellite based on sliding-window wavelet and dynamic recurrent neural networks. In this work, the sliding-window technique is utilized in order to detect anomalies in reaction wheel actuator and the dynamic recurrent neural network is used to isolate the faults in a reaction wheel.

In [108] a hierarchical fault detection, isolation and recovery approach is developed for avionics and spacecraft applications. Fault-three synthesis and neural networks are utilized in [109] to develop a fault diagnosis approach for the RADARSAT-1 ACS. Reference [110] provides a fault detection, isolation and recovery approach for the ACS of the ESA GOCE satellite and references [111,112,113,114,115] deal with the integration, reutilization, and standardization of FDI systems used in previous missions planned by the Jet Propulsion Laboratory (JPL) and European Space Agency (ESA).

2.4 Conclusions

In this chapter the concepts of fault detection, isolation and identification (FDII) have been provided and the characteristics of the desired FDII system are provided. The FDII approaches are divided into two main categories; model based methods and history based methods. The advantages and disadvantages for each group have been discussed and compared. The previous works for FDII in spacecraft have been provided and motivations for FDII in formation flying spacecraft have also been ex-

plained.

Chapter 3

Formation Flying of Satellites

The NASA's Goddard Space Flight Center (GSFC) proposed the definition of spacecraft formation flying as follows [95]:

"The tracking or maintenance of a desired relative separation, orientation or position between or among spacecraft."

Hence, formation flying spacecraft is a particular case of a more general category. There are several advantages to utilize formation of multiple spacecraft. These includes robustness, accuracy, feasibility cost and energy efficiency. This chapter provides an overview on the fundamentals of formation flying control architectures and defines the formation flying attitude control subsystem that is used to evaluate fault diagnosis systems and also different sensors and actuators that are used in spacecraft. Section 3.1 introduces the concept of coordinate reference frames, Section 3.2 describes rotational matrix for coordinate frames transformation, in Section 3.3 different attitude presentations are described and in Section 3.4 the formation flying of multiple spacecraft is discussed. In Section 3.5 the spacecraft sensors and actuators are presented, while Section 3.6 discusses mathematical modeling of reaction wheel actuators in spacecraft and finally, the mathematical modeling of the external attitude disturbances are described in Section 3.7.

3.1 Coordinate Reference Frame

In spaceflight analysis in order to know the position and motion of a satellite, one must first select the correct coordinate system for the problem. A description of the three main coordinate systems used in formation flying calculations is presented below [88]. The representation of the satellite's position and attitude is dependent on these reference frames. Hence, the definitions of these reference frames, and how to rotate vectors between them, are crucial for satellite formation flying studies.

3.1.1 Earth Centered Inertial (ECI) Frame

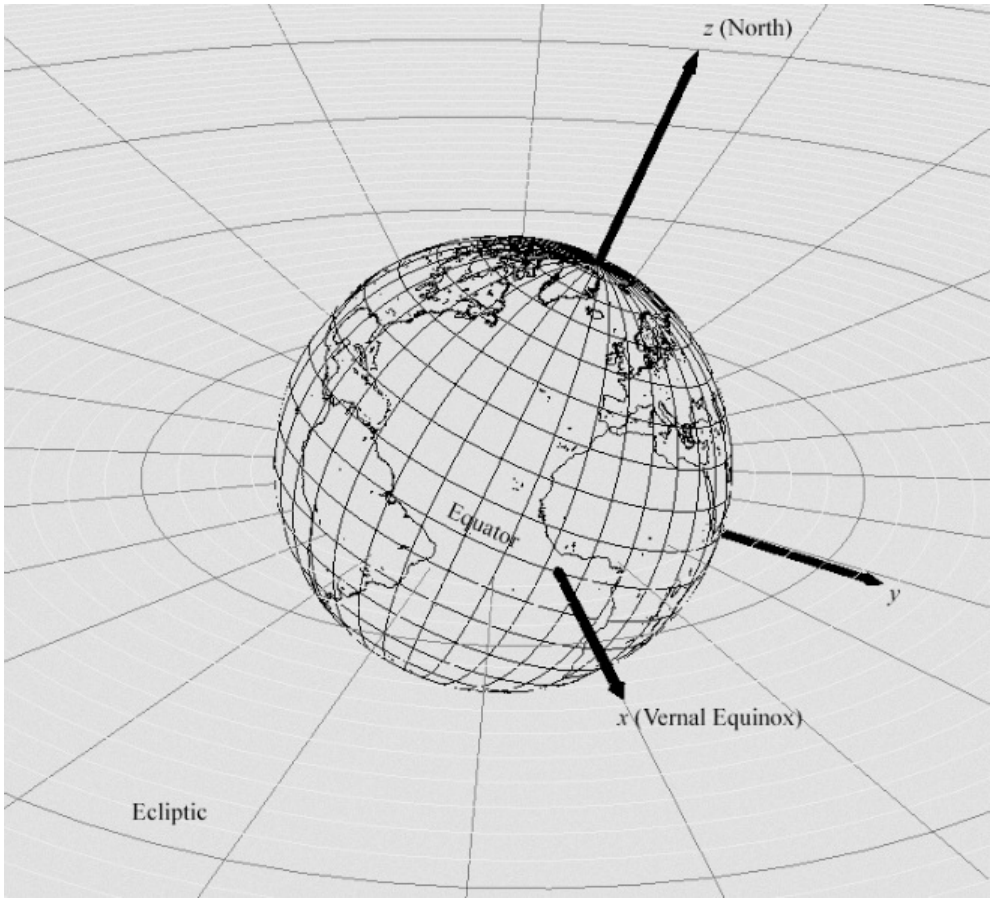

Figure 3.1: Earth-Center inertial frame, F_i [118].

This frame is fixed in space, which means that it is a non-accelerated reference frame in which Newton's Laws are valid. The origin of the frame is oriented at the

center of Earth. The x axis points in the direction of the vernal equinox, z-axis points toward the North Pole and y-axis completes the right hand Cartesian coordinate system. This frame is denoted by F_i. Figure 3.1 illustrates the axes of the ECI frame in space.

3.1.2 Body Frame

This frame is a moving reference frame which is fixed on the satellite. The orientation of the satellite is determined relative to the Orbit frame, while angular velocities are expressed in the Body frame. The origin of this frame is the center of mass of the satellite body, the x-axis forward and z-axis is downward, y-axis completes the right hand orthogonal system. The origin is at the center of the mass of the satellite. This frame is denoted by F_b.

3.1.3 Orbital Frame

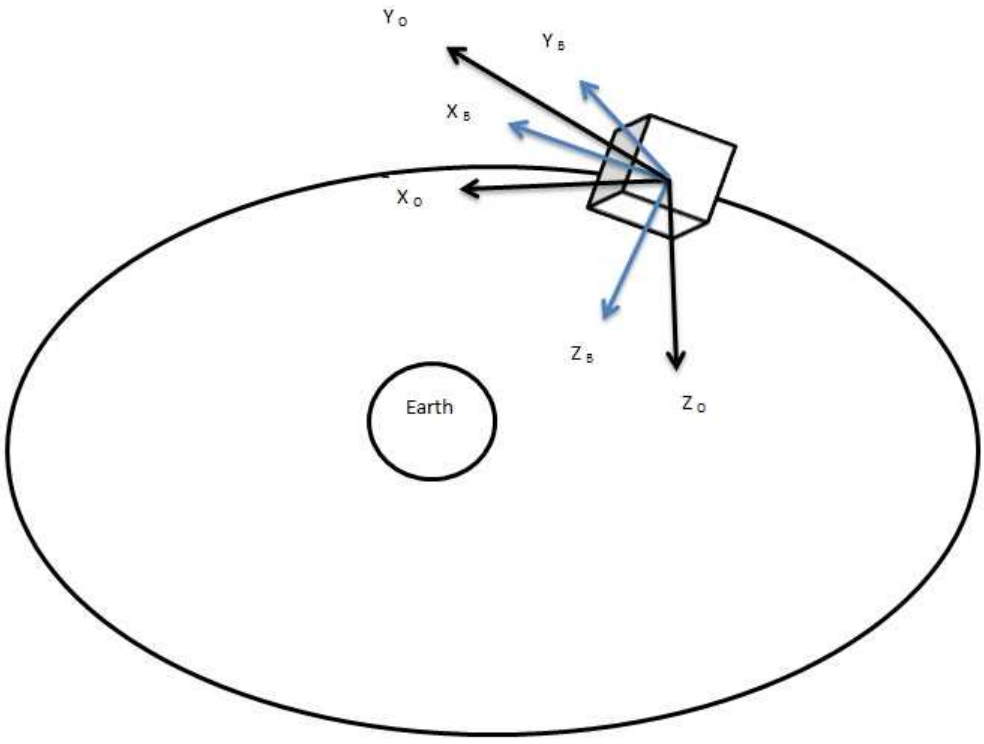

Figure 3.2: Satellite orbital and body frame.

Orbit frame rotates relative to the inertial frame, with a rate of depending on the altitude of the satellite. The origin is at the center of mass of the satellite. The y-axis is in the orbit anti-normal direction. The z-axis points toward the center of Earth, and the x-axis completes the right hand system. Figure 3.2 illustrates the orbital frame and body frame of a satellite. This frame is denoted by F_O.

3.2 Rotational Matrix

Rotation matrix is a description of the rotational relationship between two reference frames. The rotation matrix C from frame m to n is denoted ba C_m^n. Rotation of a vector from frame m to frame n, can be given as

$$v^m = C_m^n v^n \tag{3.1}$$

The orientation of the satellite is described using a rotation matrix (direction cosine matrix) C_O^B , which is denoted as

$$C_O^B = \begin{pmatrix} m_{11} & m_{12} & m_{13} \\ m_{21} & m_{22} & m_{23} \\ m_{31} & m_{32} & m_{33} \end{pmatrix} \tag{3.2}$$

In this matrix each of the elements m_{ij} is named directional cosines and column vectors can be arranged as:

$$m_1 = \begin{pmatrix} m_{11} \\ m_{21} \\ m_{31} \end{pmatrix} \quad m_2 = \begin{pmatrix} m_{12} \\ m_{22} \\ m_{32} \end{pmatrix} \quad m_3 = \begin{pmatrix} m_{13} \\ m_{23} \\ m_{33} \end{pmatrix}$$

Rotation matrix is an orthogonal matrix, thus m_1, m_2 and m_3 are orthogonal. The rotation matrix satisfies the following properties:

$$C_B^A = (C_A^B)^{-1} = (C_A^B)^T \tag{3.3}$$

$$C_B^A C_A^B = I_{3\times 3} \tag{3.4}$$

3.3 Attitude Representation

There are many ways to represent the attitude of a satellite in a reference frame. But frequently Euler angles and Unit Quaternions are the two mostly used for presenting a satellite orientation. Euler angles are reliable, simple and accurate enough for applications, however sometimes singularities occur in coordinate transformations. In order to avoid singularities, Quaternion representation can be used as representation method as described below. In our simulation we have used unit quaternions representation.

3.3.1 Euler Angles Representation

The Euler angles representation is often used in a user's interface during attitude computation because of its clear physical interpretation. Its parameters consist of three rotation angles known as the roll angle ϕ, pitch angle θ and yaw angle ψ. The angles roll, pitch and yaw represent the rotations about the x, y and z axis, respectively in a rotation from one frame to another. These angles are illustrated in Figure 3.3. The tranformation of a vector in an initial reference frame (x_i, y_i, z_i) to a new vector in the satellite body frame (x_b, y_{b,z_b}) is given as follows

$$\begin{pmatrix} x_b \\ y_b \\ z_b \end{pmatrix} = \begin{pmatrix} 1 & 0 & 0 \\ 0 & cos(\phi) & sin(\phi) \\ 0 & -sin(\phi) & cos(\phi) \end{pmatrix} \begin{pmatrix} cos(\theta) & 0 & -sin(\theta) \\ 0 & 1 & 0 \\ sin(\theta) & 0 & cos(\theta) \end{pmatrix} \begin{pmatrix} cos(\psi) & sin(\psi) & 0 \\ -sin(\psi) & cos(\psi) & 0 \\ 0 & 0 & 1 \end{pmatrix} \begin{pmatrix} x_i \\ y_i \\ z_i \end{pmatrix} \tag{3.5}$$

3.3.2 Unit Quaternions

Unit quaternions are the other way for the attitude representation. They were first described by the Irish mathematician Sir William Rowan Hamilton in 1843 and applied to mechanics in three-dimensional space. Unit quaternions has several advantages

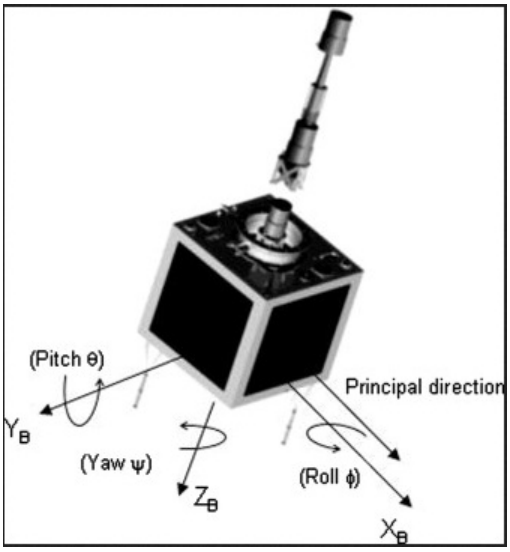

Figure 3.3: Euler angles in satellite [119].

over the Euler angles. Quaternions involve the use of algebraic relations to determine the elements of the rotation matrix. The computations are faster and there are no singularities as may occur on the Euler angle formulation. The disadvantage is that there is no obvious physical interpretation of the rotation geometry.

Quaternion has 4 elements. Three of the elements are vectors which define an axis of rotation and the fourth element is a scaler that defines the magnitude of a rotation angle about the axis of rotation. A quaternion can be represented as:

$$Q = \vec{i}q_1 + \vec{j}q_2 + \vec{k}q_3 + q_4 \tag{3.6}$$

The q_i $(i = 1 - 4)$ can be defined as:

$$q_1 = m_1 sin\frac{\mu}{2} \quad q_2 = m_2 sin\frac{\mu}{2} \quad q_3 = m_3 sin\frac{\mu}{2} \quad q_4 = cos\frac{\mu}{2} \tag{3.7}$$

where m_1, m_2, m_3 are the rotation axis and μ is the rotation angle. The unit quaternion satisfy $q^T q = 1$ which also means that $q_1^2 + q_2^2 + q_3^2 + q_4^2 = 1$. The rotation matrix

from Body frame to the orbital frame can be expressed in quaternions as:

$$C_B^O = \begin{pmatrix} 1-2(q_3^2+q_4^2) & 2(q_2q_3-q_4q_1) & 2(q_2q_4+q_3q_1) \\ 2(q_2q_3+q_4q_1) & 1-2(q_2^2+q_4^2) & 2(q_3q_4-q_2q_1) \\ 2(q_2q_4-q_3q_1) & 2(q_3q_4+q_2q_1) & 1-2(q_2^2+q_3^2) \end{pmatrix} \tag{3.8}$$

3.3.3 Satellite Attitude Dynamics

The satellite is modeled as a rigid body and its dynamic model is derived using the Euler's dynamical equation [89,90]. Euler's dynamical equation is the equivalent of Newton's second law of motion for rotation about the center of mass. It is defined as

$$\frac{d\vec{h}}{dt} = \vec{\tau} \tag{3.9}$$

where $\vec{h} = I.\vec{\omega}$ is the angular momentum, and τ is the sum of all external torques acting on the body.

Equation (3.9) is expressed with respect to the inertial reference frame. With respect to the body reference frame with an angular velocity $\vec{\omega}$, Euler's equation becomes

$$\dot{\vec{h}} + \vec{\omega} \times \vec{h} = \vec{\tau} \tag{3.10}$$

The scaler form of this equation becomes

$$\begin{aligned} \dot{h_x} + \omega_y h_z - \omega_z h_y &= \tau_x \\ \dot{h_y} + \omega_z h_x - \omega_x h_z &= \tau_y \\ \dot{h_z} + \omega_x h_y - \omega_y h_x &= \tau_z \end{aligned} \tag{3.11}$$

where h_x, h_y, h_z are the angular momentum components along the body coordinates and $\omega_x, \omega_y, \omega_z$ are the angular velocity components about the body axes and τ_x, τ_y, τ_z are the body referenced external torques.

If we assume that the spacecraft body frame is aligned with the principal axes,

then we can have

$$h_x = I_x \omega_x$$

$$h_y = I_y \omega_y$$

$$h_z = I_z \omega_z \tag{3.12}$$

so that equation (3.11) becomes

$$I_x \dot{\omega_x} - \omega_y \omega_z (I_y - I_z) = \tau_x$$

$$I_y \dot{\omega_y} - \omega_x \omega_z (I_z - I_x) = \tau_y$$

$$I_z \dot{\omega_z} - \omega_y \omega_z (I_x - I_y) = \tau_z \tag{3.13}$$

where I_x, I_y, I_z are the principal moments of inertia of the body. Equation (3.13) describes the attitude dynamics of a rigid body satellite.

3.4 Formation Flying of Multiple Spacecraft

A spacecraft formation consists of two or more spacecraft in specific relative positions and orientations. Dispersing the functions of a single spacecraft over a formation of smaller spacecraft produces robust and fault-tolerant system architecture and reduces the costs of the mission. A formation of small satellites would be cheaper to develop and launch, but could still perform the tasks of a large, single satellite mission through proper task distribution. The failure of a single spacecraft in a formation does not necessarily lead to system failure as it would in a single, larger spacecraft. Upgrades or repairs could be performed by simply replacing any obsolete or disabled spacecraft. Finally, the capability of obtaining multiple simultaneous measurements along a large baseline would enable satellite formations to accomplish goals that are difficult or impossible to achieve with a single satellite. Three main architectures for formation flying control are proposed in literature which can be defined as follows [95,96]:

- Leader-follower structure

In the leader-follower strategy, one typically divides the spacecraft into subgroups. Within each subgroup one spacecraft is defined as the leader and the rest are defined as followers. Leader spacecraft is controlled to a reference orbit and the other follower spacecraft in the formation control their relative states to that leader. This approach has the advantage that it allows most satellites in the formation to follow the natural dynamics of the absolute orbit of the leader, while only performing regular automatic control on the relative states of the formation. The principal disadvantage of leader-follower is that the leader spacecraft is by definition at its correct state and will not require as much fuel use as the followers. Fuel use can be balanced among the satellites by periodically interchanging the designations of the leader and followers.

- Behavioral structure

  In the behavioral strategy, the control action for each spacecraft is defined by a weighted average of the controls corresponding to each desired behavior for the spacecraft. This approach eases the implementation of conflicting or competing control objectives, such as tracking versus avoidance. It is however difficult to enforce group behavior, and to mathematically guarantee stability and formation convergence.

- Virtual structure

  In the third approach, virtual structure, the spacecraft formation is viewed as a virtual rigid body. The desired states of a single spacecraft, may be specified such that the formation moves as a single structure. In this scheme it is easy to prescribe a coordinated group behavior and the formation may be maintained well during maneuvers, given that the single spacecraft is able to follow its trajectory and the chief advantage of this approach over the leader/follower method is that state error will pertain to all the spacecraft in the formation.

3.5 Formation Flying Missions

3.5.1 Formation Flying Architecture Control Design

In our simulations, in order to simulate the flying of formation spacecraft, a decentralized architecture is developed to control the formation spacecraft via virtual structure [91]. In this thesis, four coordinate reference frames are used for formation flying of spacecraft. The inertial frame F_i, the formation frame F_F which is fixed at the virtual center of the formation, body frame F_b and reference frame F_b^d which denotes the desired configuration for each spacecraft. As described previously, in the virtual structure approach, the entire desired formation is treated as a single structure with a formation frame located at its virtual center of mass to represent its configuration.

The virtual structure has attitude q_F and angular velocity ω_F relative to inertial frame. Let q_i and ω_i represent the attitude and angular velocity of the i-th spacecraft relative to the inertial frame. Similarly, let q_{iF} and ω_{iF} represent attitude and angular velocity of the i-th spacecraft relative to formation frame. The actual states of the ith place holder represent the desired states of the ith spacecraft, hence these states are denoted by q_{iF}^d and ω_{iF}^d. Generally q_{iF}^d and ω_{iF}^d can vary with time, that means the formation shape is time-varying, however, in our simulations, we are concerned that formation maneuvers must preserve the overall formation shape, i.e, each spacecraft needs to preserve a fixed relative position and orientation in the virtual structure, hence, q_{iF}^d should be constant, and ω_{iF}^d should be zero. The state of the virtual structure is defined as

$$\xi = [q_F^T, \omega_F^T]^T \tag{3.14}$$

If each spacecraft has knowledge of ξ and of its own desired position and orientation with respect to the virtual structure, then formation keeping is transformed into an individual tracking problem. Therefore, the vector ξ represents the minimum amount of information needed by each spacecraft to coordinate its motion with the group.

Given q_F and ω_F, the desired states for the i-th spacecraft are given by:

$$[q_i^d]_o = [q_F]_o [q_{iF}^d]_F \tag{3.15}$$

$$[\omega_i^d]_o = [\omega_F]_o \tag{3.16}$$

3.5.2 Decentralized Architecture

In the decentralized architecture, each spacecraft in the formation instantiates a local copy of the coordination variable $\xi_i = [q_{Fi}^T, \omega_{Fi}^T]$. The ξ_i represents the coordination variable instantiated in the ith spacecraft corresponding to the coordination variable ξ defined in equation (3.14).

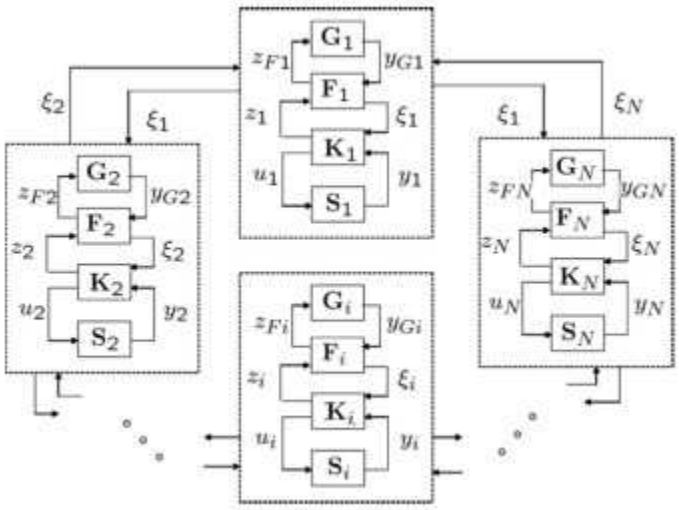

Figure 3.4: Decentralized architecture via the virtual structure approach [91].

A bidirectional ring topology is used to communicate the coordination variable instantiations, to bring each local instantiation into consensus. The decentralized architecture via virtual structure approach is illustrated in Fig 3.4. In this figure, block G_i is a discrete event supervisor for the i-th spacecraft, block F_i is the formation control module, which produces and broadcasts coordination variable, System K_i is the local spacecraft controller for the i-th spacecraft, and S_i represents the i-th spacecraft. When the formation maneuver starts, each discrete event supervisor G_i outputs the

current formation pattern to the formation control module F_i. Each formation control module implements a coordination variable instantiation ξ_i. Formation control module F_i then sends its coordination variable instantiation ξ_i to the local spacecraft controller K_i. Based on ξ_i the local controller K_i derives the desired states for the i-th spacecraft.

3.5.3 Formation Control Strategy

Two major tasks need to be carried out in the decentralized formation control via the virtual structure approach [95]:

- Propose suitable control law for each spacecraft
- Control each virtual structure instantiation into consensus.

Formation Control Strategy for Each Spacecraft

The control torque for the i-th spacecraft is given by [95]:

$$\tau_i = J_i\dot{\omega}_i^d + \frac{1}{2}\omega_i \times J_i(\omega_i + \omega_i^d) - k_{qi}\widehat{q_i^d q_i} - K_{\omega i}(\omega_i - \omega_i^d) \tag{3.17}$$

where k_{qi} is a positive scalar, K_{wi} is a symmetrical positive-definite matrix, and $\widehat{q_i^d q_i}$ is the vector part of the unit quaternion $q_i^{d*}q_i$ and q^* is the conjugate of a quaternion q.

Formation Control Strategy for Each Virtual Structure

The error state for the ith coordination variable instantiation is defined as

$$\widetilde{\xi}_i = \xi_i - \xi^d = [\widetilde{q}_{Fi}^T, \widetilde{\omega}_{Fi}^T]^T \tag{3.18}$$

where ξ^d represents a desired formation pattern to be achieved. There are two objectives for the coordination variable implemented in each spacecraft.

The first objective is to reach its desired constant goal σ^d defined by the formation pattern set and the second objective is to drive each instantiation to consensus, meaning that $\xi_1 = \xi_2 = ... = \xi_n$. The goal seeking error between ξ_i and ξ^d is defined as

$$E_G(t) = \sum_{i=1}^{n} \left\| \xi_i - \xi^d \right\|^2 \tag{3.19}$$

Also total consensus error between neighboring coordination variable instantiation is defined as

$$E_S(t) = \sum_{i=1}^{n} \left\| \xi_i - \xi_{i+1} \right\|^2 \tag{3.20}$$

where $\xi_{n+1} = \xi_1$ and $\xi_0 = \xi_n$. Defining $E(t) = E_G(t) + E_S(t)$, then the control objective is to drive $E(t)$ to zero asymptotically.

The proposed control torque τ_{Fi} is given as [95]:

$$\tau_{Fi} = k_G \widehat{q_F^{d*} q_{Fi}} - k_S \widehat{q_{F(i+1)}^{d*}} q_{Fi} - D_S(\omega_{Fi} - \omega_{F(i+1)}) - k_S \widehat{q_{F(i-1)}^{d*}} q_{Fi} - D_S(\omega_{Fi} - \omega_{F(i-1)}) \tag{3.21}$$

where $K_G > 0$ and $K_S \geq 0$ are scalars, D_S is symmetrical positive-semidefinite matrix and $\widehat{q}$ represents the vector part of the unit quaternion.

3.6 Attitude Sensors and Actuators

Attitude determination is the process of determining the orientation and location of the spacecraft relative to some reference frame. The most commonly used reference vectors are the unit vectors directed toward the Sun, the center of the Earth, a known star, or the magnetic field of the Earth. An attitude sensor measures the orientation of a given reference vector relative to the spacecraft reference frame [90]. Sun sensors, rate sensors, magnetometers and star cameras are among the various sensors that are used in a satellite.

Star sensors are different types of sensors which can be used for the attitude determination. The orientations of the spacecraft relative to the reference vectors can be computed after the orientation of these vectors are determined relative to the

spacecraft frame. The process of achieving and maintaining an orientation in space is called attitude control. Spacecraft is reoriented from one attitude to another with attitude maneuvering process.

After reorientation or an action that causes a change in attitude, the existing attitude shall be maintained relative to some defined reference frame. This is defined as attitude stabilization. Actuators are used for attitude control, stabilization or maneuvering actions. They supply the desired control torques needed to perform actions defined above. Different types of sensors and actuators are explained in the sections given below [88,90].

3.6.1 Attitude Sensors

In this section, different types of sensors that are used in attitude determination are explained [88,90].

Sun Sensors

Sun sensors are visible-light detectors which measure one or two angles between their mounting base and incident sunlight. They are popular, simple, inexpensive, reliable equipment with minimal power requirements but they require clear fields of view.

Star Sensors

Star sensors represent the most common sensors for high-accuracy missions. Star sensors measure the star coordinates in the spacecraft frame and provide attitude information when these observed coordinates are compared with known star directions obtained from a star catalog. Star sensors are heavy, expensive, require more power, and subject to interference from Sun, Earth, and other bright light sources. In spite of these disadvantages, they are the most accurate means of attitude determination with accuracies down to arc seconds.

Horizon Sensors

The essential way for directly determining the relative attitude of a spacecraft with respect to the Earth is to use horizon sensors. Horizon sensors are infrared devices that detect the contrast between the cold of deep space and the heat of earth atmosphere.

Magnetometers

Magnetometers are sensors which measure the size and direction of the Earth's magnetic field to determine the orientation of a spacecraft with respect to the local magnetic field. Magnetometers are widely used as attitude sensors since they are simple, reliable, and lightweight and have low power requirements. But magnetometers are not as accurate as star or horizon sensors. Due to a lack of complete knowledge of the magnetic field model, the predicted direction and magnitude of the field at the spacecraft's position are subject to errors. To improve the accuracy, their data usually are combined with data from sun or horizon sensors.

GPS Receivers

GPS receivers are known as high-accuracy navigation devices and have been used for attitude determination by employing the differential signals from separate antennas on a spacecraft. These sensors are low cost and low weight and are being used in low accuracy applications or as back-up sensors for low Earth orbit (LEO) missions.

Gyroscopes

Gyroscopes are inertial sensors which determine the attitude by measuring the speed or angle of rotation of the spacecraft from initial reference without any knowledge of an external or absolute reference. They are located internal to the spacecraft and work at all points in an orbit. Since they measure a change instead of absolute attitude, gyroscopes must be used along with other attitude hardware to obtain full measurements.

3.6.2 Attitude Actuators

An actuator is the mechanism that supplies control torque or force for the attitude control system. The most common sources of force/torque are gas thrusters, magnetorquers and reaction wheels [88,90].

Magnetic Torquers

Magnetic torquers are used to generate magnetic dipole moment for attitude control. They apply a torque on the satellite by producing a magnetic field which interacts with the earth's magnetic field.

Thrusters

All thrusters produce thrust by expelling propellant in the opposite direction. Gas thrusters can be hot gas, when energy is derived from a chemical reaction or cold gas type when energy is derived from the latent heat of a phase change. The obtained torques or forces can be used to control attitude, spin rate, speed of momentum wheels, and to adjust orbits. Gas jets or magnetic coils can be used for the same purposes at low Earth orbits (LEO). The main limitation on the use of thrusters is the required propellant supply. Fuel budget is an important part of mission planning for any system using gas thrusters. Gas thrusters also have complex and expensive plumbing systems.

Reaction Wheel

Reaction wheels use the rotational variant of Newton's third law. When the motor applies a torque to speed up or slow down the rotor, it produces a reacting torque on the body of the satellite [90]. Since the satellite is essentially a closed system, the total angular momentum of the satellite body plus the reaction wheels is constant. Thus any change in the angular momentum of a reaction wheel results in an equal and opposite change of the angular momentum of the satellite body. Reaction wheels are effective active control elements. They are particularly good for variable spin

rate control. Active control of spacecraft by using reaction wheels is a fast, flexible, precise way of attitude control and stabilization. On the other hand, it requires rapidly moving parts which implies problems of support and friction. Normally, three reaction wheels are used to control a satellite, with the wheel axes aligned with the body principal axes. In the next section the high fidelity mathematical model for reaction wheel actuators, that are used in our simulations to generate data, will be described.

3.7 Mathematical Model of Reaction Wheel Actuators

A high-fidelity nonlinear model of a reaction wheel has been obtained from Bialke [92] and has been integrated into the ACS dynamics. A block diagram representation of this high-fidelity reaction wheel model is shown in Figure 3.5. The reaction wheels considered in this thesis are ITHACO "type A" reaction wheels. The values of model parameters for this type of wheel are also obtained from [92] and are given in Table 3.1. As Fig 3.5 illustrates, there are five main blocks in the reaction wheel model, motor torque control, speed limiter, EMF torque limiting, motor disturbances and bearing friction and disturbances.

Motor Torque Control Block

This block consists of voltage controlled current source with a gain, G_d. The result is a motor current directly proportional to the torque command voltage. The motor has a torque constant K_t which produces torque proportional to the current driven I_m into it. The torque command voltage is restricted to be within [-5,+5].

Speed Limiter Block

The function of a speed limier block is to prevent the reaction wheel from reaching unsafe speeds. Once the wheel ω speed exceeds an establishes speed threshold ω_s,

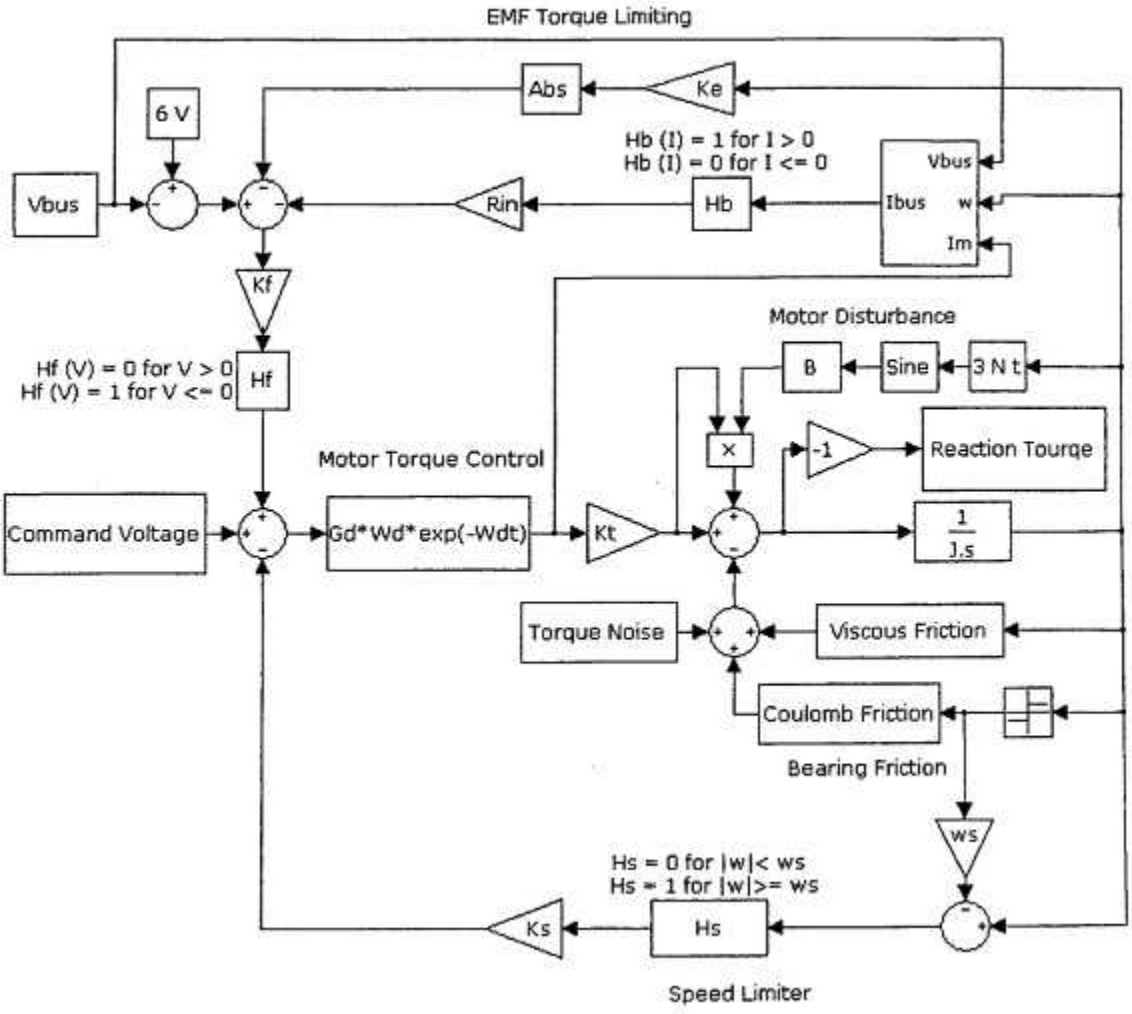

Figure 3.5: Detailed reaction wheel block diagram [92].

Table 3.1: Reaction wheel model constants [92].

Variable	Nomenclature	Unit	Value
G_d	Driver Gain	A/V	0.19
K_t	Motor Torque Constant	$N-m/A$	0.029
K_e	Motor Back-EMF	$V/rad/sec$	0.029
K_s	Overspeed Circuit Gain	$V/rad/sec$	95
ω_s	Overspeed Circuit Threshold	rad/sec	690
ω_d	Driver Bandwidth	rad/sec	2000
τ_c	Coulomb Fiction	$N-m$	0.002
J	Flywheel Inertia	$N-m-s^2$	0.0077
N	Number of Motor Poles	—	36
B	Cogging Torque Amplitude	$N-m$	Zero
R_{in}	Input Resistance	Ω	2
K_f	Voltage Feedback Gain	V/V	0.5
P_q	Quiescent Power	W	3
ω_a	Torque Noise High Pass Filter Frequency	rad/sec	0.2
θ_a	Torque Noise Angle Deviation	rad	0.05
R_b	Bridge Resistance	Ω	2
	Torque command range	V	$[-5,+5]$

the circuit provides a high gain negative feedback K_s into the torque command. The heavy-side function H_s utilize to enables the negative feedback.

EMF Torque Limiting Block

In the low bus voltage condition, when reaction wheel runs at high speed the back-EMF of the motor is increased and the motor torque may be limited. This eventually eliminates the voltage headroom and reduces torque capacity. From the disturbance stand point, since the motor torque is coupled directly to the bus voltage any fluctuations in the bus voltage will be felt as torque disturbances. The nonlinear relationship between I_{bus} and V_{bus} is defined as

$$I_{bus} = \frac{I_m^2 R_B + 0.04\,|I_M|\,V_{bus} + P_q + \omega I_m k_e}{V_{bus} - 1} \tag{3.22}$$

In order to eliminate the voltage drop when power is not being drown from the bus a heavy-side function H_B is included in the block.

Motor Disturbance Block

The motor torque in reaction wheel can be a source of very high frequency disturbances due to the motor excitation and the magnetic construction. Recent reaction wheels include brushless DC motors that exhibit torque ripple at the commutation frequency and cogging at a frequency corresponding to the number of motor poles and rate of rotation. Torque ripple is defined as amount of variation in the motor torque due to the commutation method and the shape of the back-EMF. The amount of spacecraft disturbances due to torque ripple is highly dependent on the torque ripple frequency. Cogging is a disturbance torque which is always present in a conventional brushless DC motor. ITHACO's zero cogging motor completely eliminates this potential source of jitter.

Bearing Friction and Disturbances Block

The friction in a reaction wheel mathematically is divided into viscous friction and coulomb friction. The viscous friction τ_v varies with speed and temperature and generated in the bearing due to the bearing lubricant. Since the viscosity is temperature dependent the lubricant has a strong sensitivity to temperature. This drag torque for ITHACO's reaction wheel is defined as

$$\tau_v = (0.049 - \frac{0.0002}{^oC}(T + 30^oC)) \quad \frac{mN - m}{rad/sec} \tag{3.23}$$

The coulomb friction is constant with polarity dependent on the direction of rotation of the reaction wheel. It is caused by rolling friction within the bearings. The loss in torque is independent of wheel speed and temperature.

Torque Noise

Torque noise is the very low frequency torque variations from the bearings due to lubricant dynamics. It is a function of lubricant behavior and it has the most significant effect on the spacecraft pointing accuracy. This noise can be modeled as a sine

wave with a high pass filter frequency as

$$\tau_a = J\theta_a\omega_a^2 sin\omega_a t \tag{3.24}$$

3.8 Mathematical Model of External Attitude Disturbances

The attitude control subsystem of an Earth-orbiting satellite must tolerate the typical external disturbance torques due to the gravity-gradient effects, the Earth's magnetic field, aerodynamic torques (dominant in the low-altitude orbits), and solar radiation torque. Therefore, all these environmental disturbances need to be modeled and properly incorporated into the ACS simulator to be able to evaluate the robustness of the proposed fault detection and isolation algorithms with respect to them. As a result, the following mathematical models of these disturbances are obtained from [88] and are incorporated into the ACS simulator.

3.8.1 Solar Radiation

Solar radiation pressure produces a force on the satellite related to its distance to the sun. Solar radiation has more effect at high altitudes. Surface area of the satellite which faces the Sun is essential when determining the resulting acceleration caused by solar radiation. Worst-case solar radiation torque is estimated as:

$$\tau_s = \frac{F_s}{c} A_s(1+r).cosi_s.(c_{ps} - c_g) \tag{3.25}$$

where F_s is the solar constant, c is the speed of the light in m/s, A_s is the surface area for solar radiation in m^2, r is the coefficient of reflectivity, i_s is the sun incidence angle, c_{ps} is the location of the center of solar pressure, and c_g is the center of gravity. Coefficient of reflectivity r is a number between 0 and 1 with usual value of 0.6 for most of satellites. In order to consider worst case this parameter is considered as 1 in our simulations.

3.8.2 Gravity-Gradient Torque

Any non-symmetrical object in the orbit is affected by a gravitational torque because of the variation in the Earth's gravitational force over the object. There are many mathematical models for gravity gradient torque. The most common one is derived by assuming homogeneous mass distribution of the Earth as follows:

$$\tau_g = \frac{3\mu(I_x - I_y)sin(2\theta)}{2R^3} \tag{3.26}$$

where τ_g is the max gravity torque, μ is the Earth's gravity constant in $\frac{m^3}{s^2}$, R is the orbit radius in meter, θ is the maximum deviation of the z-axis from local vertical in radians, I_x and I_y are moments of inertia about x and y axes in $kg.m^2$.

3.8.3 Aerodynamic Drag

This disturbance is most effective on satellites orbiting below 400-500 km. The drag force created by the air molecule interaction with satellite body produce a torque on the satellite, thus reducing its velocity and resulting in a lower orbit for the satellite. This torque is derived as:

$$\tau_a = 0.5(\rho c_D A_{aero} V^2)(c_{pa} - c_g) \tag{3.27}$$

where ρ is the atmospheric density in kg/m^3, c_D is the drag coefficient, which is between 2 and 2.5, A_{aero} is the surface area for aerodynamic pressure in m^2, V is the satellite velocity, c_{pa} is the center of aerodynamic pressure, and c_g is the center of gravity.

3.8.4 Magnetic Torque

This torque is resulting from the interaction of the geomagnetic field and spacecraft's residual magnetic field. The worst-case magnetic torque is estimated as:

$$\tau_m = D_r E_{mf} \tag{3.28}$$

where D_r is the residual dipole of the satellite in $amp - turn.m^2$, $E_{mf} = \frac{2M}{R^3}$ is the Earth's magnetic field in Tesla, M is the magnetic moment of the Earth in $Tesla.m^3$, and R is the orbit radius or radius from the dipole (Earth) center to the satellite in meter.

The values of the entire set of parameters of the environmental models are provided in Table 3.2. The values of all the four external attitude disturbances are provided in Table 3.3.

Table 3.2: Parameters of the disturbance models used in the ACS simulations.

Parameter	Description	Units	Value
ρ	Atmospheric density	kg/m^3	1.04 e-13
A_{aero}	Contact surface aera for aerodynamic pressure	m^2	1
A_s	Contact surface area for solar radiation	m^2	1
c_D	The drag coefficient		2.2
c_{pa}	The center of aerodynamic pressure		0.1
c_g	The center of gravity		0
c_{ps}	The center of solar pressure		0.1
M	Magnetic moment of Earth	$T.m^3$	7.96e15
D_r	Residual dipole of the satellite	$Amp - turn.m^2$	0.8
F_s	Solar constant	W/m^2	1366
r	Reflectance factor		1
θ	Maximum deviation in the local-vertical pointing	rad	$1.74e-4$
i_s	Incidence angle	deg	0

Table 3.3: Torque disturbances applied to the Spacecraft (Nm).

Parameter	Description	Value
$\tau_{gravity}$	Gravity gradient torque	$4.7e-6$
τ_{aero}	Aerodynamic drag torque	$6.5e-7$
$\tau_{magnetic}$	Magnetic torque	$2.4e-5$
τ_{solar}	Solar Radiation Torque	$9e-7$

3.9 Conclusions

In this chapter, the coordinate systems that are used for spacecraft maneuvers calculations have been explained and different attitude representations for spacecraft have

been provided. The dynamics of satellite and the architecture of formation flying control laws have been provided. Different sensors and actuators that are utilized in spacecraft are presented and the mathematical model for a reaction wheel has been explained. Finally, different attitude disturbance torques that effect the spacecraft attitude maneuvers have been provided and the mathematical models for the disturbance torques are provided as well.

Chapter 4

Spacecraft-level Fault Detection, Isolation and Identification

The development of efficient algorithms that can autonomously detect and isolate faults in spacecraft have been widely investigated during past decades. The complex system like autonomous spacecraft and formation of spacecraft require intelligent and autonomous technologies that can perform fault diagnosis in spacecraft with high level of accuracy and precision. The accuracy and precision of fault diagnosis scheme are strongly dependent on the availability of mathematical models of system. In complex and nonlinear systems like spacecraft, developing precise models for all components can be quite difficult. Due to these limitations in this chapter we propose our wavelet-entropy spacecraft-level fault detection scheme on a three-axis ACS model. The capability of wavelet entropy in detecting changes in signals make it a good choice for use in fault analysis problems. A discrete wavelet transform (DWT) is used to extract features from the original signals and wavelet entropy is used as a measure of degree of chaos in the signal for detecting the faults. It is important to note that in spacecraft-level fault diagnosis scheme, the absolute attitude measurements from each satellite in the formation is considered as the diagnostic signals.

4.1 Discrete Wavelet Transform and Wavelet Entropy

4.1.1 Wavelet Transform Approach

The Wavelet Transform [107] provides a time-frequency representation of a signal. It was developed to overcome the short coming of the Short Time Fourier Transform (STFT), which can also be used to analyze non-stationary signals. While STFT gives a constant resolution at all frequencies, the Wavelet Transform uses a multi-resolution technique by which different frequencies are analyzed with different resolutions, namely

$$CWT(\tau, s) = \int_{-\infty}^{\infty} x(t) \frac{1}{\sqrt{s}} \psi^* \left(\frac{t-\tau}{s} \right) \tag{4.1}$$

The Continuous Wavelet Transform (CWT) is provided by equation (4.1), where $x(t)$ is the signal to be analyzed, τ, s are translation and scale parameters respectively, $\psi(t)$ is a mother wavelet and " $*$ " denotes a complex conjugate.

All the wavelet functions used in the transformation are derived from the mother wavelet through translation (shifting) and scaling [107]. The translation parameter τ relates to the location of the wavelet function as it is shifted through the signal. Thus, it corresponds to the time information in the Wavelet Transform. The scale parameter s is defined as $|1/frequency|$ and corresponds to the frequency information. Scaling either dilates (expands) or compresses a signal. Large scales (low frequencies) dilate the signal and provide detailed information hidden in the signal, while small scales (high frequencies) compress the signal and provide global information about the signal. The Discrete Wavelet Transform (DWT) [107], which is based on sub-band coding, is found to yield a fast computation of the Wavelet Transform. It is easy to implement and reduces the computation time and resources required. In the case of DWT, a time-scale representation of the digital signal is obtained by using digital filtering techniques. The signal to be analyzed is passed through filters with different cutoff frequencies at different scales. The DWT is computed by successive low-pass and high-pass filtering of the discrete time-domain signal. This is called the Mallat algorithm or the Mallat-tree decomposition [94]. The Discrete Wavelet Transform is

defined as follows

$$DWT\left(m,n\right)=2^{\frac{-m}{2}}\sum_{m}\sum_{n}x\left(n\right)\psi^{*}\left(\frac{t-n2^{m}}{2^{m}}\right)\qquad m,n\in Z \tag{4.2}$$

At each level of decomposition, the high pass filter produces details, while the low pass filter associated with scaling function produces approximations.

4.1.2 Wavelet Energy and Wavelet Entropy

4.1.3 Wavelet Energy

As stated previously, wavelet transform of a transient signal is expressed by multi-resolution decomposition fast algorithm which utilizes the wavelet bases to decompose the signal to components under different scales. It is equal to recursively filtering the signal with a high-pass and low-pass filter pairs. The approximations are the high-scale, that is low frequency components of the signal produced by filtering the signal by a low-pass filter. The details are the low-scale, that is high frequency components of the signal produced by filtering the signal by a high-pass filter. After each level of decomposition, the sampling frequency is reduced by half. Then recursively one decomposes the low-pass filter outputs (approximations) to produce the components of the next stage.

Given a discrete signal $x[n]$, that is being transformed at instant k and scale j, it has a high-frequency component coefficient $D[k]$ and a low-frequency component coefficient $A[k]$. The frequency band of the information contained in the signal components $D[k]$ and $A[k]$, obtained by reconstruction are as follows

$$D_j[k]:[2^{-(j+1)}f_s,2^{-j}f_s] \tag{4.3}$$

$$A_j[k]:[0,2^{-(j+1)}f_s] \tag{4.4}$$

where f_s is the sampling frequency. The original signal sequence $x[n]$ can be repre-

sented by the sum of all components as follows

$$x[n] = D_1[n] + A_1[n] = D_1[n] + D_2[n] + A_2[n] \quad (4.5)$$

$$= \sum_{j=1}^{J} D_j[n] + A_J[n] \quad (4.6)$$

The equation (4.5) indicates that in the first level of decomposition, $x[n]$ is decomposed into approximation $A_1[n]$ and detail $D_1[n]$ and the next higher scale decomposition is based on $A_1[n]$ instead of $x[n]$ i.e. in the next level of decomposition the approximation $A_1[n]$ is decomposed into the detail $D_2[n]$ and approximation $A_2[n]$. Since the wavelet bases are orthogonal, these decomposed signals could be regarded as a direct estimation of local energies at different scales.

Thus, the wavelet energy of detail and approximation components at instant k and scale j will be represented as follows

$$E_{j,k} = |D_j[k]|^2 \quad k = 1, 2, ..., N \quad (4.7)$$

$$E_{J+1,k} = |A_J[k]|^2 \quad k = 1, 2, ..., N \quad (4.8)$$

where N denotes the number of samples data at scale j.

The wavelet energy at each scale could be described as

$$E_j = \sum_{k=1}^{N} E_{j,k} \quad j = 1, 2, ..., J+1 \quad (4.9)$$

where (J+1) scale denotes the approximation component. The total wavelet energy is defined as

$$E_{tot} = \sum_{j=1}^{J+1} E_j \quad (4.10)$$

4.1.4 Wavelet Entropy

The concept of entropy is derived from thermodynamic entropy, which can be seen as a measure of the degree of system chaos. Entropy is a common concept in many fields. In mathematics, entropy is used to measure the uncertainty of problems. While in the

information science, entropy is the average uncertainty of the information source. In other word, entropy is a measure of irregularity of states such as imbalance and uncertainty. A method for measuring the entropy appears as an ideal tool for quantifying the ordering of non-stationary signals. In the information field, Shannon entropy [93] represents the degree of chaos of a system. It provides an efficient criterion for analyzing and comparing probability distributions. The Shannon entropy is defined as follows:

Given a random variable X which takes a finite number of possible values $x_1, x_2, ..., x_n$ with probabilities $p_1, p_2, ..., p_n$, respectively, the Shannon entropy is defined as [97]:

$$H(X) = -\sum_{i=1}^{n} p_i log(p_i) \tag{4.11}$$

The concept of wavelet entropy is inherited from the Shannon entropy. When a fault appears in the diagnostic signal, the amplitude and frequency of the diagnostic signal will change as the system changes from the normal state to the faulty state. The Shannon entropy will change accordingly. Wavelet combined entropy [93] can make full use of localized features at the time-frequency domains as wavelet analysis deals with unsteady signals and can embody the ability where the information entropy manifests the signal information.

Therefore, wavelet entropy not only can achieve the purpose of information emergence, but also can analyze faulty signals more efficiently. Many types of wavelet entropies have been defined [93] to solve different problems, and these methods can achieve good detection and recognition performance. In this work, the Shannon entropy is used to extract the features from signals.

The definition of Shannon entropy is as follows [93]

$$Entropy = -\sum_{k} E_{j,k} \log E_{j,k} \tag{4.12}$$

where $E_{j,k}$ is the wavelet energy spectrum at scale j and at the instant k.

Window-Wavelet Entropy Approach

The wavelet entropy represents the degree of chaos of the measured signal which can provide useful information about the underlying state of the system. However, in critical circumstances, such as reaction wheel operation in a satellite, actuator faults should be detected immediately.

Gathering a large amount of data and performing a post-analysis is not practical. Therefore, the traditional wavelets transform needs to be improved for real-time wavelet analysis. To provide a real-time fault detection, window wavelet technique is added to the diagnostic basis signal. To obtain the real-time wavelet entropy of $x(n)$ at instant k, a window of the time series must be picked out, i.e. $x_w(n) = x(k-W+1), ..., x(k)$ where $k-W+1 \succ 0$, $n = k-W+1,\ k-W+2, ..., k$ and W is the width of the window. When a higher value for W is chosen more information could be obtained, however, this implies more storage and calculations. Therefore, the proper value of W must be considered. By selecting a proper value for W, wavelet decomposition of a signal is produced as

$$x_w(n) = A_{wJ}(n) + \sum_{j=1}^{J} D_{wj}(n) \qquad n = k-W+1, ..., k \tag{4.13}$$

As defined in equations (4.9) and (4.10), the wavelet energy at each scale and total wavelet energy is defined as

$$E_{wj} = \sum_{n=k-w+1}^{k} |A_{wJ}(n)|^2 + \sum_{j=1}^{J} \sum_{n=k-w+1}^{k} |D_{wj}(n)|^2 \quad j = 1, 2, ..., J+1 \tag{4.14}$$

$$E_{wtotal} = \sum_{j=1}^{J+1} E_{wj} \quad j = 1, 2, ..., J+1 \tag{4.15}$$

The relative wavelet energy is now defined as follows

$$P_j = \frac{E_{wj}}{E_{wtotal}} \quad j = 1, 2, ..., J+1 \tag{4.16}$$

In equation (4.16), P_j represents the distribution of wavelet energy at different scales.

According to equation (4.11) and (4.16), the wavelet entropy (WE) for each window is now defined as follow

$$WE = -\sum_{j=1}^{J+1} P_j log(P_j) \tag{4.17}$$

4.2 Wavelet-Entropy Fault Detection Scheme

4.2.1 Proposed Fault Detection Algorithm

In our proposed fault detection scheme, wavelet entropy is used for spacecraft fault detection. The main objective of wavelet analysis is to decompose signals into several frequency bands. For the analysis of signals using discrete wavelet transform, selection of appropriate wavelet and the number of decomposition levels are very important. During the occurrence of faults, the amplitude and frequency characteristics of the signal will change and the entropy will change accordingly. Wavelet combined entropy can make full use of localized features at time-frequency domains.

The first step in the fault detection scheme is generating diagnostic signal that must be monitored for fault detection purposes. In our proposed fault detection scheme, the absolute attitude measurements in a satellite in terms of quaternion parameters are considered. The proposed wavelet entropy fault detection scheme is described as follows

- Diagnostic Signals: In the first step of our fault detection approach, the absolute attitude measurements in a satellite in terms of quaternion parameters are considered as monitored signals for fault detection purposes. In this step the quaternion signals; q_1, q_2, q_3 are considered for the next step.

- Window Discrete Wavelet Transform (WDWT): In this step, diagnostic signals are decomposed into details and approximation coefficients using the WDWT technique. In the WDWT technique, the proper window size must be selected. When a higher value for window size is chosen more information could be obtained, however, this implies more storage and calculations. Therefore, a proper value of window size must be considered. In our simulations Daubechies wavelet

[107,116] is selected and the number of decomposition levels for fault detection step was chosen to be 2.

- Sum of Absolute Wavelet Entropy (SAWE): In this step, for each diagnostic signal, the absolute wavelet entropy (AWE) of the produced coefficients is calculated and then these absolute entropies are summed. In this step the SAWE for each window is calculated as follows

$$SAWE = \sum_{i=1}^{4} abs\left(-\sum_{j=1}^{J+1} P_j log(P_j)\right) \tag{4.18}$$

  where J is the decomposition level of the wavelet transform. In our simulations we set $J = 2$.

- Fault Detection: The fault detection is accomplished by comparing the value of the SAWE to a defined threshold. The fault will be detected if the SAWE passes the threshold. Otherwise, the satellite is determined to be in a normal or healthy condition.

In our fault detection scheme, in order to prevent false alarms due to noise in the system when the SAWE passes a threshold, there is a time delay for declaring the faulty condition by the fault diagnosis module, i.e. when the SAWE passes the thresholds and this condition remains for period of σ seconds, then the faulty condition is established. However, this delay may result in the fault detection times to become longer but it prevents it from generating false alarms in our fault diagnosis system.

4.2.2 Time-varying Threshold Technique

Robustness in fault detection systems is the essential property that is required for operation in the presence of disturbances and noise while maintaining sensitivity to faults. This robustness could be achieved by defining time-varying thresholds [120] in a fault detection scheme. In our proposed fault detection algotithm instead of using fix thresholds, time-varying thresholds are considered. In our proposed method, two

time-varying thresholds are considered to cover the monitored signal. These time-varying thresholds consist of a filter, with leads the behavior that is driven by the diagnostic signal. Figure 4.1 illustrates the schematic of the time-varying threshold technique that is utilized.

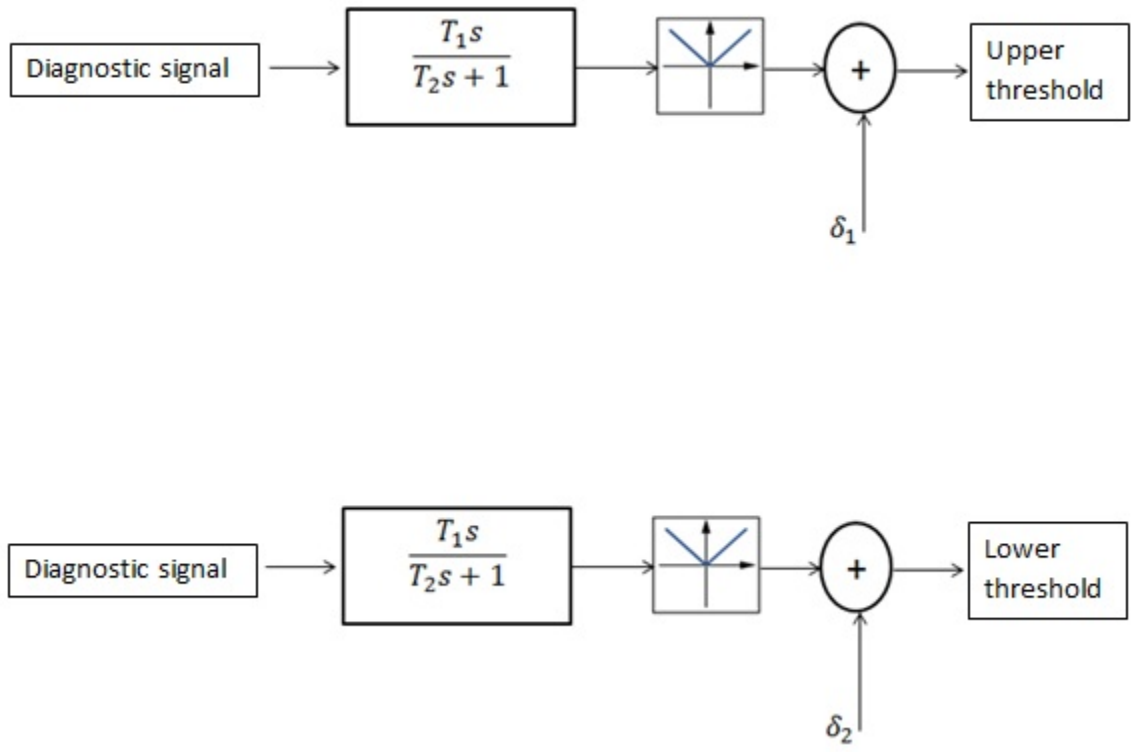

Figure 4.1: Generation of a time-varying thresholds [120].

In this schematic, δ_1 and δ_2 denote the sensitivity parameters that are used to adjust the thresholds and T_1 and T_2 are constants that are determined in the healthy condition of a satellite. For the threshold, the parameters $\delta_1,\ \delta_2,\ T_1$ and T_2 are defined by comparing the SAWE of a satellite under different healthy scenarios. After these parameters are calculated the thresholds are calculated online in real-time. Under the healthy scenario, the values for δ_1 and δ_2 are defined so that these values produce two thresholds to cover the signals and detect faults in the system.

When the fault is injected in the reaction wheel, the SAWE of the satellite changes and if it passes the threshold, in this condition the fault is said to be detected. The

flow chart of our proposed fault detection algorithm is illustrated in Figure 4.2.

4.3 Characterization of Possible Fault Scenarios in Reaction Wheels

In order to be able to develop the fault detection algorithm and to inject faults in the ACS, the potential sources of faults in the reaction wheels must be identified. Extensive experimental experience with reaction wheels in different satellite missions has revealed that the following potential failures may occur in these actuators, namely

- Unexpected changes in the Bus Voltage (V_{bus});
- Unexpected changes in the motor current (I_m); and
- Viscous temperature faults.

There are three possible fault scenarios in the reaction wheel actuators and for each fault scenario the proposed fault detection algorithm is performed to verify the capability of our proposed fault detection algorithm in the ACS of a satellite.

4.4 Simulation of the Reaction Wheel Operation

The simulations performed in this thesis have been implemented in Matlab and Simulink. Using the high-fidelity mathematical model of the reaction wheel presented in Chapter 3, we have simulated the reaction wheel behavior for the generated torque in a satellite. It is important to note that in order to perform fault analysis, the absolute attitude measurements of a satellite in terms of quaternion parameters is used as a diagnostic signal and the reaction wheel itself, though being an actuator of the ACS, is not considered as the system being monitored directly.

In our simulations three reaction wheels are used in a 3-axis stabilized satellite for the attitude control and in order to detect faults one fault analysis module need to be dedicated for health monitoring in the ACS of the satellite. It is important to

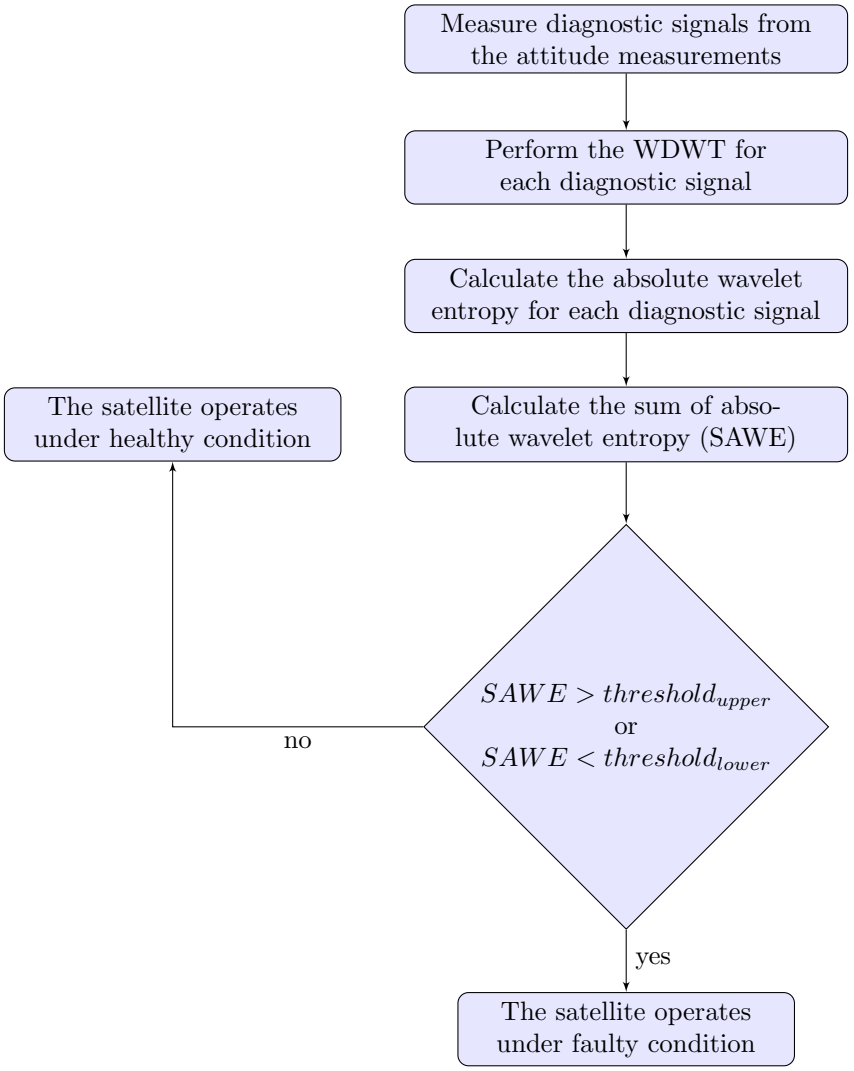

Figure 4.2: Flow chart of the proposed fault detection algorithm.

note that in our simulations all fault validation results are obtained with a Gaussian random noise for the attitude measurements.

Table 4.1: Simulation parameters for a satellite.

Parameters	Value
Weight	120 Kg
Inertia Moment	Ix = 9.8, Iy = 9.7, Iz = 9.75 Kgm2
Orbit	680 Km
Orbital attitude period	97 min
Initial Euler Angles	[2,6,4]
Desired Euler Angles	[15,25,50]
Desired angular velocity	[0,0,0]

Our simulation data are obtained from the closed-loop ACS simulation of a 3-axis stabilized LEO satellite. The simulations are carried out for 1000 sec of the ACS operation and the simulated LEO satellite was in an altitude of about 680 km. The simulation parameters are shown in Table 4.1.

4.4.1 Reaction Wheel Operation in the Healthy Condition

In the healthy (normal) condition, the reaction wheel works with its nominal specifications and generates proper torque for a satellite. The parameters δ in threshold formula is calculated based on the results under this condition, i.e. the process of determining proper threshold is based on different operation of a satellite under healthy conditions.

In order to determine the proper value for δ, different attitude missions in a satellite in healthy operation condition are considered and the average of SAWEs for each mission is calculated. By considering these SAWEs in the healthy operation condition in a satellite the δ_1 and δ_2 are defined. These attitude missions and the average of SAWEs for each mission are illustrated in Table 4.2.

In our simulations in this section the parameters δ_1, δ_2, T_1 and T_2 are chosen as:

$$\delta_1 = 0.00182 \quad \delta_2 = 0.00165 \quad T_1 = 6 \quad T_2 = 0.4$$

Table 4.2: The average of SAWEs in different attitude missions in healthy operation condition in a satellite.

Desired attitude	Average of the SAWEs	Desired attitude	Average of the SAWEs
$[24, 209, 168]$	1.7572 e-3	$[89, 25, 17]$	1.7840 e-3
$[160, 110, 31]$	1.7620 e-3	$[43, 13, 80]$	1.7885 e-3
$[355, 126, 200]$	1.7674 e-3	$[340, 130, 300]$	1.7945 e-3
$[297, 303, 290]$	1.7437 e-3	$[30, 310, 45]$	1.7802 e-3
$[97, 257, 35]$	1.7400 e-3	$[124, 44, 19]$	1.7913 e-3
$[341, 166, 350]$	1.7423 e-3	$[90, 0, 0]$	1.7900 e-3
$[15, 40, 76]$	1.7541 e-3	$[173, 137, 86]$	1.7873 e-3
$[72, 64, 56]$	1.7557 e-3	$[45, 45, 45]$	1.7799 e-3
$[84, 279, 159]$	1.7563 e-3	$[20, 333, 31]$	1.7535 e-3
$[85, 66, 164]$	1.7767 e-3	$[0, 90, 0]$	1.7605 e-3
$[30, 45, 60]$	1.7839 e-3	$[180, 100, 57]$	1.7617 e-3
$[82, 3, 23]$	1.7818 e-3	$[0, 0, 90]$	1.7567 e-3
$[50, 29, 13]$	1.7414 e-3	$[22, 145, 35]$	1.7590 e-3
$[114, 227, 120]$	1.7603 e-3	$[10, 25, 90]$	1.7619 e-3
$[33, 89, 165]$	1.7585 e-3	$[30, 30, 30]$	1.7609 e-3
$[108, 130, 207]$	1.7664 e-3	$[43, 80, 34]$	1.7577 e-3
$[62, 11, 83]$	1.7616 e-3	$[12, 25, 46]$	1.7594 e-3
$[39, 103, 331]$	1.7634 e-3	$[90, 90, 90]$	1.7706 e-3
$[15, 25, 50]$	1.7621 e-3	$[67, 87, 69]$	1.7823 e-3
$[41, 60, 18]$	1.7813 e-3	$[13, 83, 41]$	1.7734 e-3

It is important to note that the fault analysis in a satellite is performed in steady state. In our simulations the satellite has reached its steady state condition after $t = 300sec$, hence the parameters δ_1 and $\delta)2$ are chosen based on the steady state charactristics of a system. Due to noise in the satellite attitude measurements, if we chose the smaller values for δ_1 and δ_2, the false alarms are increased in a monitored system, however larger values for these parameters can decrease the ability of detecting low severity faults in the reaction wheel. The time delay parameter σ is chosen as $\sigma = 10$ sec.

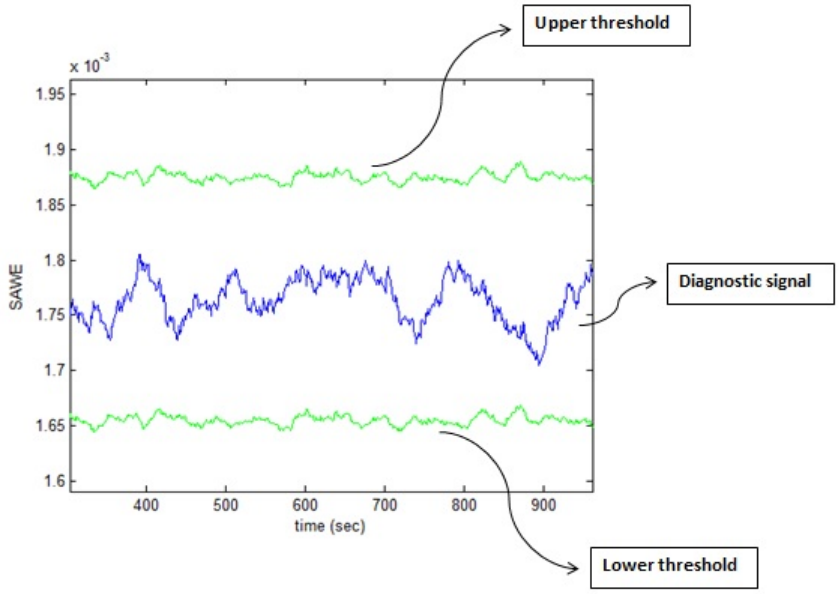

Figure 4.3: SAWE of a satellite under the healthy condition.

The SAWE of a satellite under a healthy condition and the thresholds are illustrated in Figure 4.3. As mentioned before, the window wavelet entropy technique is used in our proposed scheme and SAWE is calculated for each window. In our simulations the window size is selected as $W = 350$. If the lower values for window size are selected, some faults cannot be detected in the reaction wheel and if the higher values are selected the computations and storage capacity becomes more complex and larger. The comparison between different window sizes will be illustrated in Section 4.5.

4.4.2 Reaction Wheel Operation under Bus Voltage Fault Scenario

In this fault scenario, low bus voltage condition is considered as a fault in a reaction wheel. In order to simulate this fault scenario, bus voltage is dropped by 25%, 26%, 27%, 28%, 29%, 30%, 31%, 32%, 33%, 34%, 35%, 36%, 37%, 38%, 39% and 40% from its nominal value (Nominal value =24 volt). These faults are injected to a reaction wheel in the steady state condition at $t = 600sec$.

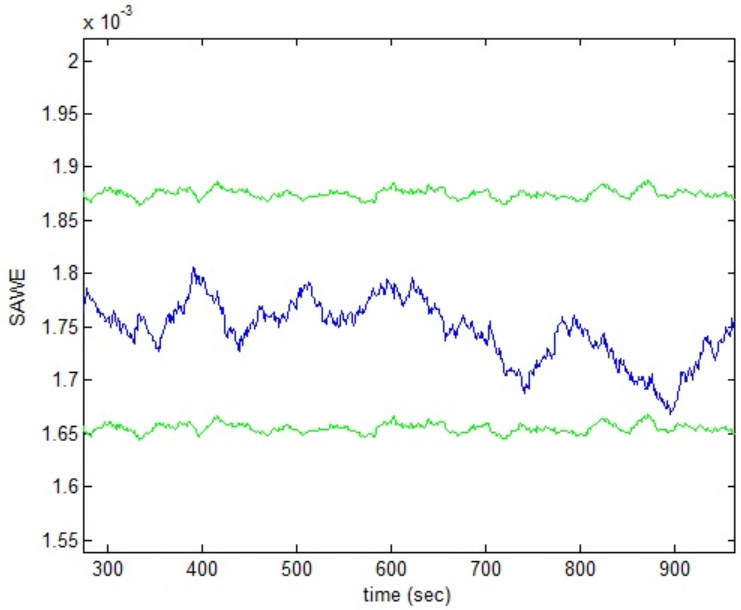

Figure 4.4: SAWE of the satellite for a 27% drop in the bus voltage.

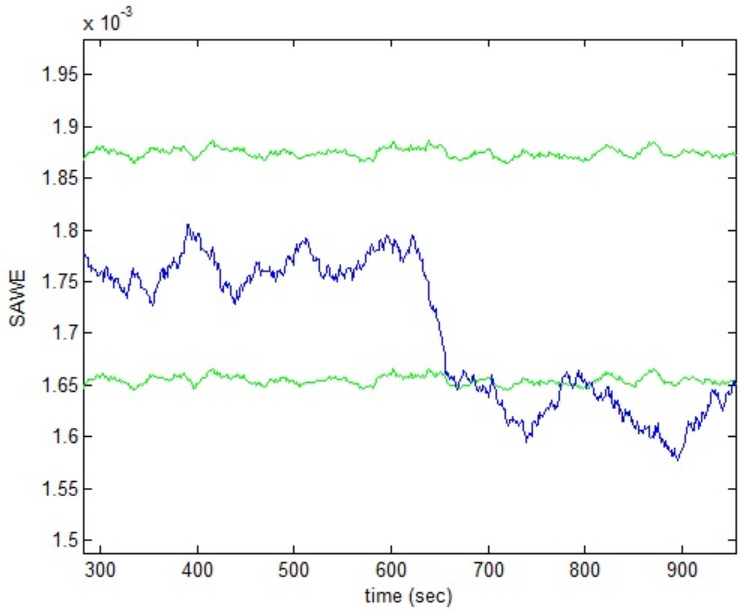

Figure 4.5: SAWE of the satellite for a 28% drop in the bus voltage.

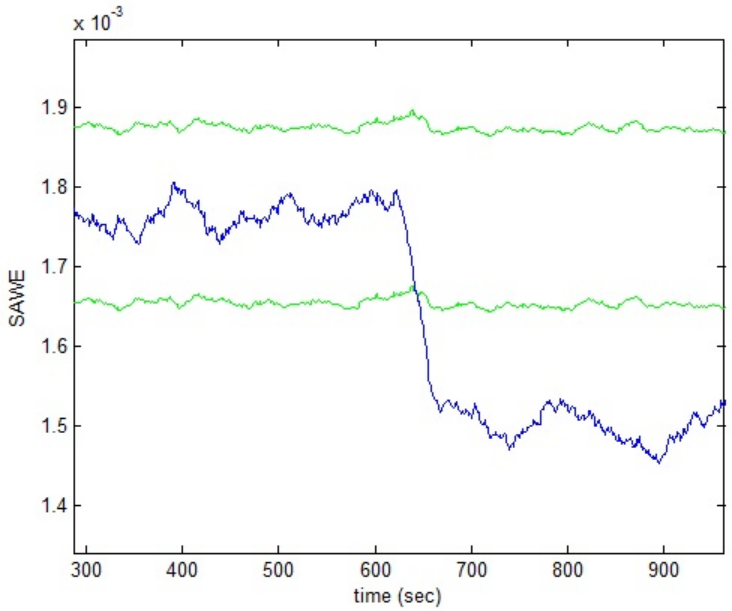

Figure 4.6: SAWE of the satellite for a 29% drop in the bus voltage.

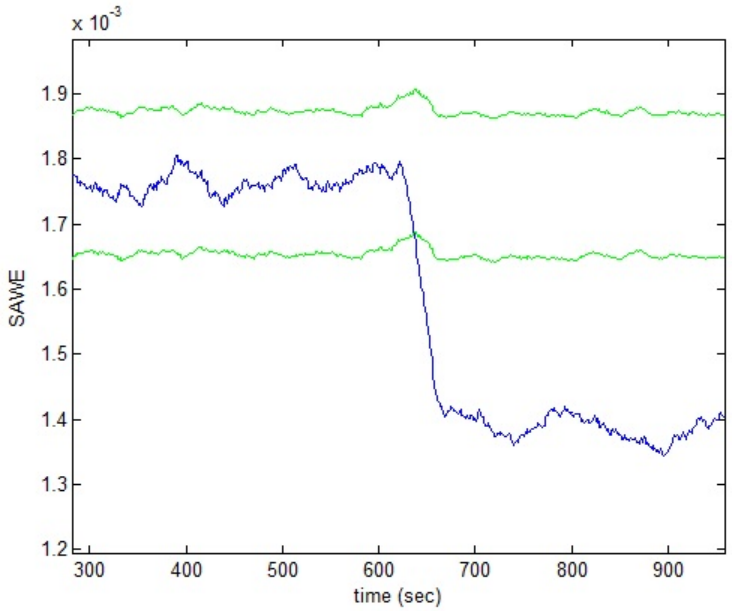

Figure 4.7: SAWE of the satellite for a 30% drop in the bus voltage.

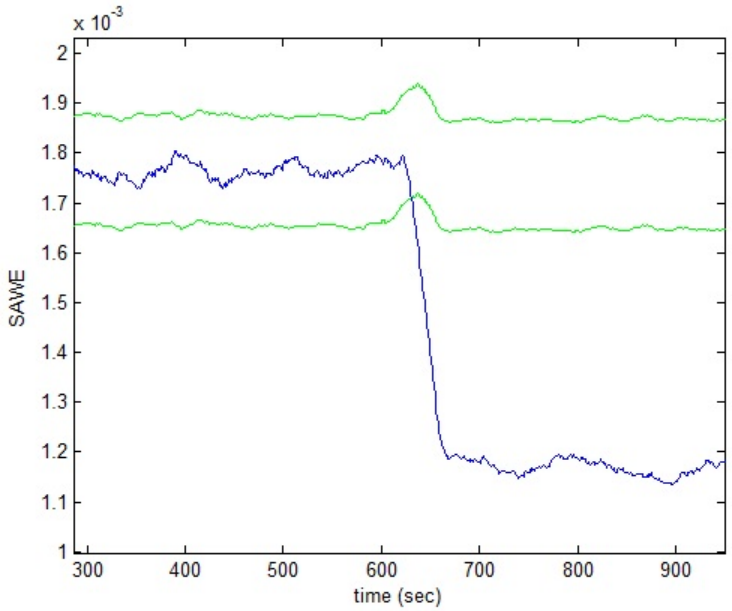

Figure 4.8: SAWE of the satellite for a 33% drop in the bus voltage.

The SAWE of the satellite in this fault scenario is illustrated in Figures 4.4, 4.5, 4.6, 4.7 and 4.8.

As the results in these figures indicate, when the bus voltage is dropped by 27%,

the SAWE didn't pass the threshold and in these cases the fault is not detected. When the bus voltage dropped by 28% the SAWE passes the thresholds but the system has false alarm and when the bus voltage is dropped by at least 28%, the SAWE is changed consequently and has passed the threshold, hence the fault is detected.

Table 4.3: Fault detection time in bus voltage fault scenario.

Percentage drop in bus voltage	Fault injection time (second)	Fault detection time (second)
25	600	Not detected
26	600	Not detected
27	600	Not detected
28	600	Not detected
29	600	647
30	600	647
31	600	644
32	600	642
33	600	641
34	600	640
35	600	639
36	600	638
37	600	638
38	600	637
39	600	636
40	600	636

The fault detection times are indicated in Table 4.3. The results in Table 4.3 indicate that our proposed fault detection scheme can detect at least 29% drop in bus voltage faults in a short and proper time period, however for lower than 29% drop in the bus voltage this scheme can not detect the injected faults.

4.4.3 Reaction Wheel Operation under Motor Current Fault Scenario

The generated motor current from the motor control torque block is proportional to the torque command voltage and the current is converted into torque through the motor torque gain K_t. Therefore, any injected fault in the motor torque gain will be reflected directly as fluctuations in the motor current and as result in the motor torque.

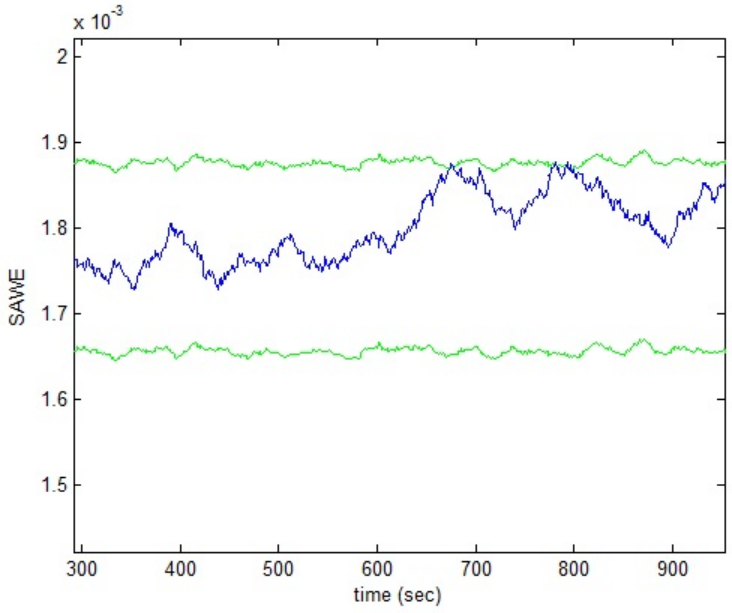

Figure 4.9: SAWE of the satellite for a 4% drop of the motor gain torque in the reaction wheel.

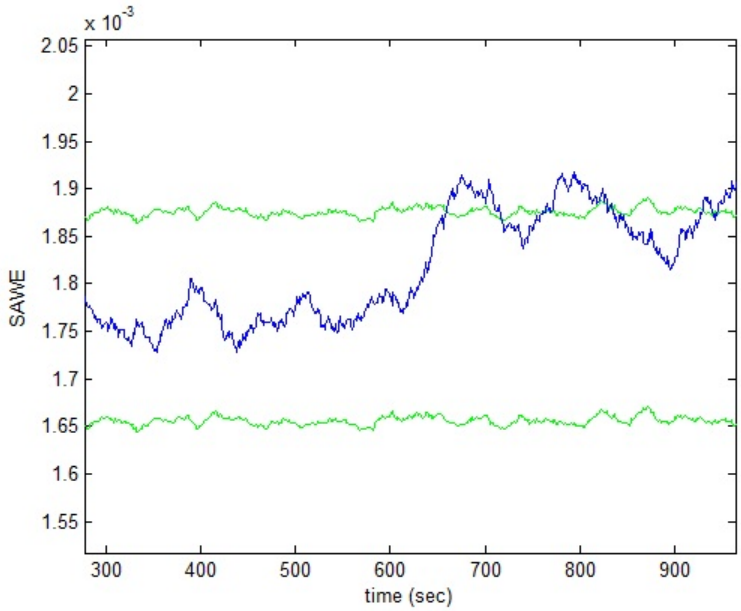

Figure 4.10: SAWE of the satellite for a 6% drop of the motor gain torque in the reaction wheel.

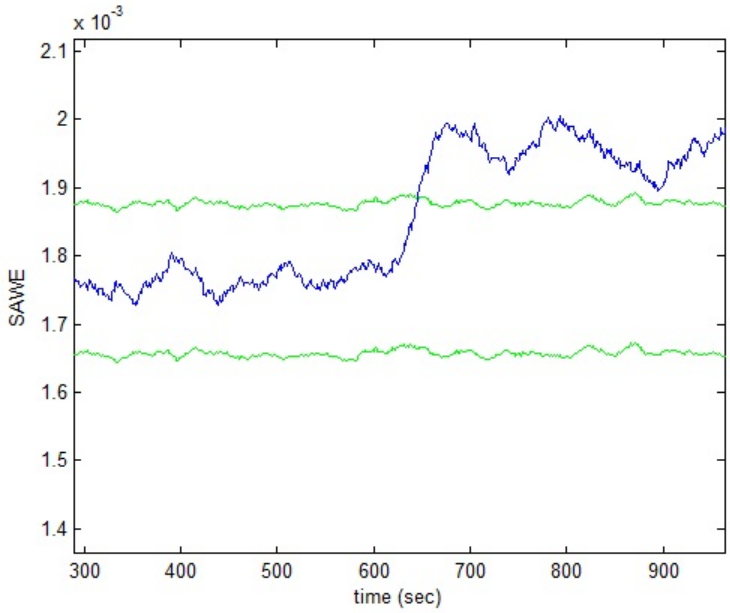

Figure 4.11: SAWE of the satellite for a 8% drop of the motor gain torque in the reaction wheel.

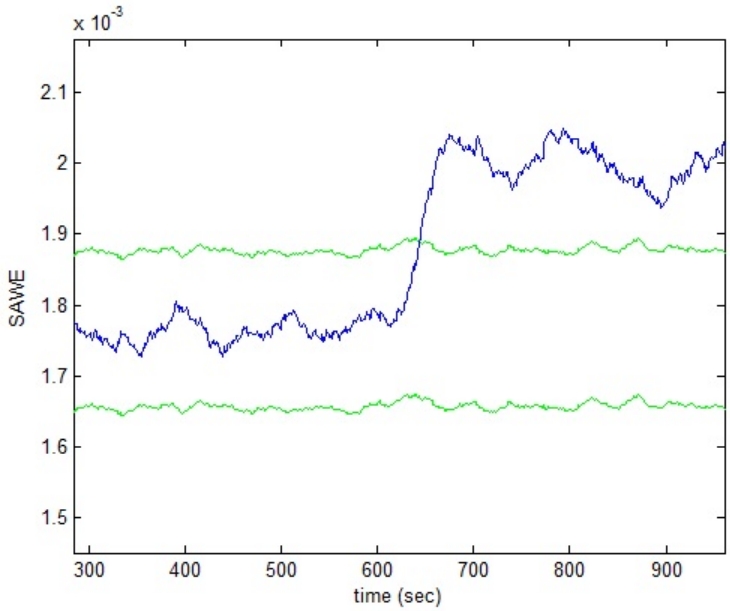

Figure 4.12: SAWE of the satellite for a 10% drop of the motor gain torque in the reaction wheel.

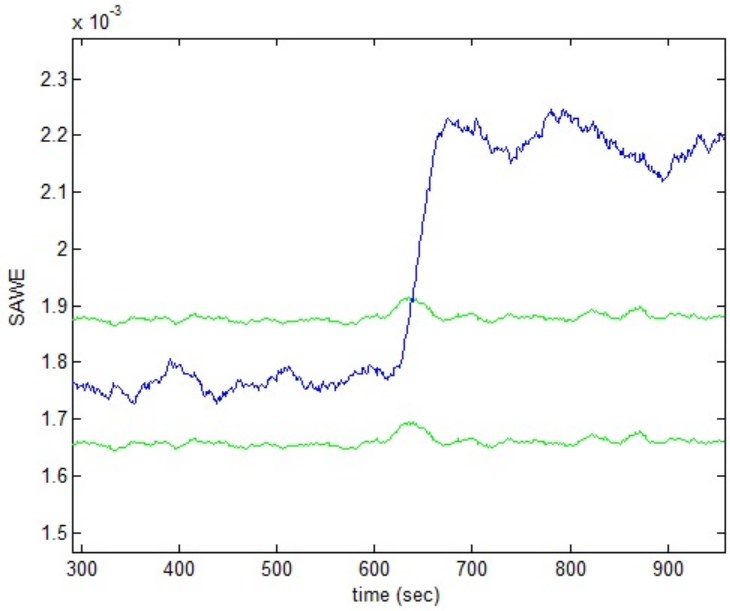

Figure 4.13: SAWE of the satellite for a 16% drop of the motor gain torque in the reaction wheel.

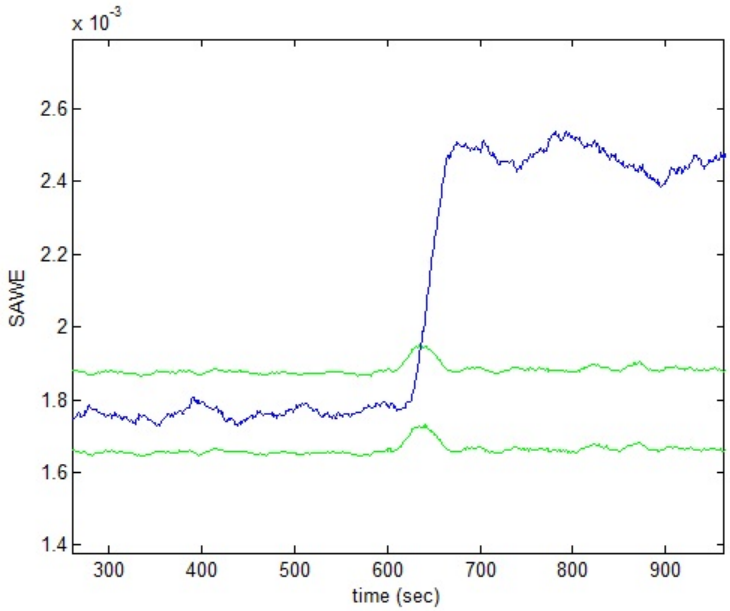

Figure 4.14: SAWE of the satellite for a 20% drop of the motor gain torque in the reaction wheel.

In the motor current fault scenario, the motor torque gain K_t of the reaction wheel is changed as an injected fault. In this fault scenario in order to simulate motor current fault, the motor torque constant K_t is dropped by 2%, 4%, 6%, 8%, 10%, 12%, 14%, 16%, 20%, 25%, 30% and 35% of its nominal value (nominal value of $K_t = 0.029$) at $t = 600sec$. The SAWEs of the satellite in this fault scenario are illustrated in Figures 4.9, 4.10, 4.11, 4.12, 4.13 and 4.14.

Table 4.4: Fault detection time in motor current fault scenario.

Percentage drop in motor gain torque	Fault injection time (second)	Fault detection time (second)
2	600	Not detected
4	600	Not detected
6	600	Not detected
8	600	656
10	600	653
12	600	651
14	600	648
16	600	647
20	600	646
25	600	646
30	600	645
35	600	645

The fault detection times are indicated in Table 4.4. The results indicate that this fault detection scheme can detect at least 8% drop in motor gain torque in the reaction wheel in a reasonable time period, however for lower drop in the motor gain torque, this scheme can not detect faults in the reaction wheel.

4.4.4 Reaction Wheel Operation under Viscous Temperature Fault Scenario

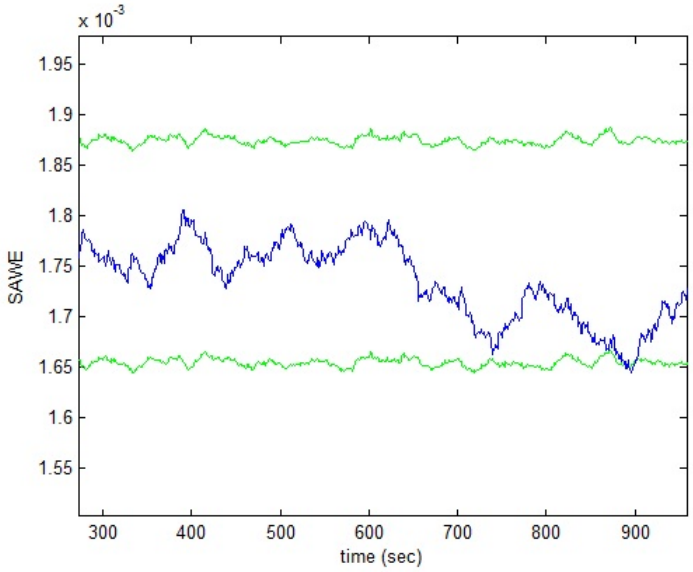

Figure 4.15: SAWE of the satellite for a 16% drop in the τ_v under viscous temperature fault scenario.

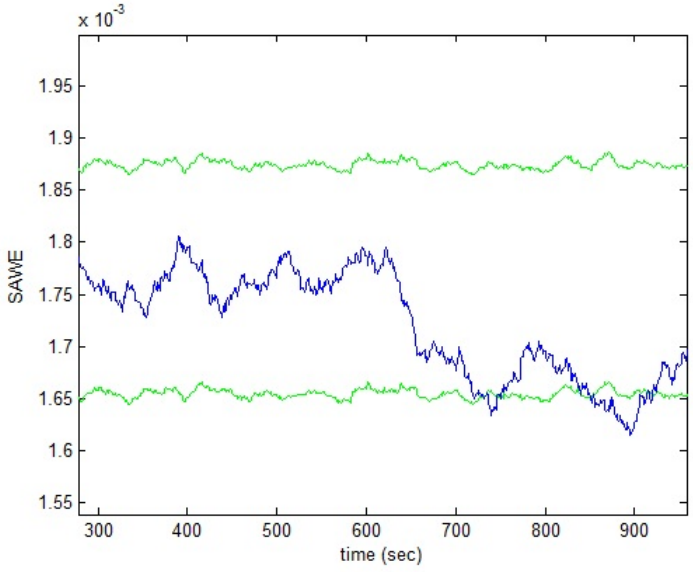

Figure 4.16: SAWE of the satellite for a 18% drop in the τ_v under viscous temperature fault scenario.

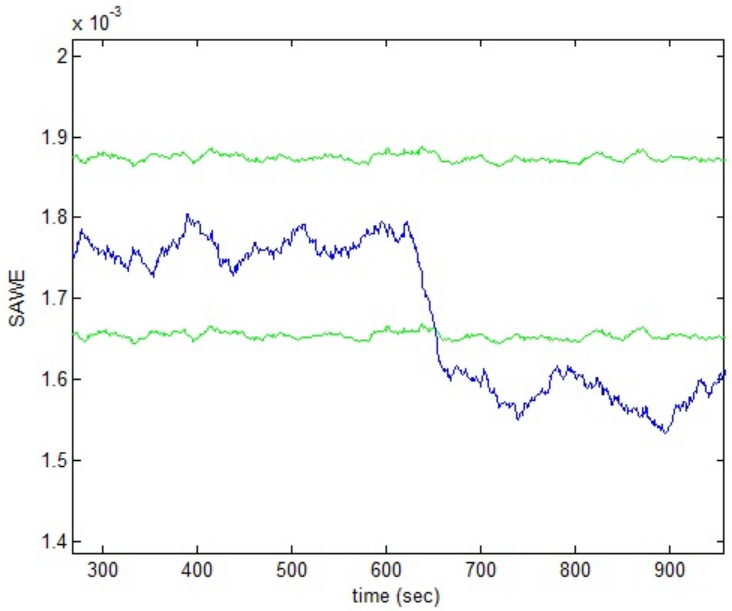

Figure 4.17: SAWE of the satellite for a 20% drop in the τ_v under viscous temperature fault scenario.

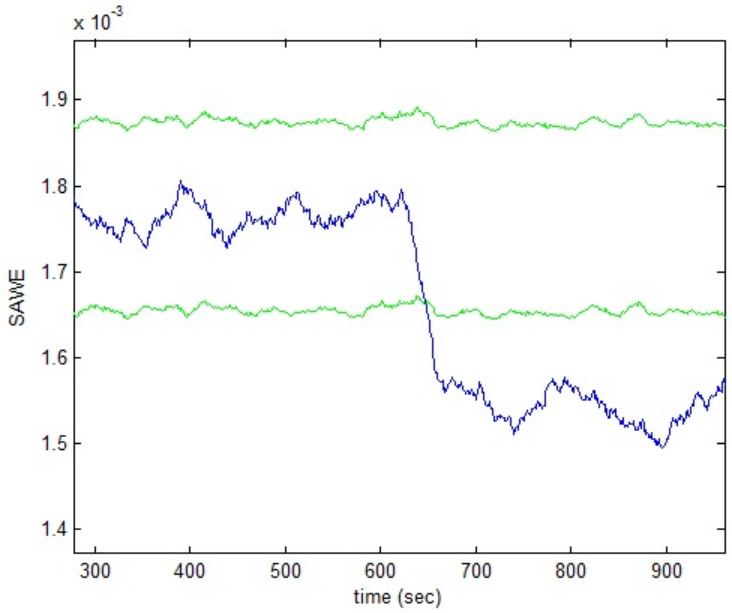

Figure 4.18: SAWE of the satellite for a 25% drop in the τ_v under viscous temperature fault scenario.

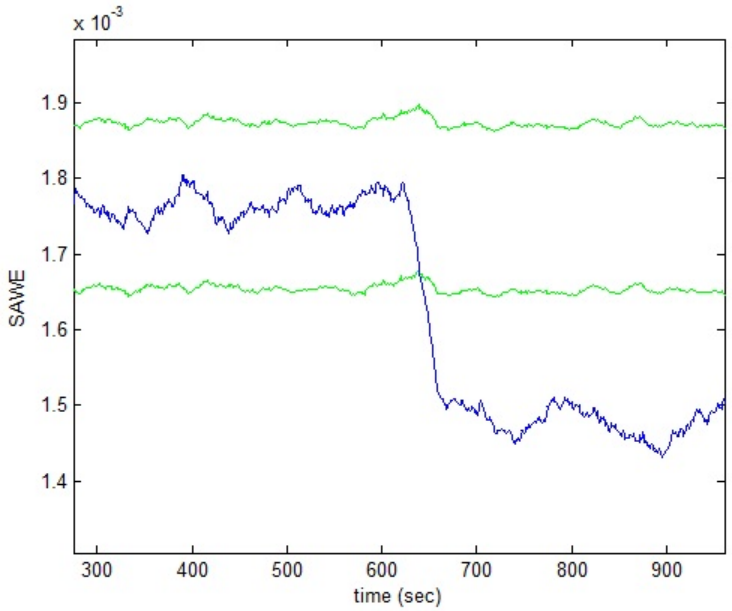

Figure 4.19: SAWE of the satellite for a 30% drop in the τ_v under viscous temperature fault scenario.

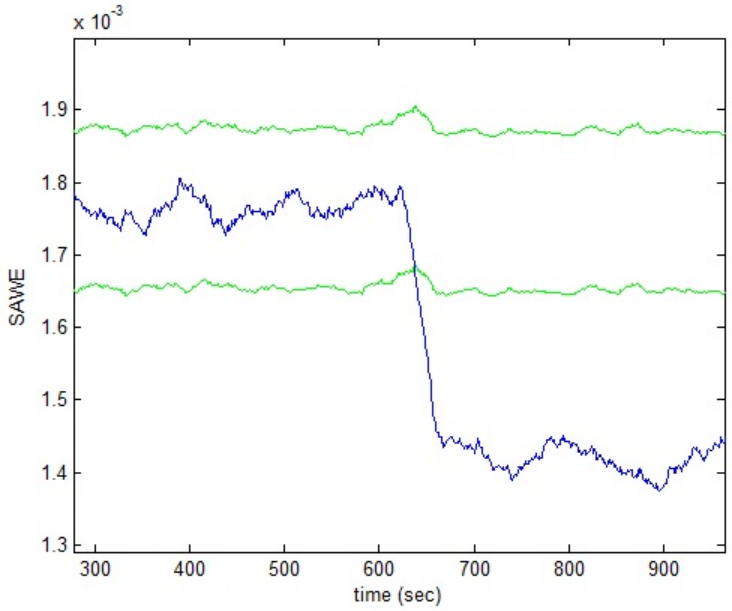

Figure 4.20: SAWE of the satellite for a 35% drop in the τ_v under viscous temperature fault scenario.

Due to the unknown working environment of the reaction wheel in a satellite in outer space the friction model is designed to work under a limited range of temperature. Since the bearing viscosity is temperature dependent, in the fiction model of the reaction wheel therefore any fluctuation in the temperature will be reflected as fluctuations in the drag torque. In the reaction wheel, according to equation (3.23) any change in τ_v is related to a change in the reaction wheel torque. Thus in this fault scenario the value of the viscous friction τ_v decrease 3%, 5%, 7%, 10%, 12%, 14%, 16%, 18%, 19%, 20%, 25%, 30%, 35% and 40% of its value under a normal condition. Figures 4.15, 4.16, 4.17, 4.18, 4.19 and 4.20 illustrate the SAWE in this fault condition for a satellite and the fault detection times are indicated in Table 4.5.

Table 4.5: Fault detection time in viscous temperature fault scenario.

Percentage drop in viscous friction τ_v	Fault injection time (second)	Fault detection time (second)
3	600	Not detected
5	600	Not detected
7	600	Not detected
10	600	Not detected
12	600	Not detected
14	600	Not detected
16	600	Not detected
18	600	Not detected
20	600	655
25	600	650
30	600	648
35	600	646
40	600	645

As the rsults in Table 4.5 show, the proposed algorithm is capable of detecting at least 20% drop in the viscous friction in a proper time period, however this scheme

can not detect lower drop in the viscous friction in the reaction wheel.

4.5 Window Size Effects on Fault Detection

As mentioned earlier, in our simulations the window size is selected as 350. Table 4.6 illustrate the fault detection time for different values of window in our simulations.

Table 4.6: Comparison of different window sizes in the fault detection performance.

Window size	Injected fault in $t = 600sec$	Fault detection time (second)
50	29% drop in bus voltage	Not detected
100	29% drop in bus voltage	Not detected
150	29% drop in bus voltage	667
200	29% drop in bus voltage	660
250	29% drop in bus voltage	652
300	29% drop in bus voltage	647
350	29% drop in bus voltage	647
400	29% drop in bus voltage	647
450	29% drop in bus voltage	647
50	8% drop in motor torque gain	Not Detected
100	8% drop in motor torque gain	Not Detected
150	8% drop in motor torque gain	Not Detected
200	8% drop in motor torque gain	679
250	8% drop in motor torque gain	668
300	8% drop in motor torque gain	663
350	8% drop in motor torque gain	656
400	8% drop in motor torque gain	656
450	8% drop in motor torque gain	656
50	20% drop in viscous friction	Not detected
100	20% drop in viscous friction	Not detected
150	20% drop in viscous friction	Not detected
200	20% drop in viscous friction	Not detected
250	20% drop in viscous friction	673
300	20% drop in viscous friction	664
350	20% drop in viscous friction	655
400	20% drop in viscous friction	655
450	20% drop in viscous friction	655

By considering the results in Table 4.6, the window size for fault diagnosis is selected as W=350.

4.6 Confusion Matrix Approach for Fault Detection

In order to evaluate the performance of the proposed fault detection algorithm, the confusion matrix [110] approach is used. A confusion matrix consists of four elements, namely the true positive, the true negative, the false positive, and the false negative which are defined as follows

- True positive (t.p.): The number of samples detected as healthy while the satellite is operating in the healthy mode.
- True negative (t.n.): The number of samples detected as faulty while the satellite is operating in the faulty mode.
- False negative (f.n.): The number of samples detected as healthy while the satellite is operating in the faulty mode.
- False positive (f.p.): The number of samples detected as faulty while the satellite is operating in the healthy mode.

For each fault scenario a confusion matrix is calculated and the two parameters of accuracy and precision are calculated to evaluate the performance of the fault detection scheme. These two parameters are defined as follows

$$Precision = \frac{t.n.}{t.n. + f.n.}$$

$$Accuracy = \frac{t.p. + t.n.}{t.p. + t.n. + f.p. + f.n.}$$

Table 4.7: Confusion matrix for the bus voltage fault scenario.

Percentage drop in bus voltage	t.n.	t.p.	f.n.	f.p.	Accuracy	Precision
25	N/A	N/A	N/A	N/A	N/A	N/A
26	N/A	N/A	N/A	N/A	N/A	N/A
27	N/A	N/A	N/A	N/A	N/A	N/A
28	28	50	16	0	78%	56%
29	42	50	8	0	92%	84%
30	44	50	6	0	94%	88%
31	45	50	5	0	95 %	90%
32	47	50	3	0	97 %	94%
33	49	50	1	0	99 %	98%
34	50	50	0	0	100 %	100%
35	50	50	0	0	100 %	100%
36	50	50	0	0	100 %	100%
37	50	50	0	0	100 %	100%
38	50	50	0	0	100 %	100%
39	50	50	0	0	100 %	100%
40	50	50	0	0	100 %	100%

For a total number of 100 simulations for each fault scenario the confusion matrices are produced. The confusion matrix for bus voltage fault scenario is illustrated in Table 4.7. As the results show the proposed method is capable of detecting 29% drop in the bus voltage with 78% accuracy and 56% precision, but it cannot detect lower drops in the bus voltage in the reaction wheel.

Table 4.8: Confusion matrix for motor current fault scenario.

Percentage drop in motor torque gain K_t	t.n.	t.p.	f.n.	f.p.	Accuracy	Precision
2	N/A	N/A	N/A	N/A	N/A	N/A
4	N/A	N/A	N/A	N/A	N/A	N/A
6	N/A	N/A	N/A	N/A	N/A	N/A
8	30	50	20	0	80%	60%
10	34	50	16	0	84%	68%
12	37	50	13	0	87%	74%
14	39	50	11	0	89%	78%
16	43	50	7	0	93 %	86%
20	46	50	4	0	96 %	92%
25	48	50	2	0	98 %	96%
30	50	50	0	0	100 %	100%
35	50	50	0	0	100 %	100%

Table 4.9: Confusion matrix for viscous temperature fault scenario.

Percentage drop in viscous friction τ_v	t.n.	t.p.	f.n.	f.p.	Accuracy	Precision
3	N/A	N/A	N/A	N/A	N/A	N/A
5	N/A	N/A	N/A	N/A	N/A	N/A
7	N/A	N/A	N/A	N/A	N/A	N/A
10	N/A	N/A	N/A	N/A	N/A	N/A
12	N/A	N/A	N/A	N/A	N/A	N/A
14	N/A	N/A	N/A	N/A	N/A	N/A
16	N/A	N/A	N/A	N/A	N/A	N/A
18	N/A	N/A	N/A	N/A	N/A	N/A
20	31	50	19	0	81%	62%
25	35	50	15	0	85%	70%
30	41	50	9	0	91%	82%
35	46	50	4	0	96%	92%
40	49	50	1	0	99%	98%

Tables 4.8 and 4.9 indicate the confusion matrix values for the second and third fault scenario, respectively. As the results in Table 4.8 show, the value of the precision in the motor current fault scenario for 8% drop in the motor torque gain is not suitable for fault detection purposes and also the proposed fault detection method cannot detect motor current faults lower than 8% drop in K_t. In the third fault scenario, as indicated in Table 4.9, the values of the precision for 20% drop in the viscous friction are not satisfying the fault detection purpose and this fault detection method cannot detect low severity faults in the viscous temperature fault scenario.

4.7 Spacecraft-level Fault Isolation

When a fault is detected in a satellite, the next step is to isolate the fault. The goal of the fault isolation is to determine the faulty reaction wheel in a satellite, i.e. determine which reaction wheel in a x-axis, y-axis or z-axis of a satellite has a fault. In order to isolate the fault in a satellite, the absolute angular velocity measurements of a satellite are chosen as diagnostic signals in our fault isolation scheme. Therefore, for fault isolation the diagnostic signals are $\omega_x, \omega_y, \omega_z$ in a satellite.

Our proposed fault isolation scheme utilizes the relative wavelet energy (RWE) technique as diagnostic signals. In order to determine the RWEs, first the diagnostic signals are decomposed by using discrete wavelet transform and details and approximation coefficients are produced. In the next step, according to equation (4.16) the RWEs of these coefficients are calculated. For L level of decomposition in each diagnostic signal, one has L relative wavelet energy with respect to detail coefficients and one relative wavelet energy with respect to approximation coefficient. In our proposed scheme, the level of decomposition for fault isolation is chosen as 1. For higher levels of decomposition, the computation becomes more complex and it is required more storage, hence L=1 is a proper level of decompostion for the proposed fault islation scheme.

Table 4.10 illustrate the average of the RWEs of the angular velocity measurements in three axe of a satellite under different fault scenarios. As this table shows, if the fault occurs in one axis, the RWE of the approximation coefficients are increased in that axis and the RWE of the other approximation coefficients do not change. Hence, by considering the RWE of the approximation coefficients one can isolate the fault in a satellite. Since the bus voltage is common in three reaction wheels, therefore the RWEs of the approximation coefficients of the three axes are changed.

Table 4.10: Average of the RWEs of the angular velocity measurements in a satellite.

Fault scenario	ω_x	ω_y	ω_z
Bus voltage	[0.9921 0.0079]	[0.9922 0.0078]	[0.9920 0.008]
Motor current in x-axis	[0.9391 0.0609]	[0.5233 0.4768]	[0.5233 0.4768]
Viscous temperature in x-axis	[0.9792 0.0208]	[0.5233 0.4768]	[0.5233 0.4768]
Motor current in y-axis	[0.5233 0.4768]	[0.9443 0.0557]	[0.5233 0.4768]
Viscous temperature in y-axis	[0.5233 0.4768]	[0.9797 0.203]	[0.5233 0.4768]
Motor current in z-axis	[0.5233 0.4768]	[0.5233 0.4768]	[0.9434 0.0566]
Viscous temperature in z-axis	[0.5233 0.4768]	[0.5233 0.4768]	[0.9794 0.0206]

As the results in Table 4.10 indicate, we can isolate the fault in a satellite by considering the change of the RWEs of the approximation coefficients. In order to isolate the fault, we define the threshold for the RWEs of each diagnostic signal. If the RWE of the ω_x passes its threshold the fault has occurred in x-axis of a satellite, if the RWE of the ω_y passes its threshold the fault has occurred in y-axis and similarly if the RWE of the ω_z passes its threshold the fault has occurred in z-axis of a satellite. If all RWEs of all three $\omega_x, \omega_y, \omega_z$ pass their thresholds the bus voltage fault condition is determined in the three axes of a satellite.

In order to define the threshold for each angular velocity measurements, the RWEs in healthy condition are considered and according to thresholds scheme in Figure 4.1 the parameter δ is defined, and then the threshold is calculated online. Table 4.11 indicates the values of the RWEs in healthy condition for each angular velocity measurements in a satellite.

The value of δ for fault isolation scheme is selected as $\delta = 0.32$ and the parameters T_1 and T_2 are selected as $T_1 = 5,\ T_2 = 0.4$. The RWE of the approximation coefficients in three axes of a satellite and the thresholds, under three fault scenarios are illustrated in Figures 4.21, 4.22, 4.23, 4.24, 4.25, 4.26 and 4.27. As seen in these figures, the fault can be isolated by considering the RWEs of the approximation coefficients of the diagnostic signals.

Table 4.11: The average of the RWEs of the approximation coefficient of the angular velocity measurements in a satellite.

Desired missions	ω_x	ω_y	ω_z	Desired missions	ω_x	ω_y	ω_z
$[24, 209, 168]$	0.2935	0.2393	0.2463	$[13, 83, 41]$	0.2578	0.2180	0.2586
$[89, 25, 17]$	0.2761	0.2792	0.2537	$[41, 60, 18]$	0.2734	0.3009	0.2158
$[160, 110, 31]$	0.2711	0.2516	0.2529	$[67, 87, 69]$	0.2496	0.2281	0.2614
$[43, 13, 80]$	0.2880	0.2101	0.2761	$[15, 25, 50]$	0.2875	0.3112	0.2411
$[355, 126, 200]$	0.3054	0.2406	0.1898	$[90, 90, 90]$	0.2657	0.2364	0.2709
$[340, 130, 300]$	0.2449	0.2558	0.2441	$[39, 103, 331]$	0.2736	0.3074	0.2511
$[297, 303, 290]$	0.2615	0.2182	0.1864	$[12, 25, 46]$	0.2075	0.2456	0.2660
$[30, 310, 45]$	0.2806	0.2629	0.3051	$[62, 11, 83]$	0.2759	0.2339	0.2228
$[97, 257, 35]$	0.2234	0.2450	0.2439	$[43, 80, 34]$	0.3216	0.2681	0.2233
$[124, 44, 19]$	0.2330	0.2963	0.3029	$[108, 130, 207]$	0.2593	0.2483	0.2495
$[341, 166, 350]$	0.2216	0.2488	0.2440	$[30, 30, 30]$	0.2223	0.2558	0.2448
$[90, 0, 0]$	0.3184	0.2520	0.2301	$[33, 89, 165]$	0.2801	0.2327	0.2608
$[15, 40, 76]$	0.2303	0.2512	0.2183	$[10, 25, 90]$	0.2483	0.2759	0.2426
$[173, 137, 86]$	0.2709	0.2554	0.2396	$[114, 227, 120]$	0.2808	0.2660	0.2407
$[72, 64, 56]$	0.2287	0.2727	0.2350	$[22, 145, 35]$	0.2153	0.2910	0.2659
$[45, 45, 45]$	0.2344	0.2926	0.2669	$[50, 29, 13]$	0.2430	0.2866	0.2389
$[84, 279, 159]$	0.2998	0.2360	0.2556	$[0, 0, 90]$	0.2521	0.2329	0.2511
$[20, 333, 31]$	0.2136	0.2852	0.2428	$[82, 3, 23]$	0.2793	0.2514	0.2337
$[85, 66, 164]$	0.2903	0.2331	0.2610	$[180, 100, 57]$	0.2626	0.2602	0.2581
$[0, 90, 0]$	0.3021	0.2842	0.2268	$[30, 45, 60]$	0.2891	0.2722	0.2426

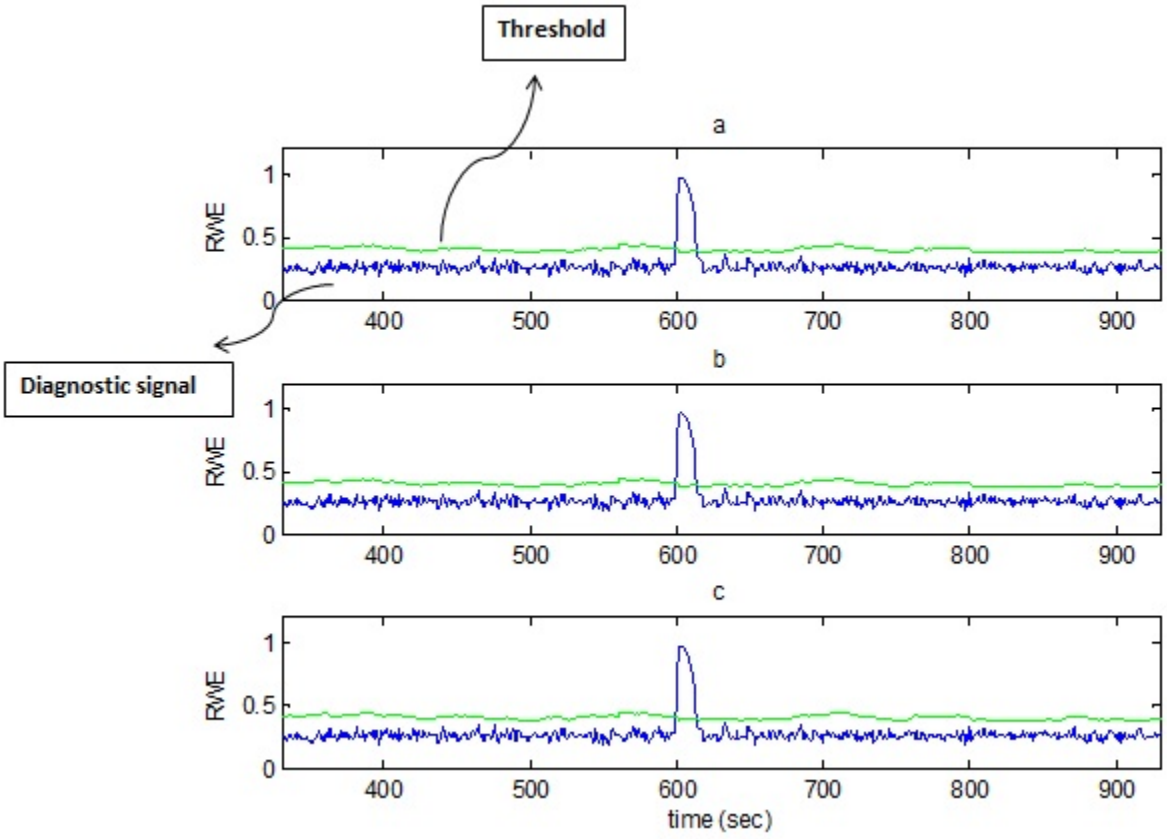

Figure 4.21: The RWEs of the approximation coefficients for three angular velocity measurement in a satellite under the bus voltage fault scenario. $a = \omega_x$, $b = \omega_y$ and $c = \omega_z$.

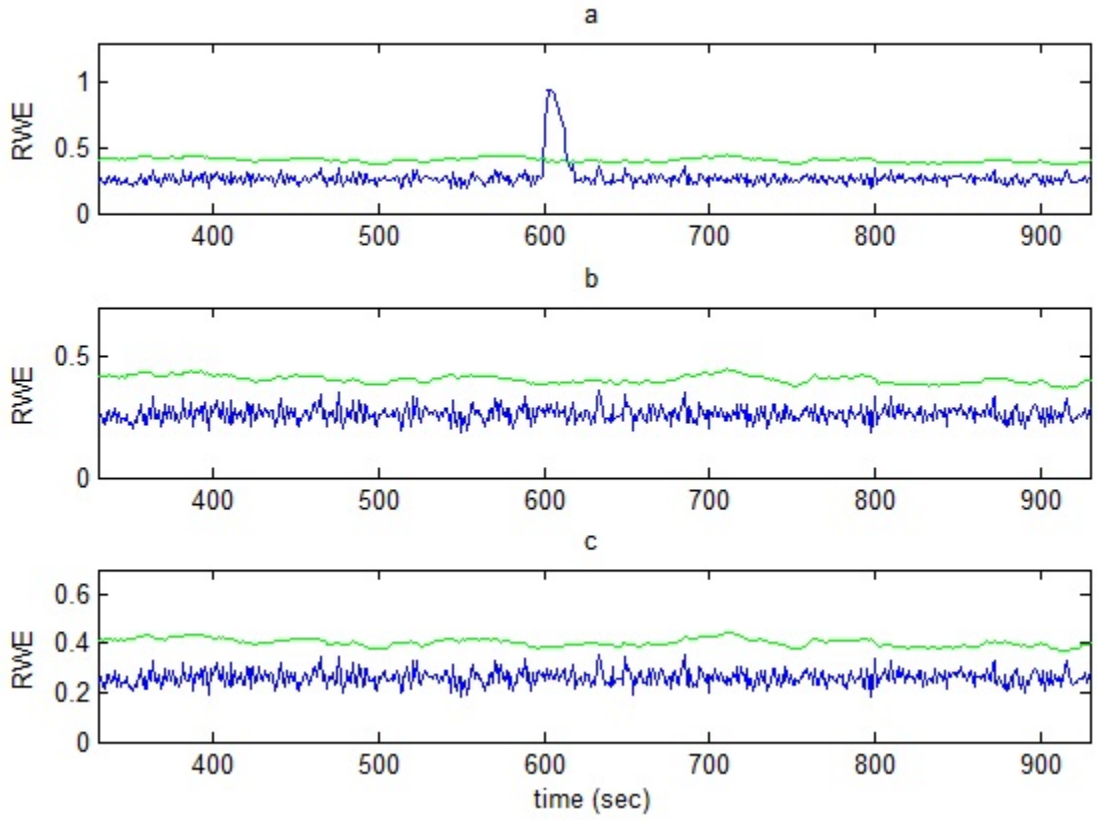

Figure 4.22: The RWEs of the approximation coefficients for three angular velocity measurements in a satellite under the motor current fault scenario in the x-axis. $a = \omega_x$, $b = \omega_y$ and $c = \omega_z$.

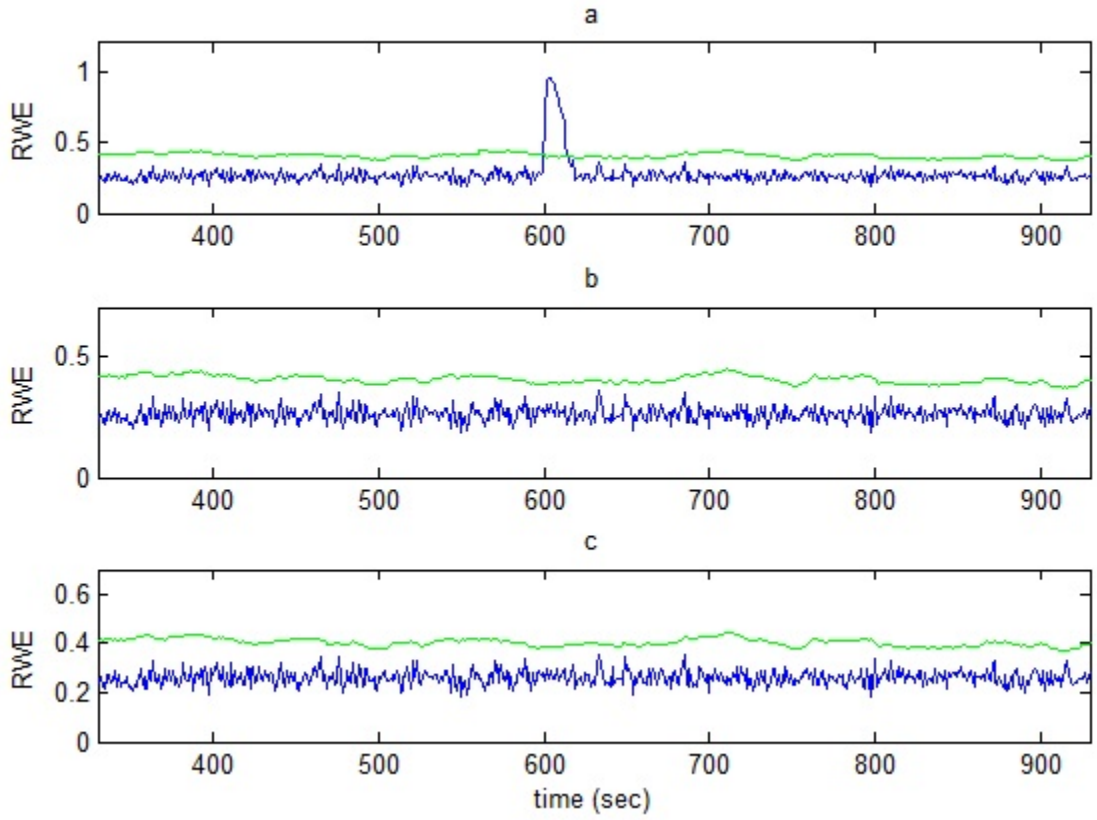

Figure 4.23: The RWEs of the approximation coefficients for three angular velocity measurements in a satellite under the viscous temperature fault scenario in the x-axis. $a = \omega_x$, $b = \omega_y$ and $c = \omega_z$.

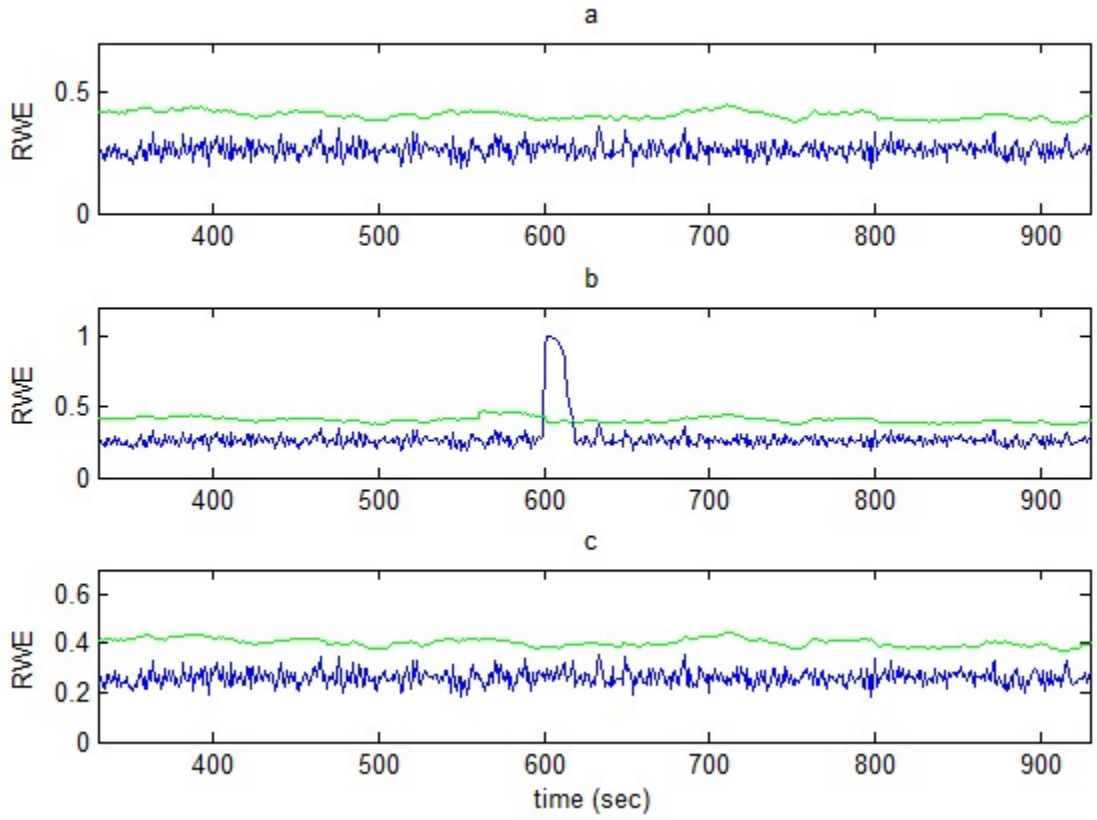

Figure 4.24: The RWEs of the approximation coefficients for three angular velocity measurements in a satellite under the motor current fault scenario in the y-axis. $a = \omega_x$, $b = \omega_y$ and $c = \omega_z$.

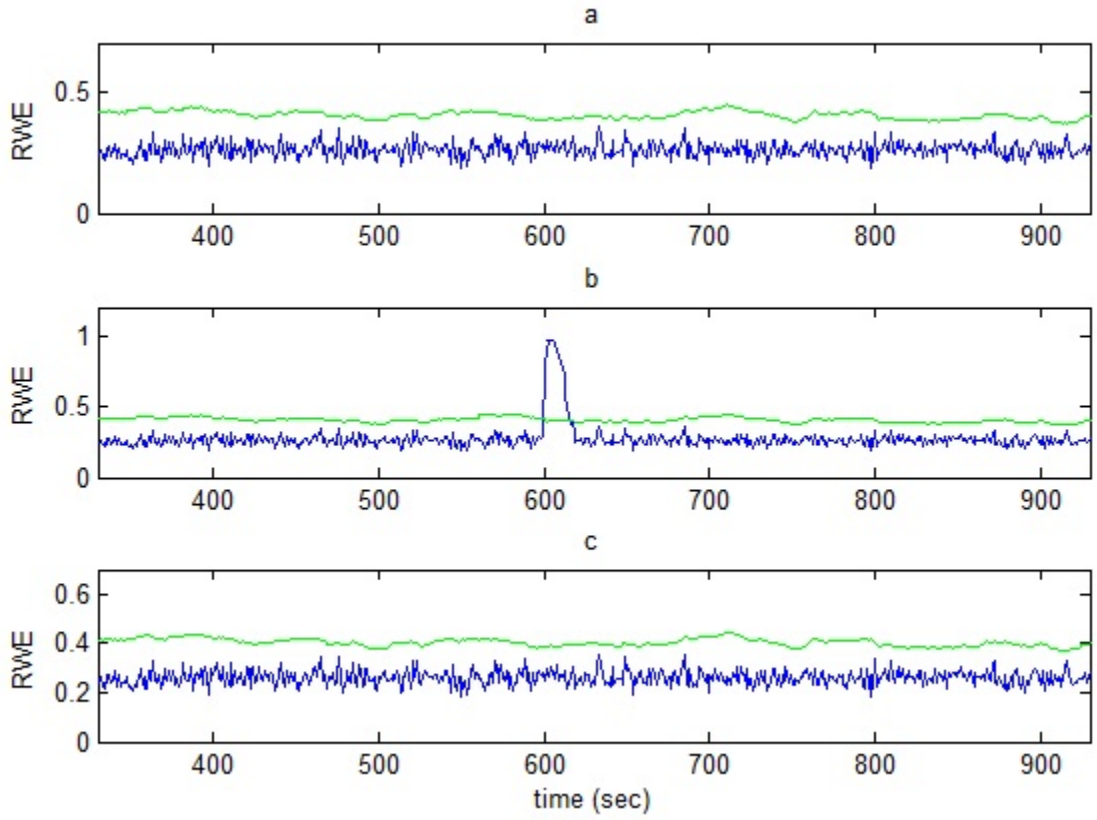

Figure 4.25: The RWEs of the approximation coefficients for three angular velocity measurements in a satellite under the viscous temperature fault scenario in the y-axis. $a = \omega_x$, $b = \omega_y$ and $c = \omega_z$.

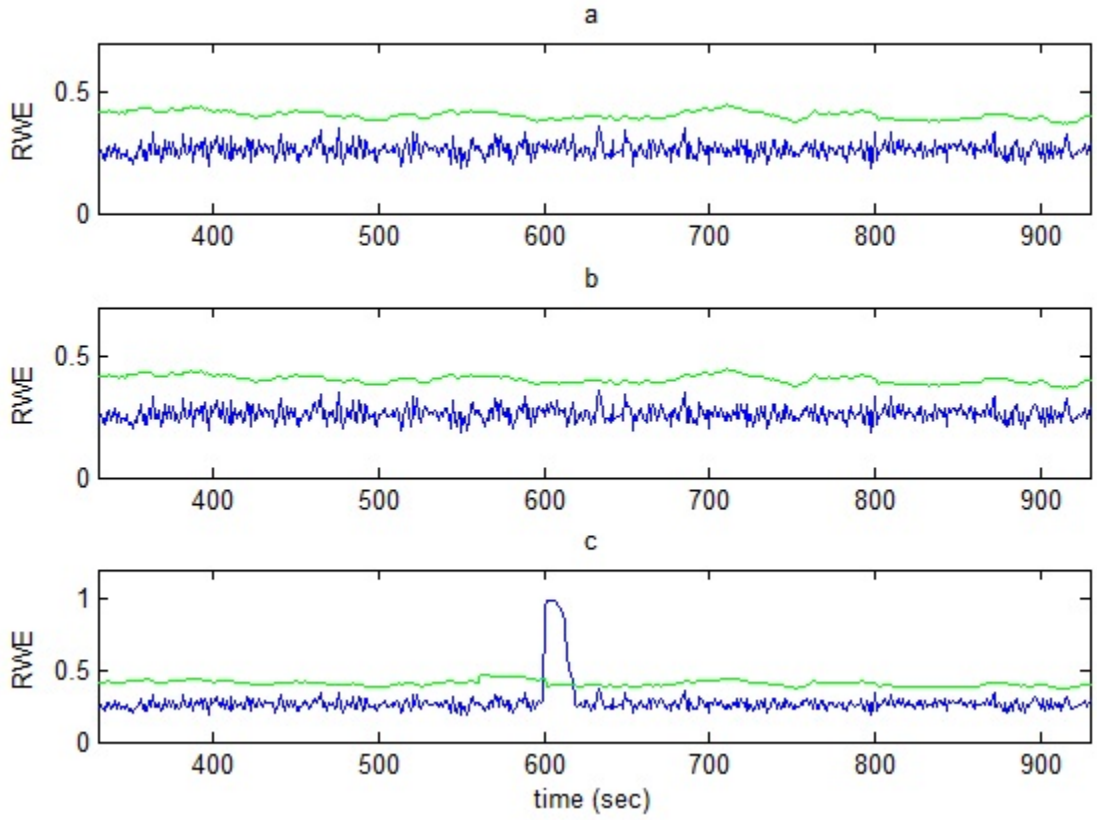

Figure 4.26: The RWEs of the approximation coefficients for three angular velocity measurements in a satellite under the motor current fault scenario in the z-axis. $a = \omega_x$, $b = \omega_y$ and $c = \omega_z$.

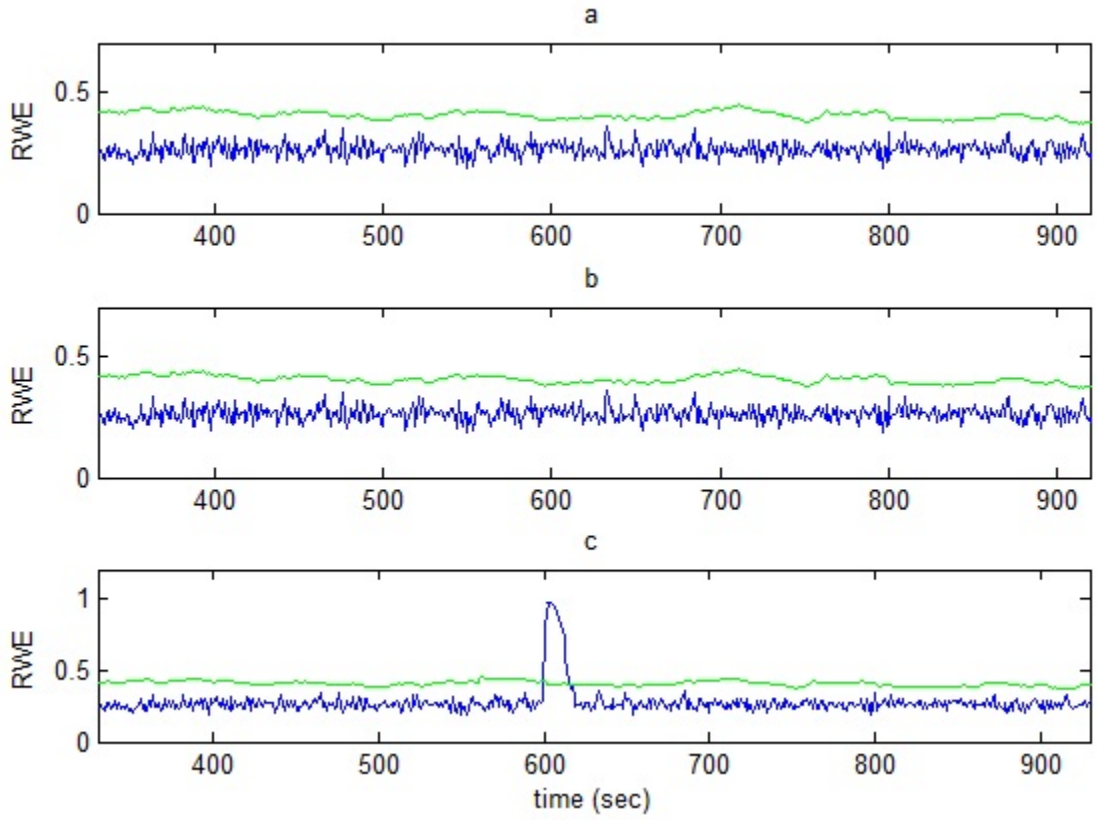

Figure 4.27: The RWEs of the approximation coefficients for three angular velocity measurements in a satellite under the viscous temperature fault scenario in the z-axis. $a = \omega_x$, $b = \omega_y$ and $c = \omega_z$.

In order to evaluate the performance of the proposed fault isolation scheme, the confusion matrix criteria is used. In the fault isolation, there are three classes for three axes of a satellite, hence the confusion matrix for fault isolation is a 3×3 matrix. The confusion matrices for the fault isolation is defined as follows

$$Confusion\ Matrix\ (CM) = \begin{pmatrix} cm_{11} & cm_{12} & cm_{13} \\ cm_{21} & cm_{22} & cm_{23} \\ cm_{31} & cm_{32} & cm_{33} \end{pmatrix} \tag{4.19}$$

where

- cm_{11}= Number of data in the x-axis that is correctly classified as the x-axis.

- cm_{12}=Number of data in the y-axis that is incorrectly classified as the x-axis.
- cm_{13}=Number of data in the z-axis that is incorrectly classified as the x-axis.
- cm_{21}=Number of data in the x-axis that is incorrectly classified as the y-axis.
- cm_{22}=Number of data in the y-axis that is correctly classified as the y-axis.
- cm_{23}=Number of data in the z-axis that is incorrectly classified as the y-axis.
- cm_{31}=Number of data in the x-axis that is incorrectly classified as the z-axis.
- cm_{32}=Number of data in the y-axis that is incorrectly classified as the z-axis.
- cm_{33}=Number of data in the z-axis that is correctly classified as the z-axis.

The confusion matrix for fault isolation is illustrated in Table 4.12.

Table 4.12: Confusion matrix for the fault isolation.

Fault scenario	cm_{11}	cm_{12}	cm_{13}	cm_{21}	cm_{22}	cm_{23}	cm_{31}	cm_{32}	cm_{33}
Bus voltage	10	0	0	0	10	0	0	0	10
Motor current	10	0	0	0	10	0	0	0	10
Viscous temperature	10	0	0	0	10	0	0	0	10

The parameters accuracy for fault isolation is defined as follows

$$Accuracy = \frac{cm_{11} + cm_{22} + cm_{33}}{\sum_{j=1}^{3}\sum_{i=1}^{3} c_{ij}}$$

As the results in Table 4.12 show, the proposed fault isolation scheme can isolate the faults in a satellite with a 100% classification accuracy.

4.8 Spacecraft-level Fault Identification

The next step after fault isolation is the fault identification. In this step the type of the fault in a reaction wheel is determined, i.e. in this step it is determined that the

fault belongs to which categories of faults (bus voltage, motor current and viscous temperature).

Fault identification is also known as pattern classification problem. In the pattern classification problem, the first and most important stage is feature extraction. In our proposed fault identification scheme, the feature extraction is accomplished by discrete wavelet transform and these features are classified by a multilayer perceptron neural network (MLPNN). In this scheme, the absolute attitude measurements in a satellite (q_1, q_2, q_3) are considered as diagnostic signals and the detail and approximation coefficients of the diagnostic signals are extracted as features in order to identify the fault. Figure 4.28 illustrate the proposed scheme for fault identification in a satellite. As this figure shows, two major tasks must be done in order to identify the fault; feature extraction and pattern classification.

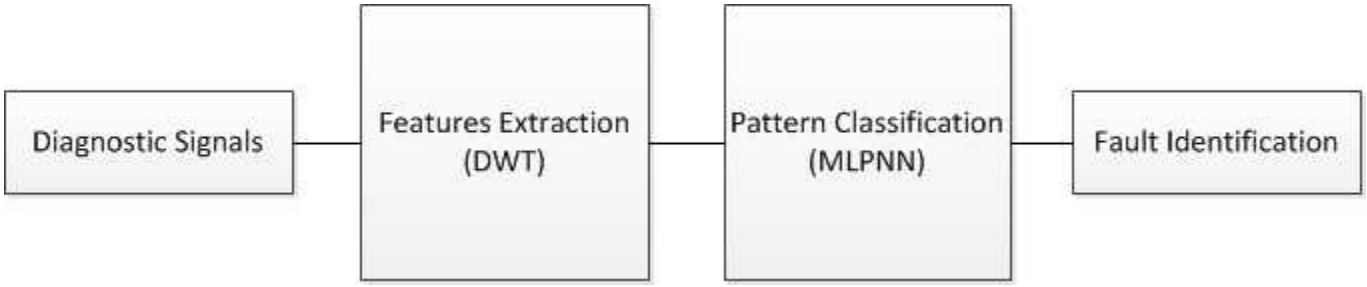

Figure 4.28: Proposed scheme for fault identification in a satellite.

4.8.1 Feature Extraction

The feature extraction in our proposed fault identification scheme is performed by utilizing the detail and approximation coefficients of the diagnostic signals. For L level of decomposition in each diagnostic signal, one has L detail coefficients and one approximation coefficient. These $L + 1$ coefficients signals are used for pattern classification purposes.

In the proposed fault identification scheme, the level of decomposition is chosen as L=3. The entropy of the attitude measurements in different levels of decomposition are demonstrated in Figure 4.29 and the values of the entropies are indicated in Table 4.13. As the entropies indicate, when we increase the level of decomposition from 3

to 4 and higher the value of the entropy for D_1 are about 10 times bigger than the entropy of the D_4, D_5 and D_6. Hence, by increasing the level of decomposition from 3 to higher values the detail coefficients do not contain any useful information about the signal. Therefore, the level of decomposition is selected as L=3. With 3 levels of decomposition, there are one approximation and three detail coefficients that are used for pattern classification in the next step.

Table 4.13: The value of the entropy of the attitude measurements for different levels of decomposition.

Detail Coefficient	L=1	L=2	L=3	L=4	L=5	L=6
D_1	5.3234 e-5	5.3234 e-5	5.3234 e-5	5.3234 e-5	5.3234 e-5	5.3234 e-5
D_2	N/A	1.9323 e-5	1.9323 e-5	1.9323 e-5	1.9323 e-5	1.9323 e-5
D_3	N/A	N/A	1.5501 e-5	1.5501 e-5	1.5501 e-5	1.5501 e-5
D_4	N/A	N/A	N/A	5.5564 e-6	5.5564 e-6	5.5564 e-6
D_5	N/A	N/A	N/A	N/A	3.1473 e-6	3.1473 e-6
D_6	N/A	N/A	N/A	N/A	N/A	2.5748 e-6

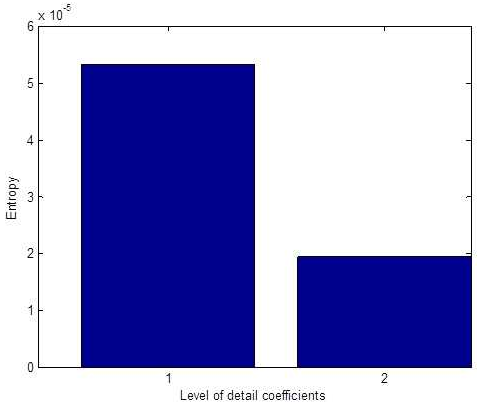

(a) $L = 2$

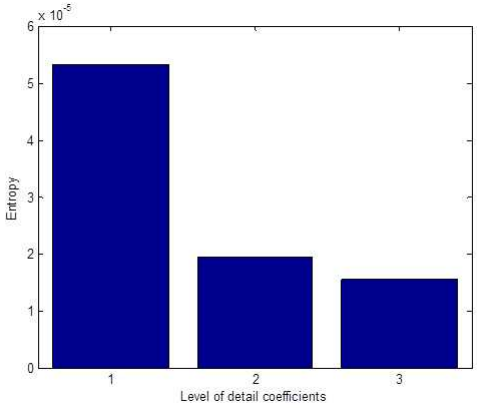

(b) $L = 3$

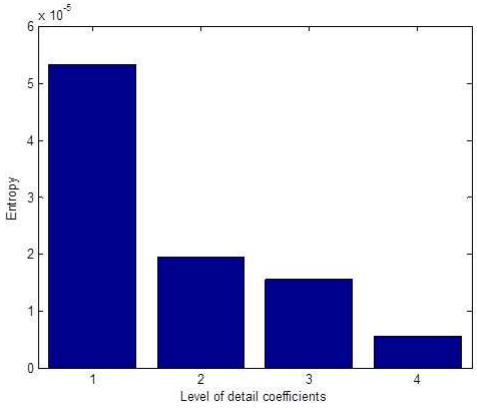

(c) $L = 4$

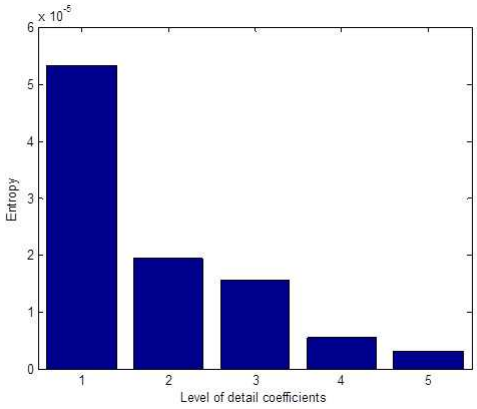

(d) $L = 5$

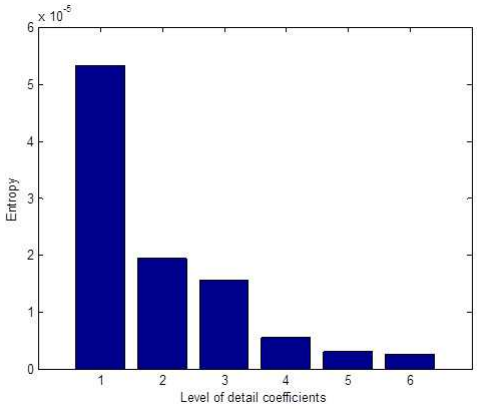

(e) $L = 6$

Figure 4.29: The entropy of the detail coefficients of the attitude measurements for different levels of decomposition.

4.8.2 Pattern Classification

The pattern classification in our proposed fault identification scheme is performed by utilizing the multilayer perceptron neural network (MLPNN). The ability of neural networks in pattern classification makes it as a powerful method for fault identification purposes.

Neural Networks as a Pattern Classifier

In the classification problem an object needs to be assigned into a predefined class based on a number of observed attributes related to that object. Neural networks have emerged as an important tool for pattern classification. The recent vast research activities in neural network classification have established that neural networks are a promising alternative to various conventional classification methods. The advantages of neural networks in the classification problem are described as follows:

- Neural networks are data driven self-adaptive methods and they can adjust themselves to the data without any explicit specification of the functional or distributional form for the underlying model, and
- Neural networks are nonlinear models, which make them flexible in modeling real world complex relationships.

4.8.3 Proposed Scheme for Fault Identification

For fault identification, as mentioned before, the detail and approximation coefficients of the DWT of the attitude measurements in a satellite are considered as inputs for MLPNN. With L=3 levels of decomposition, there are 3 detail coefficients and 1 approximation coefficient for each diagnostic signal, hence there are 12 coefficients with respect to q_1, q_2, q_3 in a satellite. The output of the MLPNN are three fault scenarios in the reaction wheel. Hence, the MLPNN in fault identification scheme has 3 neurons as outputs. The proposed MLPNN for the fault identification has 12 inputs, 12 neurons in the hidden layer and 3 neurons as outputs. The three fault

Table 4.14: Assigned classes for fault scenarios of the MLPNN.

Fault Scenario	Assigned Class
Bus Voltage	0 0 1
Motor Current	0 1 0
Viscous Temperature	1 0 0

scenarios in the reaction wheels that are assigned for three classes in outputs of the MLPNN are shown in Table 4.14.

The learning algorithm that is used in the MLPNN is back-propagation algorithm and the learning rate for the MLPNN is chosen to be 0.005 and the activation functions for hidden layers are selected as hyperbolic tangent and for the output layer is selected as linear functions.

The data sets that are used for training, validating and testing the MLPNN are obtained from detail and approximation coefficients of the diagnostic signals and these data are normalized and fed into the neural networks for training step. Figure 4.30 illustrate the training performance of the network in terms of the root mean square error (mse).

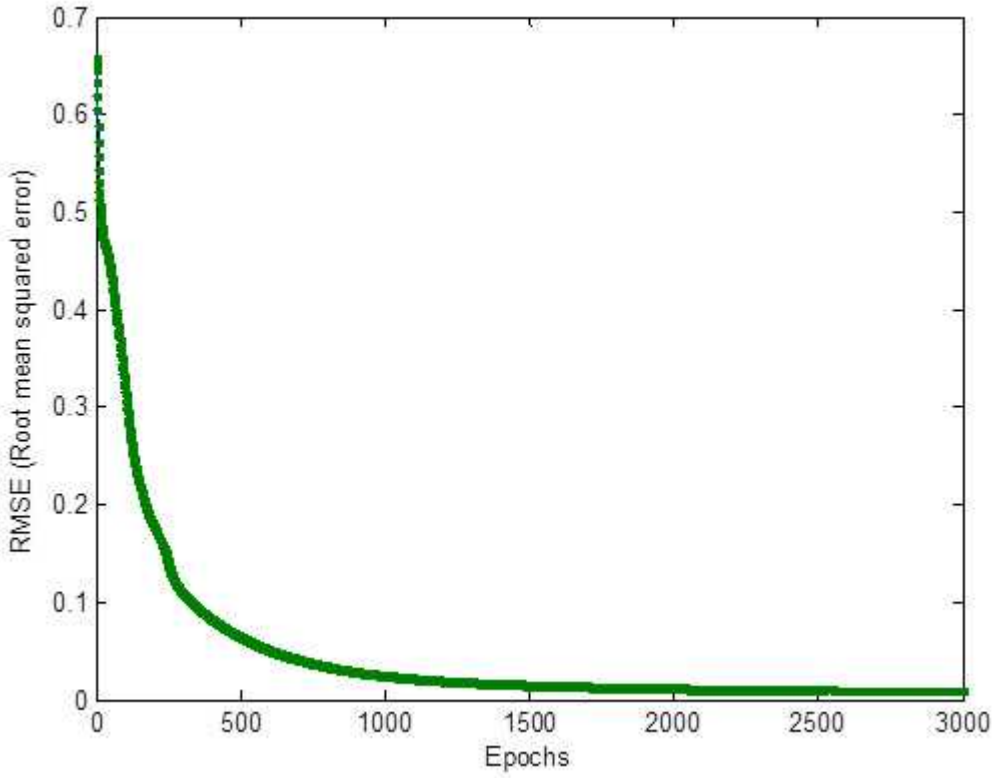

Figure 4.30: Performance of proposed MLPNN learning for fault identification.

After the training step, the network is validated and tested with new data sets to ensure the consistency in the performance of the network. Table 4.15 shows the outputs of the MLPNN for the three fault scenarios in a faulty reaction wheel. In order to evaluate the performance of the MLPNN for fault isolation, the confusion matrix criterion is used.

Table 4.15: Outputs of the MLPNN for fault identification.

Actual output	Network output
0 0 1	0.0189 0.0753 0.9058
0 1 0	0.9901 -0.0098 0.0197
1 0 0	0.9901 -0.0099 0.0197
0 0 1	0.0197 -0.0097 0.99
0 1 0	0.0093 0.9814 0.0093
0 1 0	0.9603 0.0202 0.0194
0 0 1	0.0197 -0.0097 0.99

In the fault identification problem, there are three classes for three types of faults, hence the confusion matrix for the fault identification is a 3×3 matrix. Similar to the fault isolation case, the confusion matrix for the fault identification is defined as follows

$$Confusion\ Matrix\ (CM) = \begin{pmatrix} cm_{11} & cm_{12} & cm_{13} \\ cm_{21} & cm_{22} & cm_{23} \\ cm_{31} & cm_{32} & cm_{33} \end{pmatrix} \tag{4.20}$$

where

- cm_{11}=Number of data in the class 1 that is correctly classified as the class 1.
- cm_{12}=Number of data in the class 2 that is incorrectly classified as the class 1.
- cm_{13}=Number of data in the class 3 that is incorrectly classified as the class 1.
- cm_{21}=Number of data in the class 1 that is incorrectly classified as the class 2.
- cm_{22}=Number of data in the class 2 that is correctly classified as the class 2.
- cm_{23}=Number of data in the class 3 that is incorrectly classified as the class 2.
- cm_{31}=Number of data in the class 1 that is incorrectly classified as the class 3.

- cm_{32}=Number of data in the class 2 that is incorrectly classified as the class 3.
- cm_{33}=Number of data in the class 3 that is correctly classified as the class 3.

where for the fault identification problem, class 1 refers to the bus voltage fault, class 2 refers to the motor current fault and the class 3 refers to the viscous temperature fault.

Furthermore, the classification accuracy can be define as follows

$$Classification\ Accuracy = \frac{Number\ of\ data\ that\ are\ correctly\ classified}{Total\ number\ of\ data} \quad (4.21)$$

The confusion matrix for the fault identification and the classification accuracy are illustrated in Table 4.16.

Table 4.16: Confusion matrix for the fault identification.

cm_{11}	cm_{12}	cm_{13}	cm_{21}	cm_{22}	cm_{23}	cm_{31}	cm_{32}	cm_{33}	Classification Accuracy
23	3	4	2	26	2	5	3	22	78.9%

As the results in Table 4.16 show, the proposed fault identification scheme can identify the faults in a satellite with a 78.9% classification accuracy rate.

4.9 Conclusion

In this chapter, a wavelet-entropy algorithm developed to autonomously detect faults in a reaction wheel actuators of a spacecraft. Our proposed fault detection scheme requires data from the absolute attitude measurements of satellite. According to the simulation results and confusion matrix evaluation criteria, it can be concluded that the proposed fault detection scheme is capable of detect high-severity faults in reaction wheel actuator, however our proposed fault detection scheme in not capable of detecting low severity faults in the reaction wheel actuator. In order to isolate and identify the faults in a satellite, the fault isolation and identification schemes were proposed based on discrete wavelet transform (DWT), relative wavelet energy (RWE)

and multilayer perceptron neural network (MLPNN). In the fault isolation scheme, the features from diagnostic signals (angular velocity measurements) are extracted and by considering the RWE of the approximation coefficients with threshold the fault is isolated. The fault identification is performed by obtaining the detail and approximation of the diagnostic signals (attitude measurements) and utilize these coefficients in an MLPNN for pattern classification. The results demonstrate that our proposed fault isolation scheme can isolate the faults with a 100% accuracy, however the proposed fault identification has a 78.9% classification accuracy rate. In the following chapter, a formation-level fault detection, isolation and identification (FDII) scheme based on relative attitude measurements and relative angular velocity measurements will be proposed and the results will be compared with the spacecraft-level FDII scheme.

Chapter 5

Formation-level Fault Detection, Isolation and Identification

Health monitoring in formation flying has an important and critical role in the spacecraft missions. It is obvious that formation of small spacecraft can perform the same duties of a single large spacecraft when the coordination of those small spacecraft fulfills the mission's requirements. Hence, detection of faults in actuators which could result in loss of coordination is highly desirable. In Chapter 4 we have developed a spacecraft-level fault detection, isolation and identification (FDII) scheme that was based on wavelet entropy for health monitoring reaction wheel actuators of a single spacecraft. The performance of our proposed fault detection scheme has been studied under different faulty scenarios. Confusion matrix results showed that by considering the absolute measurements in each satellite for fault detection, high-severity faults could be detected, however in low-severity fault scenarios the precision of fault detection is below requirements. Thus, development of an alternative fault detection system in formation flying is desirable.

In this chapter a formation-level FDII approach for formation flying is developed based on relative attitude and angular velocity measurements. In our proposed scheme, relative attitude and angular velocity measurements for each two neighboring satellites are considered as diagnostic signals and wavelet entropy is employed to detect faults in the spacecraft. An important advantage of this fault detection scheme is

that only relative measurements are used to detect abnormalities in the actuators and this fault detection method is independent with respect to absolute measurements in each satellite.

5.1 Formation Flying Simulation Environment

As mentioned in Chapter 3, in our simulation in order to simulate formation of flying spacecraft, a decentralized architecture is used to control a formation via virtual structure and a bidirectional ring topology is used to communicate the coordination variable instantiations, to bring each local instantiation into consensus.

Our simulations for the formation flying were developed in MATLAB and Simulink. In our simulations, we consider four spacecraft that perform formation maneuver. Each spacecraft in our simulation is distributed equally along a circle with a diameter of 1000 meter in the plane. The parameters that were used in our simulations for the formation flying of spacecraft are provided in Table 5.1.

Table 5.1: Simulation parameters for formation flying satellites.

Parameters	Value
Satellite weight	120 Kg
Inertia moment for each satellite	Ix = 9.8, Iy = 9.7, Iz = 9.75 Kgm^2
Orbit	685 Km
Orbital Period	97 min
Initial Euler Angles for satellite 1	[5,3,2] deg
Initial Euler Angles for satellite 2	[8,1,6] deg
Initial Euler Angles for satellite 3	[2,4,7] deg
Initial Euler Angles for satellite 4	[1,6,4] deg
desired angular velocity for all satellites	[0,0,0] $\frac{rad}{s}$
Desired Euler Angles	[75,15,20] deg
Maximum relative distance	1000 m

From the control point of view, the goal of formation flying control law defined in Chapter 3 is that the angular rotations and velocities of each spacecraft track a set of desired angular rotations and velocities of the formation. Table 5.2 shows the expected settling time and tracking errors that are used to evaluate the performance of the formation flying control law. The simulations that are performed in this chapter

have a final simulation time of 1000 sec.

Table 5.2: Expected settling time and tracking error in each satellite.

Variable	Settling time (sec)	Tracking error
q_1	300	1e-03
q_2	300	1e-03
q_3	300	1e-03
ω_{1x}	300	1e -5
ω_{1y}	300	1e -5
ω_{1z}	300	1e -5

Furthermore, the gains and parameters of the nonlinear controllers that are used in equations (3.17) and (3.21) are indicated in Table 5.3.

Table 5.3: Controller gains for each satellite and virtual structure.

Parameter	Value
K_G	$24I_{3\times3}$
K_S	$24I_{3\times3}$
K_F	$40I_{3\times3}$
k_q	$40I_{3\times3}$
k_ω	$20I_{3\times3}$

5.2 Proposed Formation-level Fault Detection Scheme

The formation-level fault detection is unique to multi platform missions. Individual spacecraft in the formation are considered as different components of the formation flying system. Therefore, at this level, fault detection is essentially the binary decision determining whether or not any fault exists in the formation components, i.e., in one or more satellites in the formation. At formation-level, fault detection is based on relative attitude information. In this section, formation-level fault detection (FLFD) approach is introduced and developed. In this approach, the spacecraft are in a ring topology and each satellite has two neighbors. The definition of a neighbor is as follows:

The satellite i is called a neighbor of satellite j, if satellite i receives attitude information from satellite j and vice versa.

For fault detection purposes, the similar steps that were used in Chapter 4 are deployed. The difference between these two schemes is that in the formation-level fault detection there are two relative diagnostic signals in each satellite that are used for fault analysis. The proposed formation-level fault detection scheme is described as follows:

- First, two relative signals in the fault analysis unit of each satellite are produced with respect to each neighbors of a given satellite. These two relative signals are the diagnostic signals of each spacecraft.

- The diagnostic signals are decomposed into details and approximation coefficients by using windowing discrete wavelet transform technique that is described in Chapter 4.

- The wavelet entropy of the coefficients for each window is calculated and the sum of the absolute wavelet entropy (SAWE) is calculated. In this step, there are two SAWEs in the fault analysis unit of each satellite with respect to each neighbor, the SAWE with respect to the neighbor left ($SAWE_{nl}$) and the SAWE with respect to the neighbor right ($SAWE_{nr}$) of a given satellite.

- The two SAWEs are compared with time-varying thresholds $threshold_{nr}$ and $threshold_{nr}$ defined as the threshold with respect to the neighbor left and the threshold with respect to the neighbor right respectively. If two SAWEs in one satellite have passed the threshold the fault will be detected and that satellite is designated as the faulty satellite. These steps are illustrated in the flowchart in Figure 5.1.

In order to analysis faults, first diagnostic signals must be produced in terms of the quaternions parameters. To reach this goal, relative attitudes of each two neighbor's of a given satellite are calculated and stored in the fault analysis unit of a given satellite. For instance; the relative attitude signals in the satellite 1 are produced as follows:

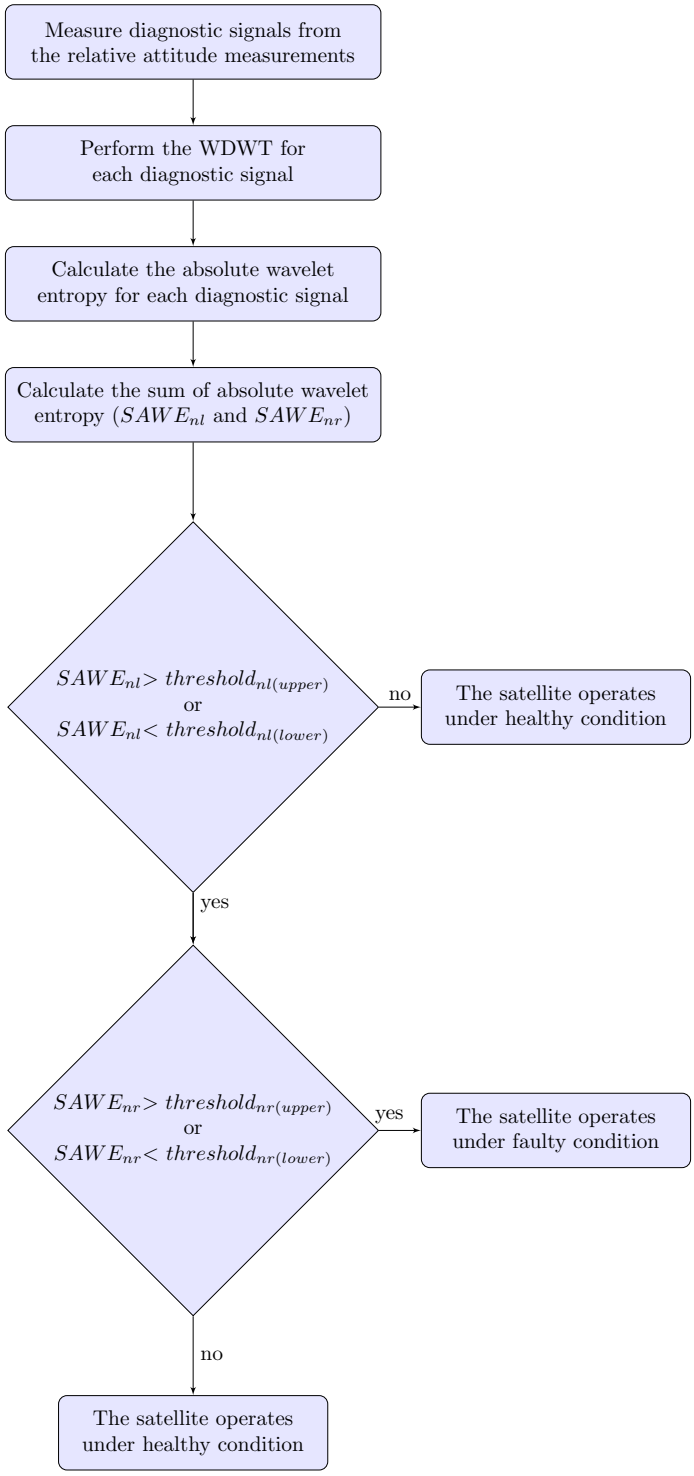

Figure 5.1: Flow chart of the proposed formation-level fault detection scheme.

- Relative attitude in satellite 1 with respect to satellite 2 is $Q_1 - Q_2$
- Relative attitude in satellite 1 with respect to satellite 4 is $Q_1 - Q_4$

where satellite 2 and satellite 4 are the two neighbors of the satellite 1 and Q denoted the attitude measurements of the satellites in terms of the quaternion parameters. These relative signals are illustrated in Fig 5.2. In this figure, Q_i represents the quaternion parameters of the attitude measurements of the satellite i ($i = 1, 2, 3, 4$).

In the next step, the DWT is applied to these diagnostic signals to decompose and produce details and approximation coefficients for each signal. Wavelet entropy of these coefficients are calculated and sum of the absolute entropy is calculated for each diagnostic signals as well. These SAWEs are compared with the time-varying thresholds that are produced in each window and the fault will be detected if the two SAWEs in each satellite have passed the thresholds. In formation-level fault detection scheme, similar to Chapter 4, in order to prevent false alarm the time delay parameter σ applied to our fault detection scheme. When the SAWEs passes the thresholds and this condition remains for period of σ second, then the faulty condition is established.

In order to inject faults in the ACS and evaluate the proposed formation-level fault detection scheme, the potential faults that were described in Chapter 4 are considered below.

5.3 Formation Flying Simulation Results

As mentioned before, in our simulations we consider four spacecraft that perform formation maneuver. We assume that the four spacecraft formation evolves like a rigid structure, that is, the formation shape is preserved and each spacecraft preserves a fixed relative orientation within the formation throughout the maneuvers. We simulate a scenario where the four spacecraft start from rest with some initial position and attitude errors and then perform a group rotation of desired attitude. Here, we assume that each place holder in the formation has the same orientation, that is, $Q = [q_1, q_2, q_3]$ is the same for each spacecraft. Since it is assumed that all four

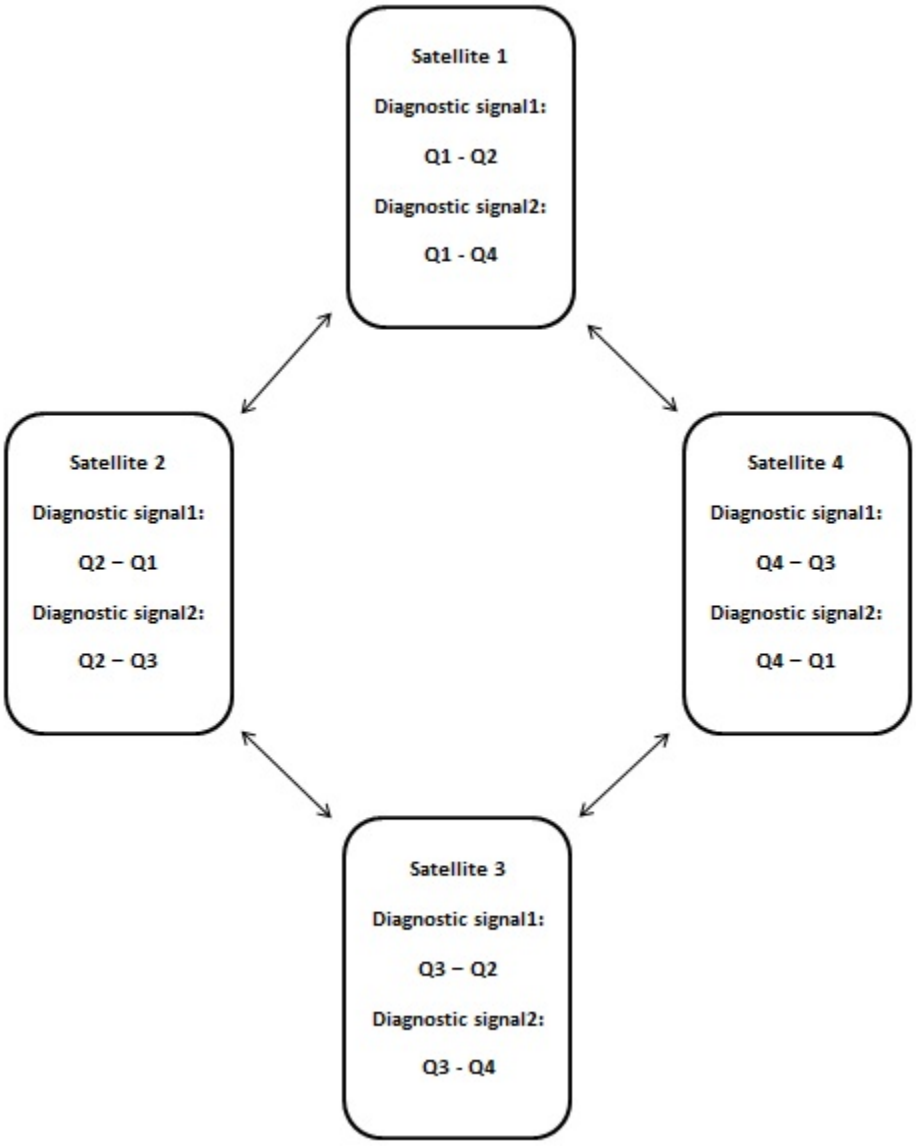

Figure 5.2: $SAWE_{nl}$ and $SAWE_{nr}$ in each fault analysis unit of four satellites in formation.

satellites are identical, hence in this section we show the simulation results for satellite 1 and these results are valid for the other satellites as well.

5.4 Simulation Results for the Healthy Scenario

Healthy scenario implies that the all the three reaction wheel actuators of each satellite are working properly during the commanded maneuver. Similar to Chapter 4, in our proposed FLFD scheme, we have used time-varying threshold technique to detect the faults in the satellites. The thresholds in this scheme are produced similar to the threshold scheme in Figure 4.1 in Chapter 4. The parameter δ must be defined under the healthy condition of satellites. In order to define this parameter, different healthy scenarios were simulated and by considering the SAWEs of the satellite in normal condition the δ has been defined. Table 5.4 illustrate the different attitude missions and the average of SAWEs of the satellite 1 in a formation flying mission under the healthy condition.

In our simulations the parameters $T_1,\ T_2,\ \delta_1$ and δ_2 are selected as:

$$\delta_1 = 3.172 \quad \delta_2 = 3.038 \quad T_1 = 5 \quad T_2 = 0.4$$

The time delay parameter for fault detection is selected as $\sigma = 10\ sec.$ The $SAWE_{nl}$ and $SAWE_{nr}$ for satellite 1 under the healthy condition and its thresholds are illustrated in Fig 5.3.

Table 5.4: The average of SAWEs in different attitude missions under the healthy operation condition in the formation flying satellites.

Desired attitude	Average of the SAWEs	Desired attitude	Average of the SAWEs
$[24, 209, 168]$	3.1292	$[89, 25, 17]$	3.1268
$[160, 110, 31]$	3.1253	$[43, 13, 80]$	3.1266
$[355, 126, 200]$	3.1215	$[340, 130, 300]$	3.1182
$[297, 303, 290]$	3.1284	$[30, 310, 45]$	3.1312
$[97, 257, 35]$	3.1294	$[124, 44, 19]$	3.1200
$[341, 166, 350]$	3.1237	$[90, 0, 0]$	3.1248
$[15, 40, 76]$	3.1304	$[173, 137, 86]$	3.1255
$[72, 64, 56]$	3.1225	$[45, 45, 45]$	3.1303
$[84, 279, 159]$	3.1274	$[20, 333, 31]$	3.1321
$[85, 66, 164]$	3.1223	$[0, 90, 0]$	3.1214
$[30, 45, 60]$	3.1189	$[180, 100, 57]$	3.1221
$[82, 3, 23]$	3.1218	$[0, 0, 90]$	3.1189
$[50, 29, 13]$	3.1319	$[22, 145, 35]$	3.1251
$[114, 227, 120]$	3.1298	$[10, 25, 90]$	3.1179
$[33, 89, 165]$	3.1208	$[30, 30, 30]$	3.1163
$[108, 130, 207]$	3.1171	$[43, 80, 34]$	3.1345
$[62, 11, 83]$	3.1180	$[12, 25, 46]$	3.1216
$[39, 103, 331]$	3.1232	$[90, 90, 90]$	3.1124
$[15, 25, 50]$	3.1151	$[67, 87, 69]$	3.1052
$[41, 60, 18]$	3.1263	$[13, 83, 41]$	3.1198

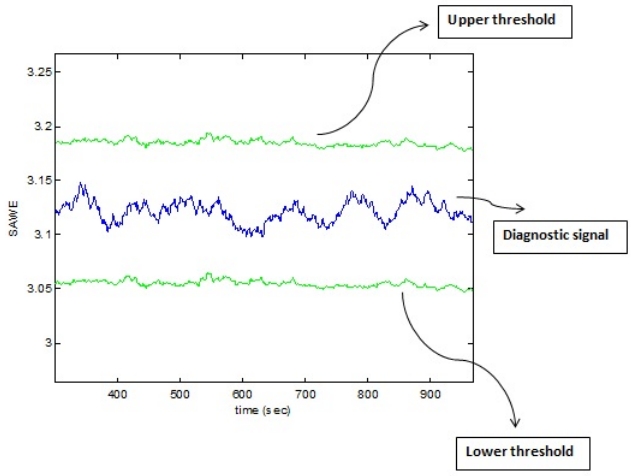

(a) $SAWE_{nl}$: SAWE of the satellite 1 with respect to satellite 2

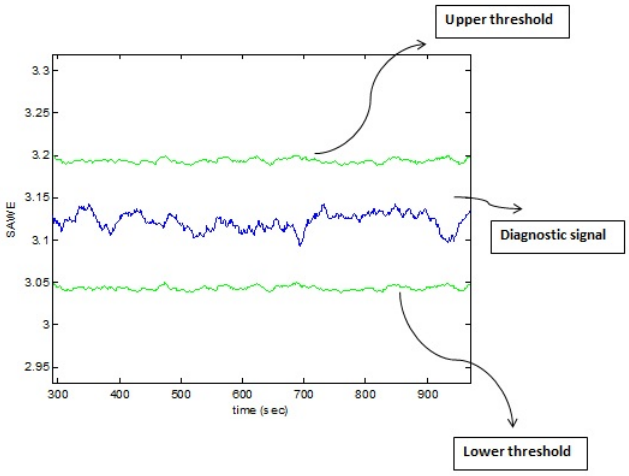

(b) $SAWE_{nr}$: SAWE of the satellite 1 with respect to satellite 4

Figure 5.3: $SAWE_{nl}$ and $SAWE_{nr}$ in the satellite 1 with respect to its neighbors under the healthy scenario.

5.5 Simulation Results for the Bus Voltage Fault Scenario

In the bus voltage fault scenario, low bus voltage condition is considered in the reaction wheel in satellite 1 as a fault. In order to simulate this fault scenario, bus voltage is dropped by 25%, 26%, 27%, 28%, 29%, 30%, 31%, 32%, 33%, 34%, 35%, 36%, 37%, 38%, 39% and 40% from its nominal value in $t = 600sec$. Similar to Chapter 4, all simulation results are obtained with nominal level of noise in the satellites. The two SAWEs for satellite 1 in this fault scenario are illustrated in Figures 5.4, 5.5, 5.6 and 5.7 and the fault detection times for this fault scenario are indicated in Table 5.5. As the results show our proposed FLFD is capable of detecting at least 27% bus voltage fault that this fault could not be detected in the spacecraft-level fault detection thar proposed in Chapter 4. However, for smaller percentage drop in the bus voltage this scheme cannot detect that faults in the reaction wheel.

The two SAWEs for satellite 2 with respect to its neighbors are illustrated in

Figure 5.8. In this figure the $SAWE_{nl}$ in satellite 2 that is related to the satellite 1 was changed but $SAWE_{nr}$ that is related to the satellite 3 was not changed.

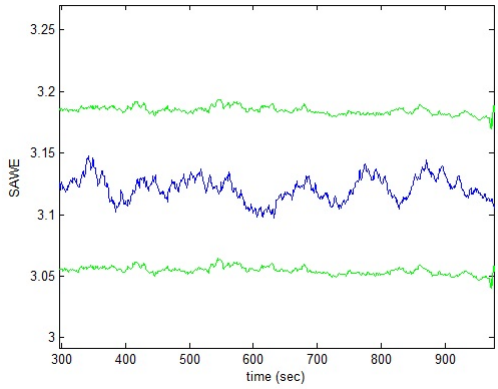

(a) $SAWE_{nl}$: SAWE of the satellite 1 with respect to satellite 2

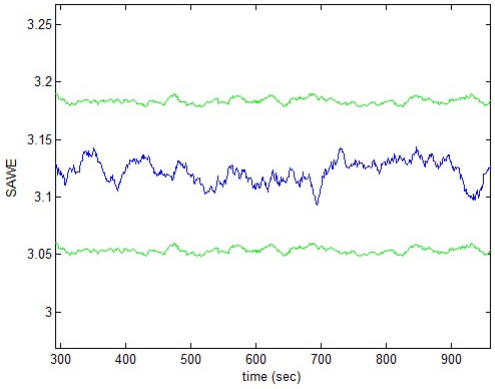

(b) $SAWE_{nr}$: SAWE of the satellite 1 with respect to satellite 4

Figure 5.4: $SAWE_{nl}$ and $SAWE_{nl}$ in the satellite 1 with respect to its neighbors under 25% drop in the bus voltage condition.

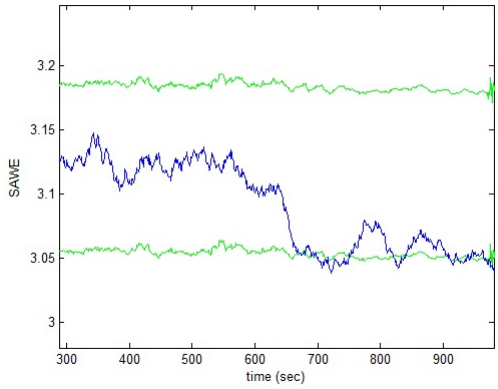

(a) $SAWE_{nl}$: SAWE of the satellite 1 with respect to satellite 2

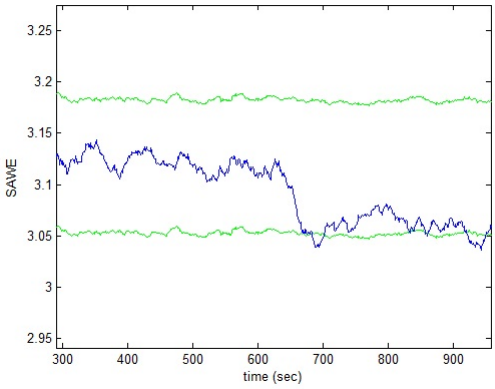

(b) $SAWE_{nr}$: SAWE of the satellite 1 with respect to satellite 4

Figure 5.5: $SAWE_{nl}$ and $SAWE_{nl}$ in the satellite 1 with respect to its neighbors under 26% drop in the bus voltage condition.

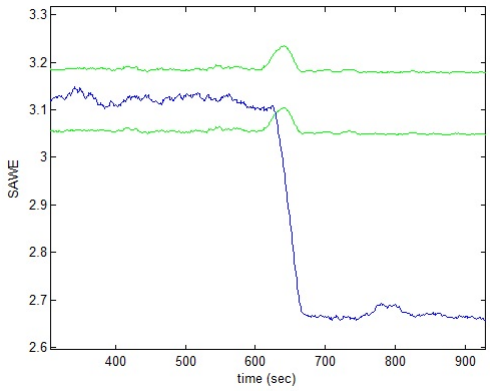

(a) $SAWE_{nl}$: SAWE of the satellite 1 respect to satellite 2

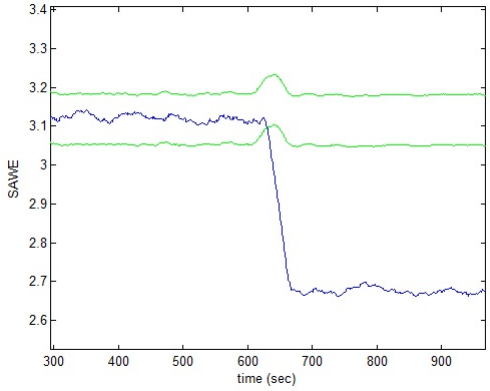

(b) $SAWE_{nr}$: SAWE of the satellite 1 with respect to satellite 4

Figure 5.6: $SAWE_{nl}$ and $SAWE_{nr}$ in the satellite 1 with respect to its neighbors under 27% drop in the bus voltage condition.

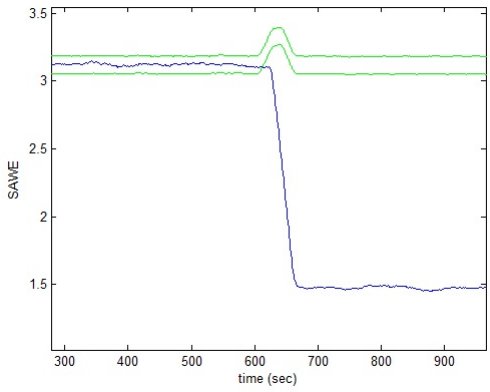

(a) $SAWE_{nl}$: SAWE of the satellite 1 respect to satellite 2

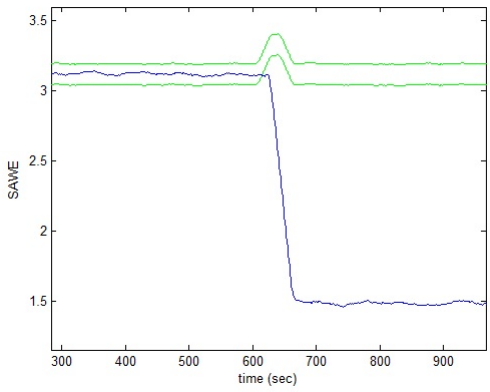

(b) $SAWE_{nr}$: SAWE of the satellite 1 with respect to satellite 4

Figure 5.7: $SAWE_{nl}$ and $SAWE_{nr}$ in the satellite 1 with respect to its neighbors under 28% drop in the bus voltage condition.

Figures 5.6 and 5.7 indicate that when the fault was injected in one satellite the two SAWEs in the faulty satellite are changed and pass the thresholds, hence fault will be detected in the faulty satellite.

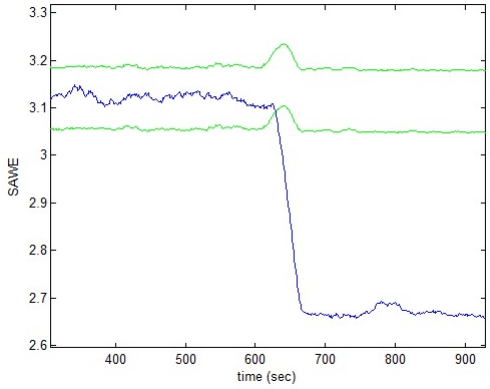

(a) $SAWE_{nl}$: SAWE of the satellite 2 with respect to satellite 1

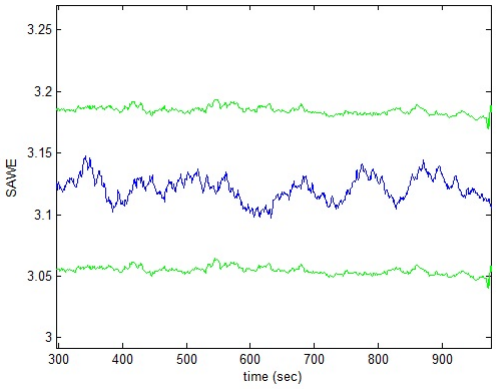

(b) $SAWE_{nr}$: SAWE of the satellite 2 with respect to satellite 3

Figure 5.8: $SAWE_{nl}$ and $SAWE_{nr}$ in the satellite 2 with respect to its neighbors in the satellite 1 faulty condition.

However, as Figure 5.8 indicates in the satellite 2 just one of the SAWE has passed the threshold (the one which is related to the satellite 1) and the other did not change. Similar to satellite 2, when the fault is injected in the satellite 1, in the satellite 4 only one of the two SAWEs has passed the thresholds and in the satellite 3, two SAWEs did not change. One can conclude that when both SAWEs in one satellite have passed the thresholds, that satellite is considered as a faulty satellite in the formation. Using this technique one can isolate faulty satellite in the formation.

Table 5.5: Fault detection time in satellite 1 for a bus voltage fault scenario.

Percentage drop in bus voltage	fault injection time (second)	fault detection time (second)
25	600	Not detected
26	600	Not detected
27	600	638
28	600	622
29	600	618
30	600	617
31	600	617
32	600	617
33	600	616
34	600	616
35	600	616
36	600	615
37	600	615
38	600	615
39	600	615
40	600	615

5.6 Simulation Results for the Motor Current Fault Scenario

In the motor current fault scenario, the motor torque gain K_t of the reaction wheel is dropped by 1%, 2%, 3%, 4%, 5%, 6%, 7%, 8%, 9%, 10%, 11%, 12%, 13%, 14% and 15% of its nominal value in satellite 1 at $t = 600sec$. The SAWEs of satellite 1 in this fault scenario are illustrated in Figures 5.9, 5.10 and 5.11 and the fault detection times are indicated in Table 5.6.

The results in these figures and Table 5.6 indicate that our proposed FLFD scheme

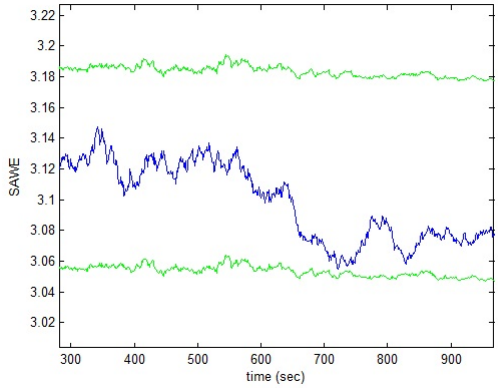

(a) $SAWE_{nl}$: SAWE of the satellite 1 with respect to satellite 2

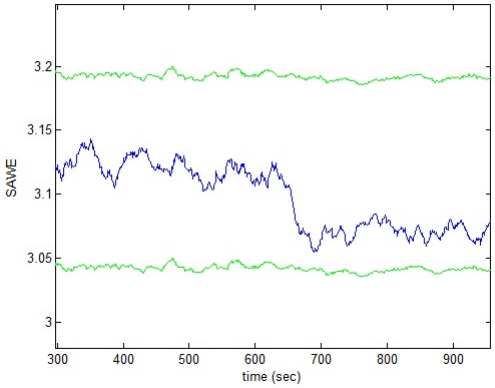

(b) $SAWE_{nr}$: SAWE of the satellite 1 with respect to satellite 4

Figure 5.9: $SAWE_{nl}$ and $SAWE_{nr}$ in the satellite 1 with respect to its neighbors under 1% drop in the motor torque gain.

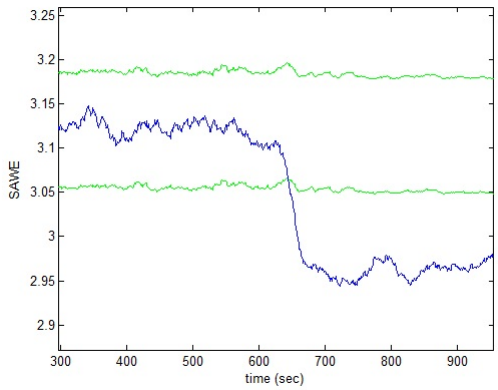

(a) $SAWE_{nl}$: SAWE of the satellite 1 with respect to satellite 2

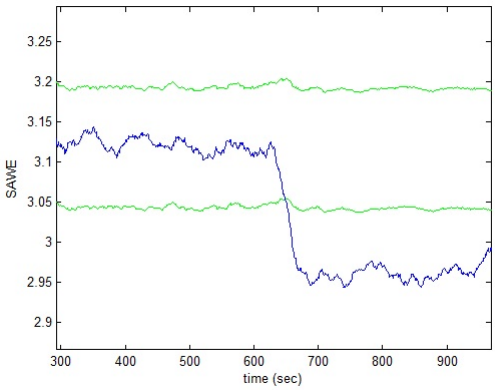

(b) $SAWE_{nr}$: SAWE of the satellite 1 with respect to satellite 4

Figure 5.10: $SAWE_{nl}$ and $SAWE_{nr}$ in the satellite 1 with respect to its neighbors under 2% drop in the motor torque gain.

is capable of detecting at least 2% drop in motor torque gain in the reaction wheel however it cannot detect 1% drop in motor torque gain in the reaction wheel. As the results indicate, our proposed scheme can detect both low-severity motor current faults in the reaction wheel in proper time interval which these faults cannot be detected in the spacecraft-level fault detection scheme.

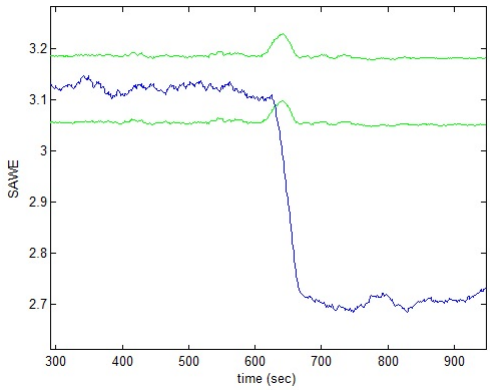

(a) $SAWE_{nl}$: SAWE of the satellite 1 with respect to satellite 2

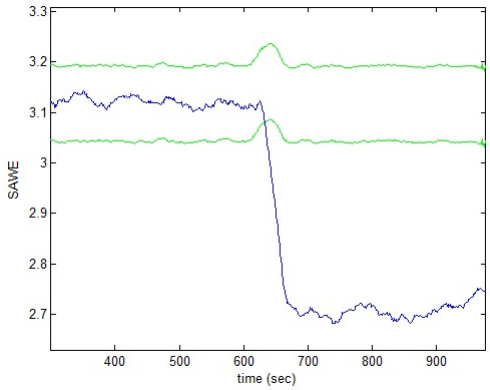

(b) $SAWE_{nr}$: SAWE of the satellite 1 with respect to satellite 4

Figure 5.11: $SAWE_{nl}$ and $SAWE_{nr}$ in the satellite 1 with respect to its neighbors under 3% drop in the motor torque gain.

Table 5.6: Fault detection time in the satellite 1 for the motor current fault scenario.

Percentage Drop in the Motor Torque Gain K_t	Fault Injection Time (second)	Fault Detection Time (second)
1	600	Not detected
2	600	651
3	600	638
4	600	627
5	600	625
6	600	624
7	600	622
8	600	621
9	600	620
10	600	620
11	600	619
12	600	619
13	600	619
14	600	618
15	600	618

5.7 Simulation Results for the Viscous Temperature Fault Scenario

In the viscous temperature fault scenario, the value of the viscous friction τ_v in satellite 1 decrease by 2%, 3%, 4%, 5%, 6%, 7%, 10%, 15%, 20%, 25% and of its value under the normal condition at $t = 600sec$. Figures 5.12, 5.13, 5.14 and 5.15 illustrate the two SAWEs in satellite 1.

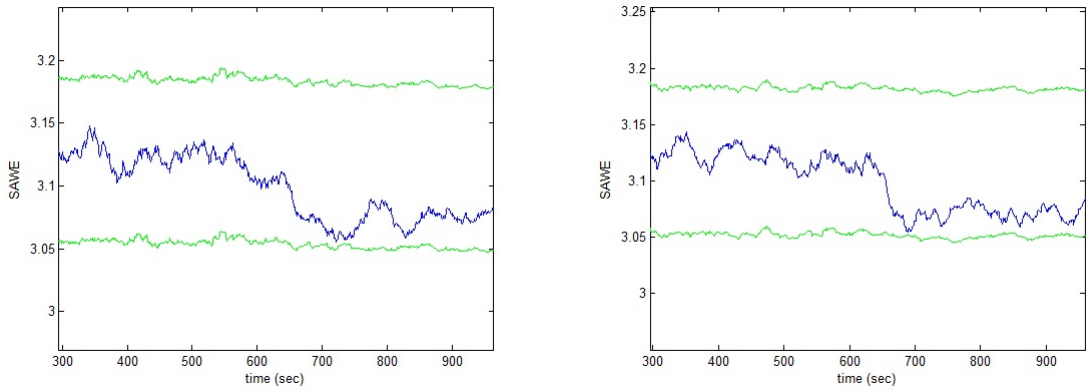

(a) $SAWE_{nl}$: SAWE of the satellite 1 with respect to satellite 2

(b) $SAWE_{nr}$: SAWE of the satellite 1 with respect to satellite 4

Figure 5.12: $SAWE_{nl}$ and $SAWE_{nr}$ in the satellite 1 with respect to its neighbors under 3% drop in τ_v.

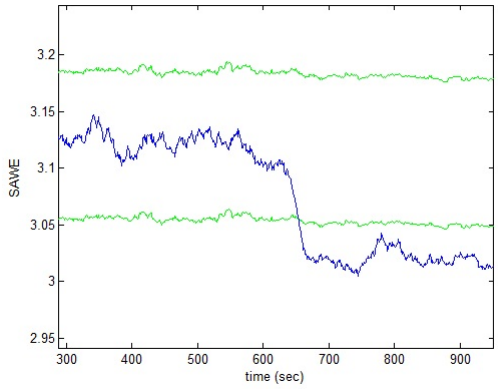

(a) $SAWE_{nl}$: SAWE of the satellite 1 with respect to satellite 2

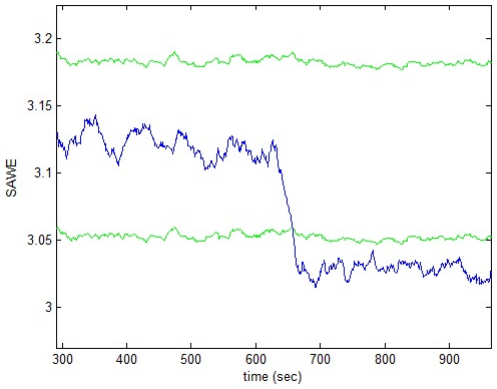

(b) $SAWE_{nr}$: SAWE of the satellite 1 with respect to satellite 4

Figure 5.13: $SAWE_{nl}$ and $SAWE_{nr}$ in the satellite 1 with respect to its neighbors under 4% drop in τ_v.

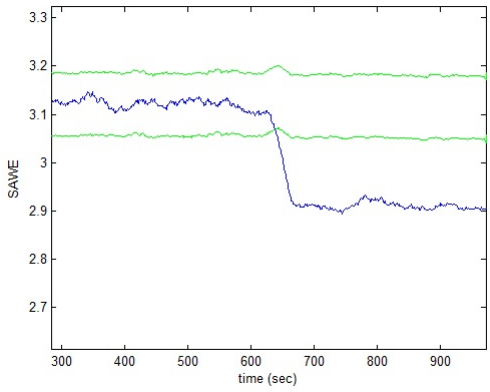

(a) $SAWE_{nl}$: SAWE of the satellite 1 with respect to satellite 2

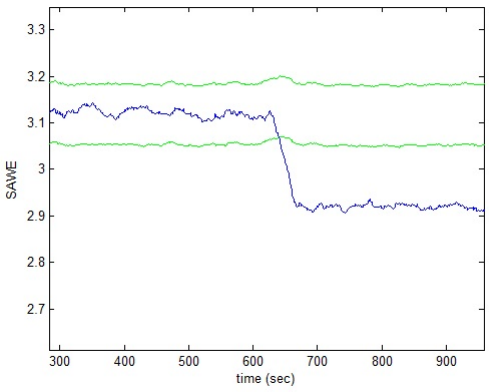

(b) $SAWE_{nr}$: SAWE of the satellite 1 with respect to satellite 4

Figure 5.14: $SAWE_{nl}$ and $SAWE_{nr}$ in the satellite 1 with respect to its neighbors under 5% drop in τ_v.

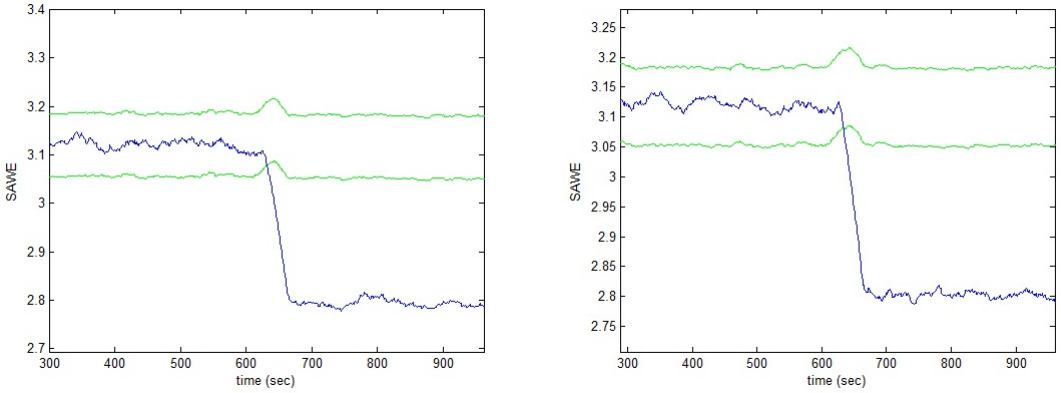

(a) $SAWE_{nl}$: SAWE of the satellite 1 with respect to satellite 2

(b) $SAWE_{nr}$: SAWE of the satellite 1 with respect to satellite 4

Figure 5.15: $SAWE_{nl}$ and $SAWE_{nr}$ in the satellite 1 with respect to its neighbors under 6% drop in τ_v.

The detection times for the temperature viscous fault scenarios are indicated in Table 5.7. As the results illustrate, this fault detection scheme can not detect lower than 4% drop in the viscous friction of the reaction wheel, however for at least 4% drop in the viscous friction of the reaction wheel, our proposed formation-level scheme can detect faults which these faults cannot be detected in the spacecraft-level fault detection scheme.

Table 5.7: Fault detection time in the satellite 1 for the viscous temperature fault scenario.

Percentage Drop in τ_v	Fault Injection Time (second)	Fault Detection Time (second)
2	600	Not detected
3	600	Not detected
4	600	660
5	600	646
6	600	638
7	600	636
10	600	626
15	600	622
20	600	620
25	600	619
30	600	619

5.8 Window Size Effects on Fault Detection

The sensevity of our scheme to the size of window is shown in Table 5.8. By chosing W=300, we can have the best fault detection time and as well low calculation and storage requirement in our simulations.

Table 5.8: Comparison of different window size in fault detection.

Window size	Injected fault in $t = 600sec$	Fault detection time (second)
50	27% drop in bus voltage	Not detected
100	27% drop in bus voltage	Not detected
150	27% drop in bus voltage	647
200	27% drop in bus voltage	642
250	27% drop in bus voltage	638
300	27% drop in bus voltage	638
350	27% drop in bus voltage	638
400	27% drop in bus voltage	638
50	2% drop in motor torque gain	Not detected
100	2% drop in motor torque gain	Not detected
150	2% drop in motor torque gain	Not detected
200	2% drop in motor torque gain	660
250	2% drop in motor torque gain	655
300	2% drop in motor torque gain	651
350	2% drop in motor torque gain	651
400	2% drop in motor torque gain	651
50	4% drop in viscous friction	Not detected
100	4% drop in viscous friction	Not detected
150	4% drop in viscous friction	Not detected
200	4% drop in viscous friction	Not detected
250	4% drop in viscous friction	662
300	4% drop in viscous friction	660
350	4% drop in viscous friction	660
400	4% drop in viscous friction	660

5.9 Confusion Matrix for the Fault Detection

As mentioned in Chapter 4, in order to evaluate the performance of our proposed fault detection scheme, the confusion matrix approach is used. From the total amount of simulation results for the reaction wheel actuators, the results for three fault scenarios are indicated in Tables 5.9, 5.10 and 5.11.

Table 5.9: Confusion matrix for the bus voltage fault scenario.

Percentage drop in bus voltage	t.n.	t.p.	f.n.	f.p.	Accuracy	Precision
25	N/A	N/A	N/A	N/A	N/A	N/A
26	N/A	N/A	N/A	N/A	N/A	N/A
27	49	50	1	0	99%	98%
28	49	50	1	0	99 %	98 %
29	50	50	0	0	100 %	100%
30	50	50	0	0	100 %	100%
31	50	50	0	0	100 %	100%
32	50	50	0	0	100 %	100%
33	50	50	0	0	100 %	100%
34	50	50	0	0	100 %	100%
35	50	50	0	0	100 %	100%
36	50	50	0	0	100 %	100%
37	50	50	0	0	100 %	100%
38	50	50	0	0	100 %	100%
39	50	50	0	0	100 %	100%
40	50	50	0	0	100 %	100%

Table 5.10: Confusion matrix for the motor current fault scenario.

Percentage drop in motor torque gain K_t	t.n.	t.p.	f.n.	f.p.	Accuracy	Precision
1	N/A	N/A	N/A	N/A	N/A	N/A
2	46	50	4	0	96%	92%
3	49	50	1	0	99 %	98%
4	50	50	0	0	100%	100%
5	50	50	0	0	100%	100%
6	50	50	0	0	100%	100%
7	50	50	0	0	100%	100%
8	50	50	0	0	100%	100%
9	50	50	0	0	100%	100%
10	50	50	0	0	100%	100%
11	50	50	0	0	100%	100%
12	50	50	0	0	100%	100%
13	50	50	0	0	100%	100%
14	50	50	0	0	100%	100%
15	50	50	0	0	100%	100%

Table 5.11: Confusion Matrix for the viscous temperature fault scenario.

Percentage drop in viscous friction gain τ_v	t.n.	t.p.	f.n.	f.p.	Accuracy	Precision
2	NA	NA	NA	NA	NA	NA
3	NA	NA	NA	NA	NA	NA
4	44	50	6	0	94 %	88 %
5	47	50	3	0	97 %	94 %
6	49	50	1	0	99 %	98%
7	50	50	0	0	100 %	100%
10	50	50	0	0	100 %	100%
15	50	50	0	0	100 %	100%
20	50	50	0	0	100 %	100%
25	50	50	0	0	100 %	100%
30	50	50	0	0	100 %	100%

The results in Table 5.9 indicate that for the bus voltage fault scenario, our proposed scheme can detect 27% drop in the voltage bus with a high level of accuracy (99%) and precision (98%). In the motor current fault scenario, our proposed FLFD scheme can detect 2% drop in the motor gain torque with 92% precision and 96% accuracy, and in the viscous temperature fault scenario, 4% drop in viscous friction in the satellite 1 could be detected with 94% accuracy and 88% precision level. These results indicate that our proposed formation-level fault detection scheme has strong capability of detecting both high-severity and low-severity faults in the satellites with high level of accuracy and precision as compared to the spacecraft-level fault detection scheme presented in Chapter 4.

5.10 Proposed Formation-level Fault Isolation and Identification Scheme

In our formation-level fault diagnosis system, there is one fault analysis unit in each spacecraft that detect, isolate and identify the faults in a satellite. When a fault is detected and the faulty satellite is determined, the next steps are to isolate the fault in a satellite and identify the type of the fault (bus voltage, motor current or viscous temperature fault). In order to isolate the fault in a satellite the relative angular velocities are chosen as diagnostic signals and in order to identify the type of fault in the reaction wheel, the relative attitude measurements are chosen as diagnostic signals in our fault isolation and identification (FII) scheme.

Since in our simulations it is assumed that only one satellite has a fault and its two neighbors are working under a healthy condition, there is no difference between the two relative attitudes and angular velocities in the faulty satellite for the FII step. Therefore, in our simulations as we injected fault in the satellite 1, we consider relative angular velocities $\omega_1 - \omega_2$ as diagnostic signal for fault isolation purpose and also the relative attitude $Q_1 - Q_2$ in the satellite 1 as diagnostic signals for fault identification, where $\omega_1 = [\omega_{1x}, \omega_{1y}, \omega_{1z}]$, $\omega_2 = [\omega_{2x}, \omega_{2y}, \omega_{2z}]$, $Q_1 = [q_{11}, q_{12}, q_{13}]$ and $Q_2 = [q_{21}, q_{22}, q_{23}]$ are the angular velocities and the attitude measurements of the satellite 1 and satellite 2, respectively.

5.10.1 Proposed Fault Isolation Scheme

In our proposed fault isolation scheme, in order to isolate the fault in a faulty satellite, the relative wavelet energy (RWE) technique is used. As mentioned before, the relative angular velocity measurements are used as diagnostic signals in our fault isolation scheme. The level of decomposition in this scheme is selected as L=1. Similar to Chapter 4, in this scheme the RWEs of approximation coefficients are considered for fault isolation purpose. Table 5.12 illustrate the average of the RWEs of the relative angular velocity measurements in three axes of a satellite 1 under different fault

scenarios.

Table 5.12: Average of the RWEs of the relative angular velocity measurements in a satellite 1.

Fault scenario	$\omega_{1x} - \omega_{2x}$	$\omega_{1y} - \omega_{2y}$	$\omega_{1z} - \omega_{2z}$
Bus voltage	[0.9921 0.0079]	[0.9922 0.0078]	[0.9920 0.008]
Motor current in x-axis	[0.9391 0.0609]	[0.5233 0.4768]	[0.5233 0.4768]
Viscous temperature in x-axis	[0.9792 0.0208]	[0.5233 0.4768]	[0.5233 0.4768]
Motor current in y-axis	[0.5233 0.4768]	[0.9443 0.0557]	[0.5233 0.4768]
Viscous temperature in y-axis	[0.5233 0.4768]	[0.9797 0.203]	[0.5233 0.4768]
Motor current in z-axis	[0.5233 0.4768]	[0.5233 0.4768]	[0.9434 0.0566]
Viscous temperature in z-axis	[0.5233 0.4768]	[0.5233 0.4768]	[0.9794 0.0206]

As the results in Table 5.12 indicate, by considering the change of RWE of the approximation the fault can be isolated in a satellite.

In order to isolate the fault, we consider a threshold for the RWEs of approximation for $\omega_{1x} - \omega_{2x}$, $\omega_{1y} - \omega_{2y}$ and $\omega_{1z} - \omega_{2z}$. If the value of the RWEs of each relative angular velocity passes its threshold the fault is isolated. The process of determining the threshold is similar to the fault isolation scheme in Chapter 4.

In order to define the threshold for each relative angular velocity measurement, the RWEs in the healthy condition are considered and according to threshold scheme in Figure 4.1 the parameter δ is defined. Table 5.13 indicate the values of the RWEs in the healthy condition for each angular velocity measurement in a satellite.

The value of δ is selected as $\delta = 0.42$ and the parameters T_1 and T_2 are selected as $T_1 = 5$ and $T_2 = 0.4$. The RWE of the approximation coefficients in three axes of a satellite under three fault scenarios are illustrated in Figures 5.16, 5.17, 5.18, 5.19, 5.20, 5.21 and 5.22. As seen in these figures, the fault can be isolated by considering the RWEs of the approximation coefficient of the diagnostic signals.

Table 5.13: The average of the RWEs of the approximation coefficient of the relative angular velocity measurements in a satellite.

Desired missions	$\omega_{1x} - \omega_{2x}$	$\omega_{1y} - \omega_{2y}$	$\omega_{1z} - \omega_{2z}$	Desired missions	$\omega_{1x} - \omega_{2x}$	$\omega_{1y} - \omega_{2y}$	$\omega_{1z} - \omega_{2z}$
$[24, 209, 168]$	0.2183	0.2759	0.2426	$[13, 83, 41]$	0.2551	0.2270	0.2280
$[89, 25, 17]$	0.2554	0.2396	0.2660	$[41, 60, 18]$	0.2474	0.2483	0.2225
$[160, 110, 31]$	0.2407	0.2727	0.2350	$[67, 87, 69]$	0.2834	0.2713	0.2949
$[43, 13, 80]$	0.2910	0.2659	0.2926	$[15, 25, 50]$	0.2370	0.2334	0.2489
$[355, 126, 200]$	0.2699	0.2866	0.2389	$[90, 90, 90]$	0.2528	0.2498	0.2878
$[340, 130, 300]$	0.2360	0.2556	0.2329	$[39, 103, 331]$	0.2267	0.3101	0.2802
$[297, 303, 290]$	0.2511	0.2852	0.2428	$[12, 25, 46]$	0.2882	0.2887	0.2275
$[30, 310, 45]$	0.2514	0.2337	0.3026	$[62, 11, 83]$	0.2896	0.2933	0.2617
$[97, 257, 35]$	0.2331	0.2610	0.2602	$[43, 80, 34]$	0.2560	0.2634	0.2527
$[124, 44, 19]$	0.2581	0.2842	0.2268	$[108, 130, 207]$	0.2714	0.1829	0.2480
$[341, 166, 350]$	0.2722	0.2426	0.2453	$[30, 30, 30]$	0.2236	0.2220	0.2537
$[90, 0, 0]$	0.2338	0.2737	0.2204	$[33, 89, 165]$	0.3012	0.2162	0.2469
$[15, 40, 76]$	0.2326	0.2836	0.2730	$[10, 25, 90]$	0.2535	0.2700	0.2300
$[173, 137, 86]$	0.2501	0.3166	0.2679	$[114, 227, 120]$	0.2451	0.2449	0.2640
$[72, 64, 56]$	0.3085	0.2381	0.2951	$[22, 145, 35]$	0.2618	0.2238	0.2356
$[45, 45, 45]$	0.2416	0.2262	0.2218	$[50, 29, 13]$	0.2785	0.2508	0.2388
$[84, 279, 159]$	0.2955	0.2494	0.2472	$[0, 0, 90]$	0.2524	0.2665	0.2031
$[20, 333, 31]$	0.2454	0.2530	0.3244	$[82, 3, 23]$	0.2930	0.2291	0.2821
$[85, 66, 164]$	0.2517	0.2142	0.2012	$[180, 100, 57]$	0.2225	0.2629	0.2261
$[0, 90, 0]$	0.2673	0.2697	0.2733	$[30, 45, 60]$	0.2661	0.2095	0.2917

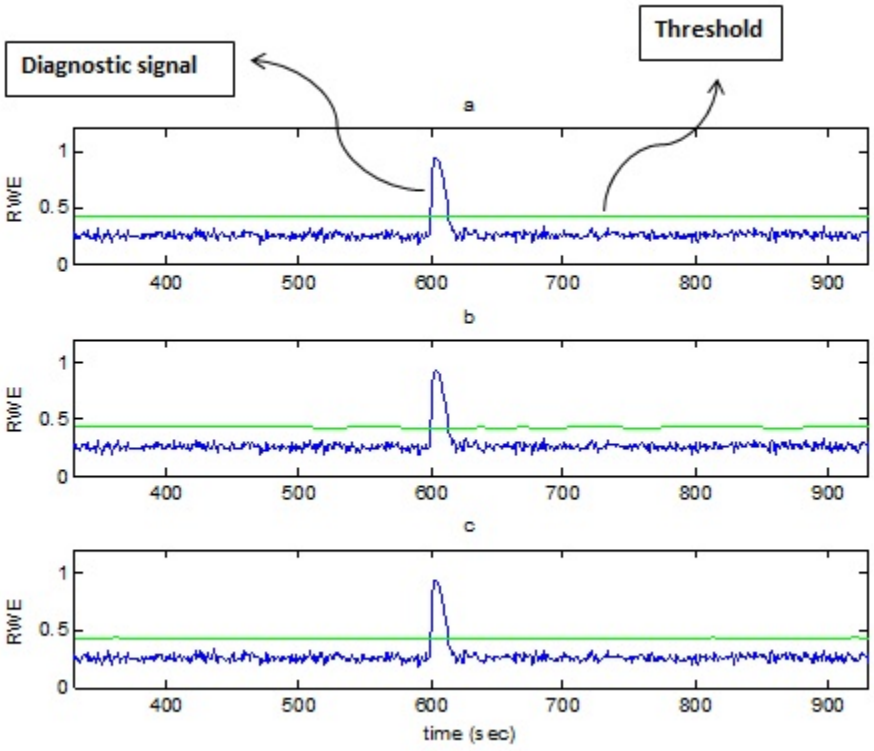

Figure 5.16: The RWEs of the approximation coefficients for three angular velocity measurements in a satellite under the bus voltage fault scenario. $a = \omega_x$, $a = \omega_{1x} - \omega_{2x}$, $b = \omega_{1y} - \omega_{2y}$, $c = \omega_{1z} - \omega_{2z}$.

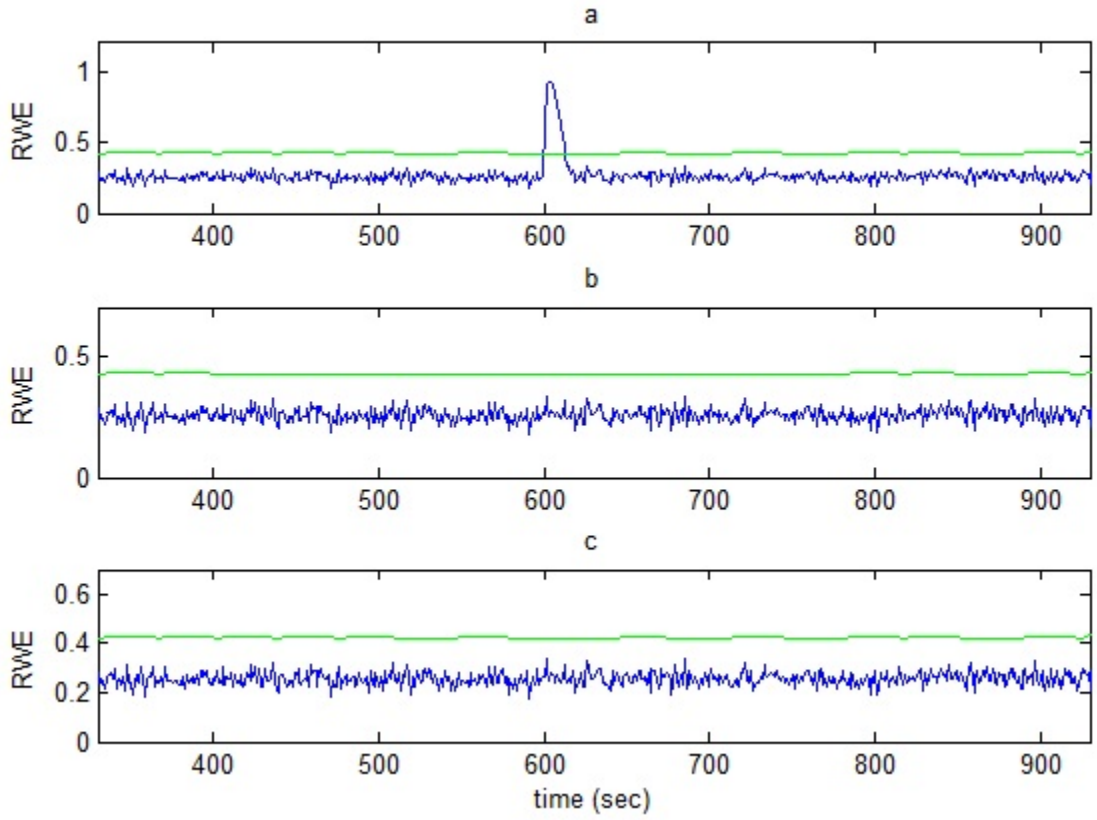

Figure 5.17: The RWEs of the approximation coefficients for three angular velocity measurements in a satellite under the motor current fault scenario in the x-axis. $a = \omega_{1x} - \omega_{2x}$, $b = \omega_{1y} - \omega_{2y}$, $c = \omega_{1z} - \omega_{2z}$.

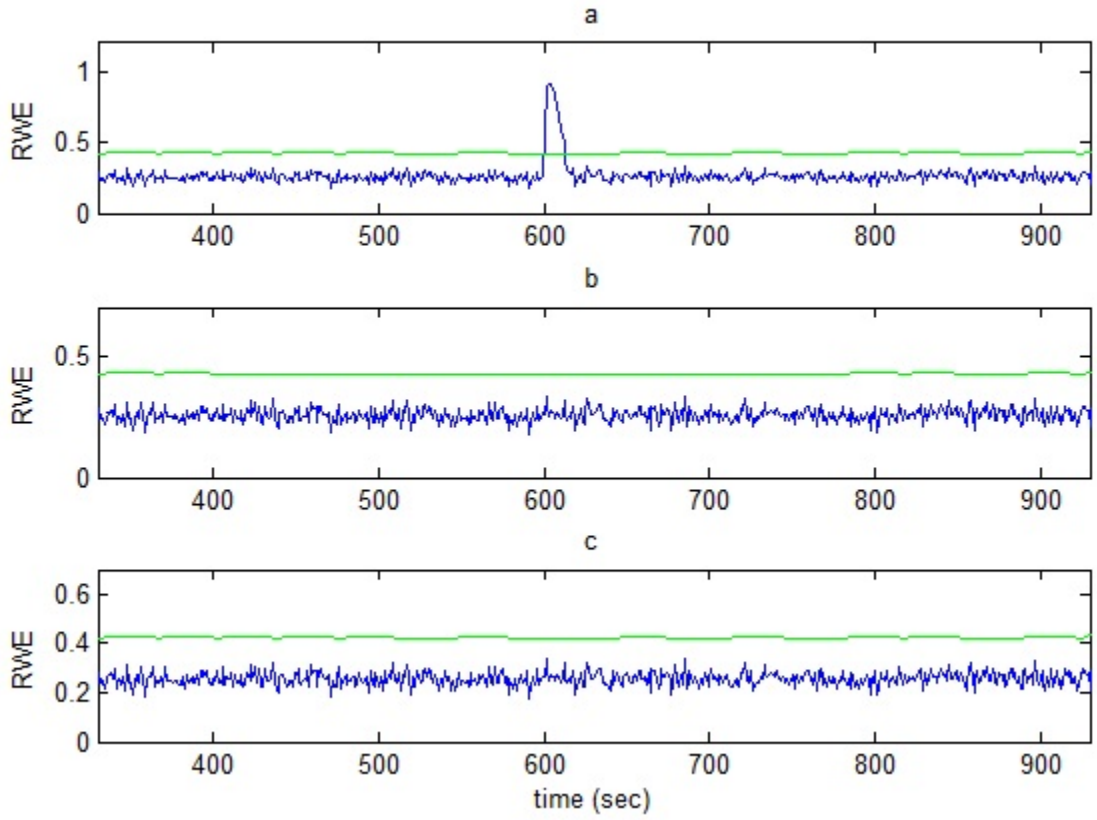

Figure 5.18: The RWEs of the approximation coefficients for three angular velocity measurements in a satellite under the viscous temperature fault scenario in the x-axis. $a = \omega_{1x} - \omega_{2x}$, $b = \omega_{1y} - \omega_{2y}$, $c = \omega_{1z} - \omega_{2z}$.

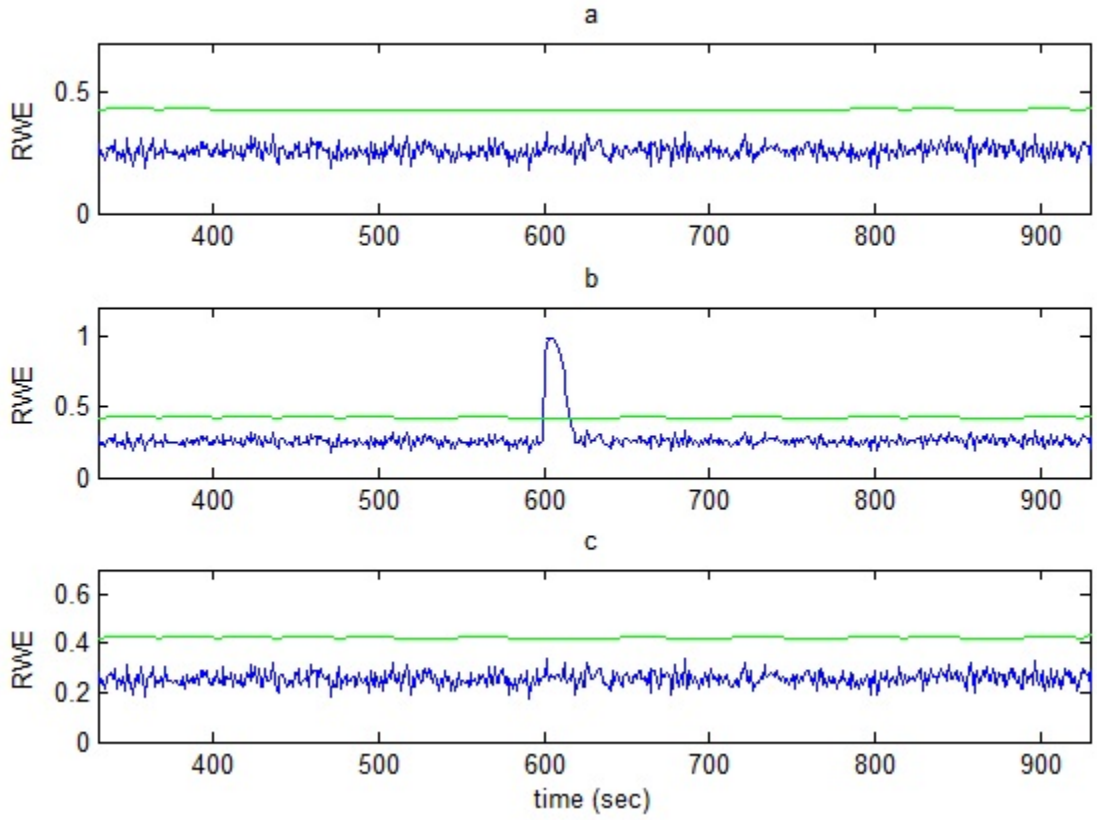

Figure 5.19: The RWEs of the approximation coefficients for three angular velocity measurements in a satellite under the motor current fault scenario in the y-axis. $a = \omega_{1x} - \omega_{2x}$, $b = \omega_{1y} - \omega_{2y}$, $c = \omega_{1z} - \omega_{2z}$.

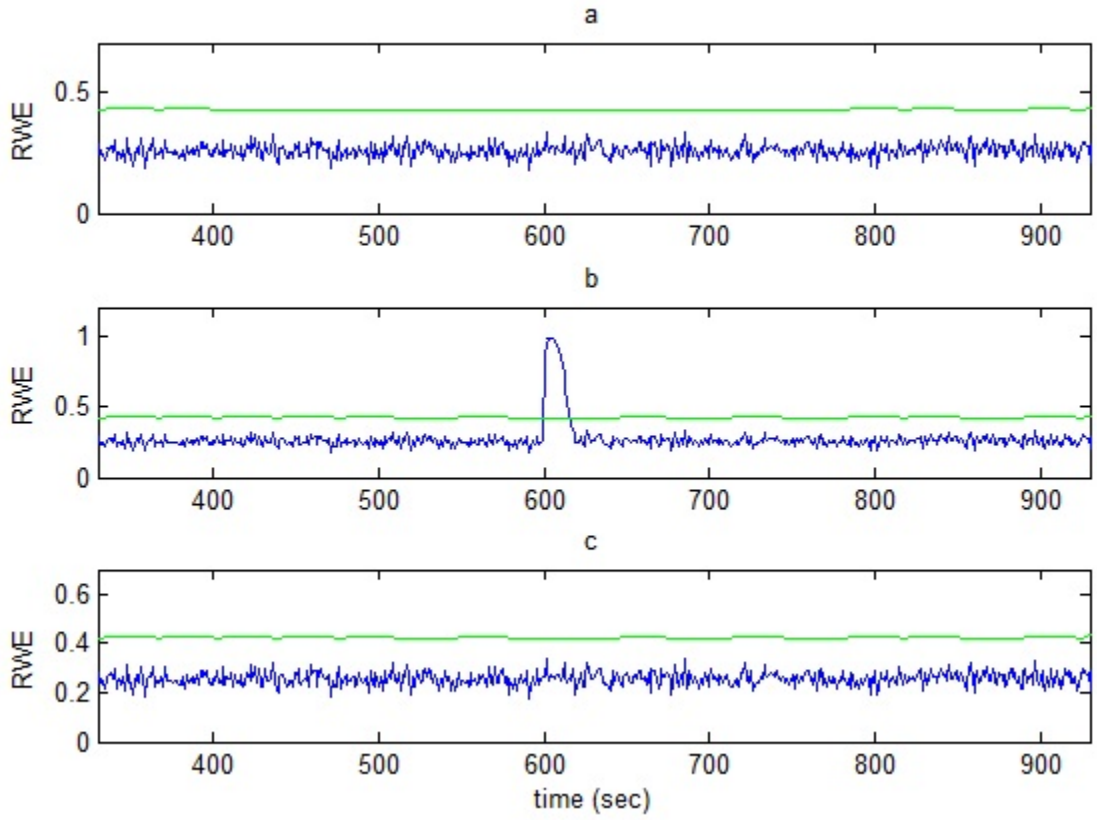

Figure 5.20: The RWEs of the approximation coefficients for three angular velocity measurements in a satellite under the viscous temperature fault scenario in the y-axis. $a = \omega_{1x} - \omega_{2x}$, $b = \omega_{1y} - \omega_{2y}$, $c = \omega_{1z} - \omega_{2z}$.

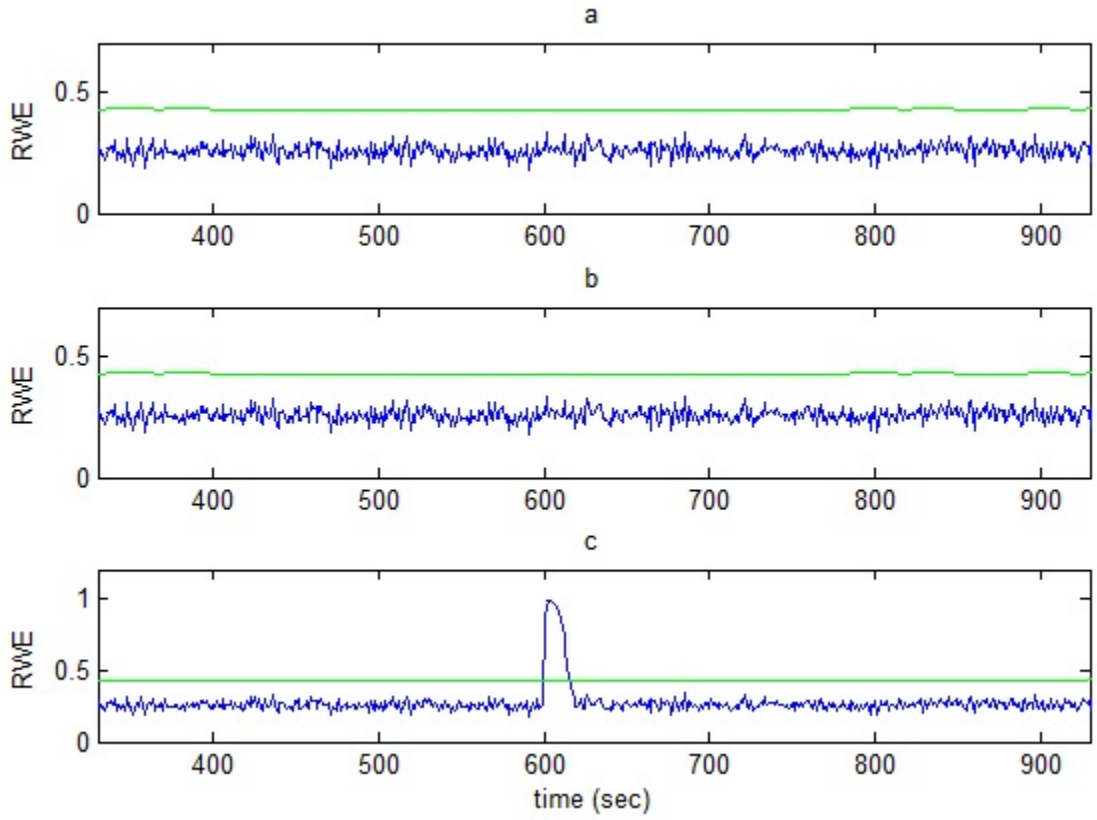

Figure 5.21: The RWEs of the approximation coefficients for three angular velocity measurements in a satellite under the motor current fault scenario in the z-axis. $a = \omega_{1x} - \omega_{2x}$, $b = \omega_{1y} - \omega_{2y}$, $c = \omega_{1z} - \omega_{2z}$.

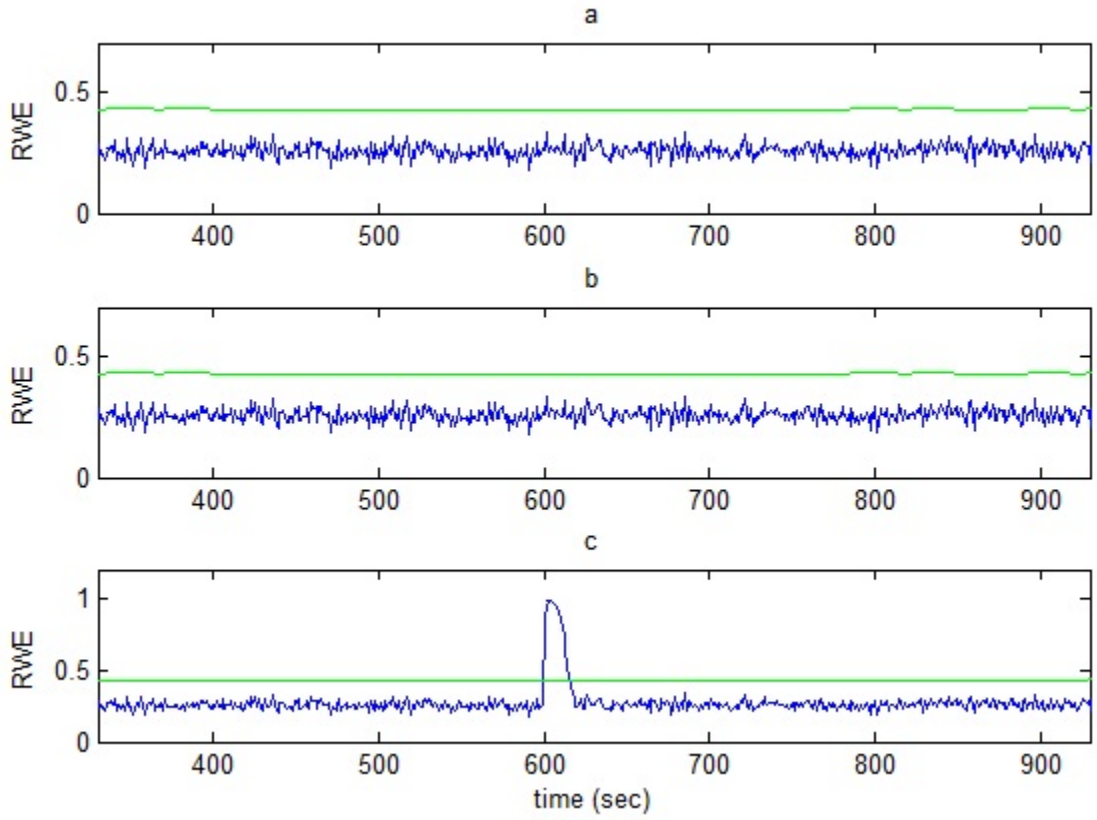

Figure 5.22: The RWEs of the approximation coefficients for three angular velocity measurements in a satellite under the viscous temperature fault scenario in the z-axis. $a = \omega_{1x} - \omega_{2x}$, $b = \omega_{1y} - \omega_{2y}$, $c = \omega_{1z} - \omega_{2z}$.

The confusion matrix for the fault isolation is indicated in Table 5.14.

Table 5.14: Confusion matrix for the fault isolation.

Fault scenario	cm_{11}	cm_{12}	cm_{13}	cm_{21}	cm_{22}	cm_{23}	cm_{31}	cm_{32}	cm_{33}
Bus voltage	10	0	0	0	10	0	0	0	10
Motor current	10	0	0	0	10	0	0	0	10
Viscous temperature	10	0	0	0	10	0	0	0	10

The results in Table 5.4 indicate that our proposed formation-level fault isolation can isolate all injected faults in a satellite without any misclassification.

5.10.2 Proposed Fault Identification Scheme

After the fault is isolated in a satellite the next step is to identify the type of the fault in a reaction wheel. This step in known as the fault identification. As mentioned before, the diagnosis signals in our fault identification scheme are relative attitude measurements in each satellite. Our proposed formation-level fault identification scheme is illustrated in Figure 5.23. As this figure shows, two major tasks must be performed in order to identify the faults: feature extraction and pattern classification.

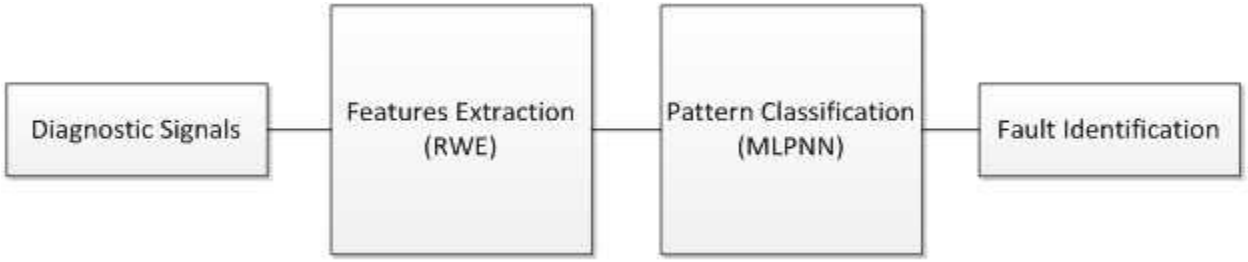

Figure 5.23: Proposed scheme for formation-level fault identification.

Feature Extraction

The feature extraction in our proposed fault identification scheme is performed by utilizing the relative wavelet energy (RWE) of the diagnostic signals. The diagnostic signals are decomposed by using discrete wavelet transform and detail and approximation coefficients are produced and then the RWEs of these coefficients are calculated. In our proposed fault identification scheme, the level of decomposition is chosen as L=3. Figure 5.24 illustrates the average of the RWEs of the diagnostic signals for different levels of decomposition. As this figure shows, by increasing the level of decomposition from 3 to 4 and higher the values of RWE for added detail coefficients did not give useful information as compared to the values of the other RWEs in the diagnostic signal. Hence, with 3 levels of decomposition one can have enough information about the diagnostic signal. By utilizing the RWEs of the relative attitude measurements one can identify the type of fault in the reaction wheel. In this step, the 12 RWEs with respect to three diagnostic signals are used as inputs for the MLPNN to identify the fault in the reaction wheel.

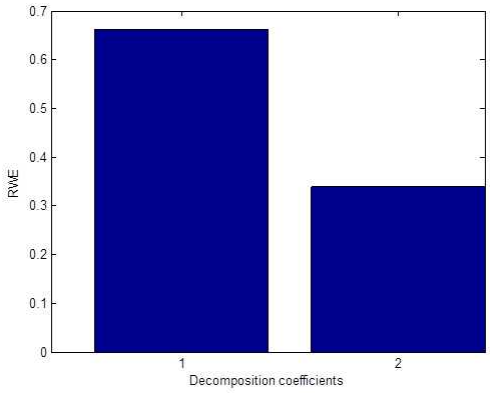

(a) $L = 1$

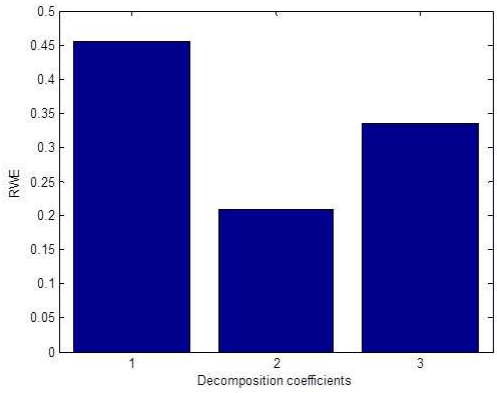

(b) $L = 2$

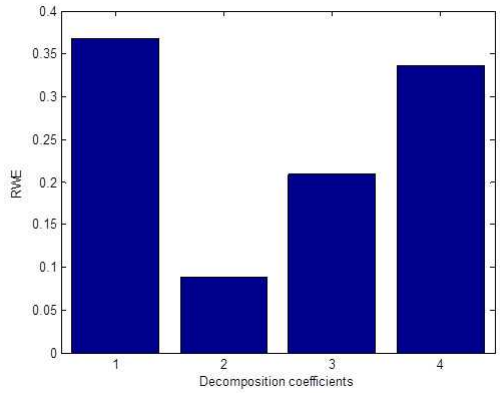

(c) $L = 3$

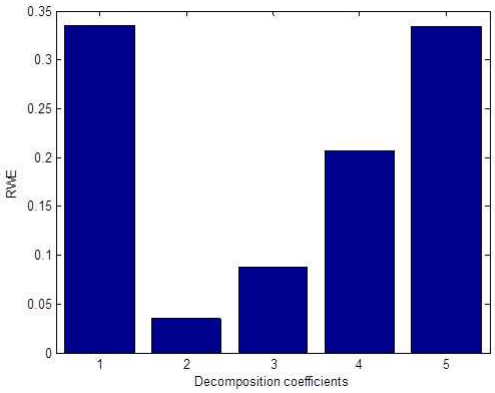

(d) $L = 4$

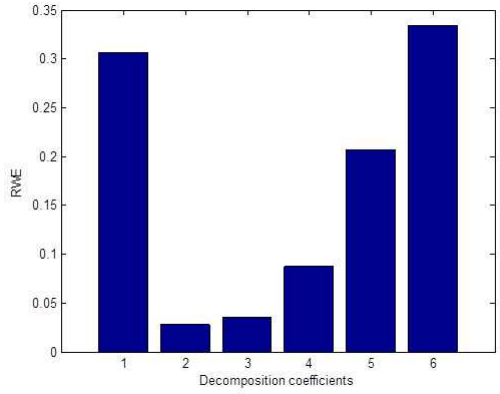

(e) $L = 5$

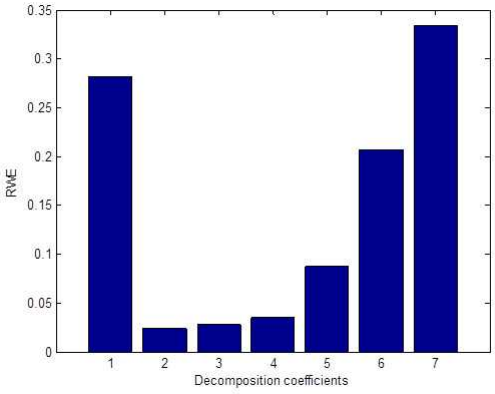

(f) $L = 6$

Figure 5.24: Comparison between the RWEs of the diagnostic signal with respect to different levels of decomposition.

For 3 levels of decomposition, we have 4 RWEs with respect to three details and

one approximation coefficients in each diagnosis signal. Hence, there are 12 RWEs with respect to three relative quaternions in a satellite that are used for pattern classification in the next step.

Pattern Classification

As Figure 5.23 shows, the extracted features are used for the pattern classification step. The pattern classification in our proposed fault identification scheme is performed by utilizing the multilayer perceptron neural network (MLPNN). In this step the RWEs of the diagnostic signals are used as inputs for the MLPNN in order to identify the fault.

As mentioned earlier, the MLPNN has 12 RWEs as inputs. The outputs of the MLPNN for fault identification are three types of the faults in a reaction wheel (bus voltage, motor current and viscous temperature). These fault types are assigned to three classes in the outputs of the MLPNN as shown in Table 5.15.

Table 5.15: Assigned classes for fault scenarios for the neural networks.

Fault Scenario	Assigned Class
Bus voltage	0 0 1
Motor current	0 1 0
Viscous temperature	1 0 0

The MLPNN for the fault identification scheme has 12 inputs, 10 neurons in the hidden layer and 3 outputs. The learning rate is chosen as 0.002 and the activation functions for the hidden layer are selected as hyperbolic tangent and for the output layer is selected as linear function. This network is trained with data under different fault scenarios in different attitude missions. After the training step, the MLPNN is validated to check the performance of the network. In the training phase, the parameters of the MLPNN are adjusted and then in the testing and validation steps, the network is tested and validated with new data sets to show that the accuracy of the network is valid for new data sets. 120 data are randomly chosen from the entire

210 data for training the network, 45 data are used for validating and 45 data are used for testing the network. Figure 5.25 illustrate the performance of the network in terms of the root mean square error.

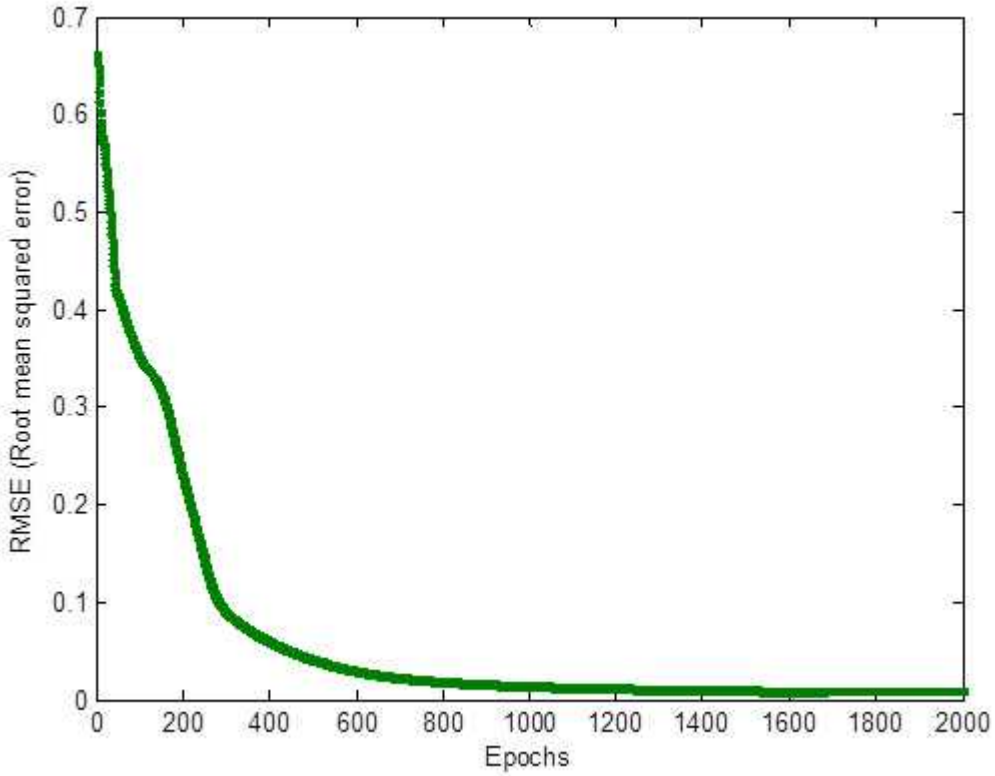

Figure 5.25: Performance of the proposed MLPNN for fault identification.

Table 5.16 shows the actual outputs and network outputs of the MLPNN for different fault scenarios in a satellite. In order to evaluate the performance of the MLPNN for fault identification, the confusion matrix criterion is used. This confusion matrix is a 3×3 that is defined in equation (4.19). The confusion matrix for fault identification is illustrated in Table 5.17.

Table 5.16: Output of the MLPNN for fault identification.

Actual output	Network output
0 0 1	0.018918 -0.00967 0.99075
0 1 0	0.018752 0.990969 -0.00972
1 0 0	0.962059 -0.00812 0.046063
0 0 1	0.018918 -0.00967 0.99075
0 1 0	0.018664 0.985983 -0.00465
1 0 0	0.962071 -0.00892 0.046846
0 0 1	0.036154 -0.00965 0.9735
0 1 0	0.018652 0.991042 -0.00969
1 0 0	0.961794 0.98918 -0.95097

Table 5.17: Confusion matrix for the fault identification.

cm_{11}	cm_{12}	cm_{13}	cm_{21}	cm_{22}	cm_{23}	cm_{31}	cm_{32}	cm_{33}	Classification accuracy
25	2	3	2	27	1	3	3	24	87.78%

As the results in Table 5.17 show, the proposed fault isolation scheme can isolate the faults in a satellite with a 87.78% classification accuracy rate.

5.11 Conclusion

In this chapter, the formation-level fault detection, isolation and identification (FDII) scheme based on discrete wavelet transform and neural networks is proposed and explained. In the fault detection method, the relative attitude measurements were utilized as diagnostic signals and sum of the absolute entropies were calculated and compared to their thresholds for fault detection purposes. The results illustrate that this fault detection scheme is capable of detecting low-severity faults in the reaction wheel actuator with high value of precision and accuracy as compared to the spacecraft-level fault detection scheme. For the fault isolation in a satellite, the relative wavelet energy technique was used in order to extract features from the diagnostic

signals and these features are compared to the defined thresholds to isolate the fault. In our fault identification scheme, the RWEs of the relative attitude measurements are utilized to identify the types of the faults in a satellite. The pattern classification in this scheme is performed by a multilayer perceptron neural network (MLPNN). The results illustrate that the classification accuracy for the fault identification in the formation-level is better than the classification accuracy in the spacecraft-level fault identification that were proposed in Chapter 4. These comparisons indicate that by utilizing the relative measurements in a satellite in a formation instead of the absulute measurements of each satellite, the fault detection and identification results have been improved.

Chapter 6

Conclusions and Future Work

In this thesis, the problem of fault detection, isolation and identification (FDII) in formation flying of satellites has been discussed and investigated. In Chapter 2, the fault detection and isolation problem was presented and different approaches for fault diagnosis in satellites are provided. In Chapter 3, the concept of coordinate systems and different attitude representations are provided and the formation flying architectures are also discussed. In this chapter the control law for the formation flying has been developed and different sensors and actuators that are used in the spacecraft are described. Furthermore, the mathematical model for the attitude torque disturbances that effect the satellite are provided in this chapter. In Chapter 4, different fault scenarios that may happen in the reaction wheel actuators are provided and explained. These fault scenarios are considered in this thesis to verify the proposed FDII scheme in satellites.

In this thesis the wavelet-entropy technique was used for fault detection purposes and in order to isolate the faults relative wavelet energy are utilized and in the fault identification scheme, the feature extraction is accomplished by the discrete wavelet transform and these features are identified by using multilayer perceptron neural networks (MLPNN). In this thesis two FDII systems have been proposed for fault diagnosis analysis in the satellites namely i) the spacecraft-level FDII scheme that has been proposed in Chapter 4, and ii) the formation-level FDII scheme that has been proposed in Chapter 5. In the spacecraft-level fault diagnosis, absolute attitude

measurements in terms of the quaternion parameters in a satellite are considered as diagnostic signals. These signals are decomposed with discrete wavelet transform and then the entropy of each signal is calculated. The sum of the absolute wavelet entropies (SAWE) are calculated and compared with time-varying thresholds. If this sum of absolute entropies passes the thresholds, the fault is detected otherwise the system works in normal condition.

In order to evaluate the proposed method, three different fault scenarios in the reaction wheel actuators are considered. The results indicate that the proposed spacecraft-level fault detection scheme can only detect high severity faults in the reaction wheels. In order to isolate the fault in a satellite, the angular velocity measurements are considered as diagnostic signals. In this scheme, the relative wavelet energy (RWE) technique is used to calculate the RWEs of diagnostic signals and these RWEs are compared with thresholds to isolate the faults. In order to identify the types of faults in reaction wheels, the fault identification scheme has been proposed. In this method, the features from the absolute attitude measurements are extracted with discrete wavelet transform (DWT) coefficients and these features are classified using a multilayer perceptron neural network (MLPNN).

The spacecraft-level FDII scheme can only detect, isolate and identify the high-severity faults in the reaction wheels, thus it is necessary to improve this method to detect and identify both low severity and high severity faults in the reaction wheels. For these reasons, the formation-level fault detection, isolation and identification scheme was proposed. In the formation-level fault detection, instead of absolute attitude measurements, relative attitude measurements in each satellite are considered as diagnostic signals. In this approach, each satellite has two neighbors and the SAWEs are calculated with respect to each neighbor. If the two SAWEs in one satellite pass the thresholds, that satellite is considered as a faulty satellite in the formation.

In the formation-level fault identification the relative angular velocity measurements are considered and in the fault identification the RWE technique is used to extract features from relative attitude measurements and these RWEs are fed into

MLPNN in order to identify the faults in a satellite. The confusion matrices for the formation-level fault isolation indicate that this FDII scheme can detect and isolate low severity faults with a high level of precision and accuracy.

6.1 Future Work

Base on the results that have been provided in this thesis, the future work can be concerned with the following issues:

- In this thesis, it is assumed that only one fault affects one of the reaction wheels in a satellite. Hence, the condition for more than one fault affecting the reaction wheels can be considered as a future work.
- The condition that more than one reaction wheel in a satellite were affected with faults were not considered in this thesis. This fault condition may be considered in future.
- This thesis focused on fault detection, isolation and identification in satellites. Hence, fault recovery in satellites may be considered as a future work in this area.
- In this thesis the ring topology is considered as a formation topology, hence other topologies in a formation flying satellites may be considered as a future work in fault diagnosis analysis.

Bibliography

[1] W. Ren, R. W. Beard, "A Decentralized Scheme for Spacecraft Formation Flying via the Virtual Structure Approach", *AIAA Journal of Guidance, Control and Dynamics*, Vol. 27, No. 1, pages 73 – 82, 2004.

[2] D. P. Scharf, F. Y. Hadaegh, S. R. Ploen, "A Survey of Spacecraft Formation Flying Guidance and Control (part I): Guidance", *Proceedings of the American Control Conference, Boston, MA*, pages 1733 – 1739, 2003.

[3] D. P. Scharf, F. Y. Hadaegh, S. R. Ploen. "A Survey of Spacecraft Formation Flying Guidance and Control (part II): Control", *Proceedings of the American Control Conference* , pages 2976 – 2985, 2004.

[4] P. K. C. Wang, F. Y. Hadaegh, "Coordination and Control of Multiple Microspacecraft Moving in Formation", *Journal of the Astronautical Sciences*, pages 315 – 355, 1996.

[5] R. W. Beard, J. Lawton, F.Y. Hadaegh, "A Coordination Architecture for Spacecraft Formation Control", *IEEE Trans. Control Syst. Technol*, pages 771 – 790, 2001.

[6] M. Mesbahi, F. Y. Hadaegh, "Formation Flying Control of Multiple Spacecraft via Graphs, Matrix Inequalities and Switching", *Journal of Guidance, Control and Dynamics*, pages 369 – 377, 2001.

[7] V. Manikonda, P. O. Arambel, M. Gopinathan, R. K. Mehra, F. Y. Hadaegh, "A Model Predictive Control-based Approach for Spacecraft Formation Keeping and Attitude Control", *Proceedings of the American Control Conference*, pages 4258 – 4262, 1999.

[8] R. S. Smith, F. Y. Hadaegh, "Parallel Estimation and Communication in Spacecraft Formations", *IFAC World Congress*, 2005.

[9] H. Wong, V. Kapila, A. G. Sparks, "Adaptive Output Feedback Tracking Control of Spacecraft Formation", *International Journal of Robust and Nonlinear Control*, *pages*117 – 139, 2002.

[10] M. Tillerson, J. P. How, "Formation Flying Control in Eccentric Orbits", *Proceedings of the AIAA Guidance, Navigation, and Control Conference*, 2001.

[11] B. J. Naasz, "Classical Element Feedback Control for the Spacecraft Orbital Maneuvers", *Master Thesis, Aerospace Engineering, Virginia Polytechnic Institute and State University*,2002.

[12] S. P. Hughes, "Formation Flying Performance Measures for Earth-Pointing Missions", *Master Thesis, Aerospace Engineering, Virginia Polytechnic Institute and State University*, 1999.

[13] M. Mitchell, L. Breger, J. P. How, "Effects of Navigation Filter Properties on Formation Flying Control", *AIAA Guidance, Navigation, and Control Conference and Exhibit*, 2004.

[14] V. Venkata, "Modelling and Control of Satellite Formations", *PhD Thesis, Aerospace Engineering, Texas A&M University*, 2003.

[15] Z. Wang, Y. Zhang, "Design and Verification of a Robust Formation Keeping Controller", *Journal of the International Academy of Astronautics, Acta Astronautica*, Vol. 61, Issues 7-8, pages 565 – 574, 2007.

[16] H. Wong, H. Pan, M. S. de Queiroz, V. Kapila, "Adaptive Learning Control for Spacecraft Formation Flying", *Proceedings of the 40h IEEE Conference on Decision and Control*, 2001.

[17] J. A. Roberts, "Satellite Formation Flying for an Interferometry Mission", *PhD Thesis, College of Aeronautics, Cranfield University*, 2005.

[18] M. Aung, A. Ahmed, M. Wette, D. Scharf, J. Tien, G. Purcell, M. Regehr, "An Overview of Formation Flying Technology Development for the Terrestrial Planet Finder Mission",*Proceedings on the 2004 IEEE Aerospace Conference*, 2004.

[19] M. R. LaPointe, "Formation Flying with Shepherd Satellites", *Ohio Aerospace Institute, NIAC Phase I presentation*, 2001.

[20] S. Persson, P. Bodin, E. Gill, J. Harr, J. Jorgensen, "PRISMA - An Autonomous Formation Flying Mission", *Small Satellite Systems and Services - The 4S Symposium*, 2006.

[21] M. Campbell, R. R. Fullmer, C. D. Hall, "The ION-F Formation Flying Experiments", *AAS/AIAA Space Flight Mechanics Meeting*, 2000.

[22] S. Gidlund, "Design Study for a Formation Flying Nanosatellite Cluster", *Master Thesis, Department of Space Science, Lulea University of Technology* , 2005.

[23] M. E. Campbell, V. Knagenhjelm, J. Yingling, "Flight Software Development for the ION-F Formation Flying Mission", *IEEE Proceedings on Aerospace Conference*, 2001.

[24] B. J. Makins, "Interferometer Architecture Trade Studies for the Terrestrial Planet Finder Mission", *Master Thesis, Massachusetts Institute of Technology*, 2002.

[25] T. Yairi, Y. Kawahara, R. Fujimaki, Y. Sato, K. Machida, "Telemetry-mining: A Machine Learning Approach to Anomaly Detection and Fault Diagnosis for Space Systems", *2nd IEEE International Conference on Space Mission Challenges for Information Technology*, 2006.

[26] I. A. Al-Zyoud, "Neural Network-based Actuator Fault Detection and Isolation for the Attitude Control Subsystem of a Satelite", *Msc Thesis, Concordia University*, 2005.

[27] F. Piromoradi, F. Sassini, C. W. da Silva, "An Efficient Algorithm for Health Monitoring and Fault Diagnosis in a Spacecraft Attitude Determination System", *IEEE International Conference on System, Man and Cybernetics ISIC* , 2007.

[28] E. C. Larson, B. E. Parker, B. R. Clark, "Model-Based Sensor and Actuator Fault Detection and Isolation", *Proceedings of the American Control Conference*, 2002.

[29] E. Wilson, C. Lages, R. Mah, "Gyro-based Maximum-Likelihood Thruster Fault Detection and Identification", *Proceedings of the American Control Conferences*, 2002.

[30] E. Wilson, D. W. Sutter, D. Berkovitz, B. J. Betts, R. del Mundo, E. Kong, C. R. Lages, R. Mah, R. Papasin, "Motion-based System Identification and Fault Detection and Isolation Technologies for Thruster Controlled Spacecraft", *Proceedings of the JANNAF 3rd Modeling and Simulation Joint Subcommittee Meeting* , 2005.

[31] A. Barua, "A fault-tree Approach for Identifying Causes of Actuator Failure in Attitude Control Subsystem of Space Vehicles", *Msc Thesis, Concordia University*, 2004.

[32] A. Valdes, "Dynamic Neural Network-based Pulsed Plasma Thruster (PPT) Fault Detection and Isolation for the Attitude Control Subsystem of Formation Flying Satellites", *Master Thesis, Concordia University*, 2008.

[33] S. Simani, C. Fantuzzi, R. J. Patton, "Model-based Fault Diagnosis in Dynamic Systems using Identification Techniques", *Springer*, 2003.

[34] M. A. Massoumnia, "A Geometric Approach to the Synthesis of Failure Detection Filters", *IEEE Trans. Autom. Control*, Vol. 31, No. 9, pages 839 – 846, 1986

[35] R. K. Douglas, J. L. Speyer, "Robust Fault Detection Filter Design", *Proceedings of the American Control Conference*, pages 91 – 96, 1995.

[36] R. K. Douglas, J. L. Speyer, "H_∞ BoundedFault Detection Filter", *AIAA Journal of Guidance, Control, and Dynamics*, Vol. 22, No. 1 pages 129 – 138, 1999.

[37] R. H. Chen, D. L. Mingori, J. L. Speyer, "Optimal Stochastic Fault Detection Filter", *Automatica*, Vol. 39, No. 3, pages 377−390, 2003.

[38] R. H. Chen, J. L. Speyer, "A Generalized Least-squares Fault Detection Filter", *International Journal of Adaptive Control and Signal Processing*, pages 747 – 757, 2000.

[39] R. H. Chen, J. L. Speyer, "Robust Multiple-fault Detection Filter", *International Journal of Robust and Nonlinear Control*, Vol. 12, No. 8, pages 675 – 696, 2002.

[40] J. H. Park, G. Rizzoni, "A New Interpretation of the Fault-detection Filter, 1: Closed-form Algorithm", *International Journal of Control*, Vol. 60, No. 5, pages 767 – 787, 1994.

[41] J. H. Park, G. Rizzoni, W. B. Ribbens, "On the Representation of Sensor Faults in Fault-detection Filters", *Automatica*, Vol. 30, No. 11, pages 1793 − 1795, 1994.

[42] M. Basseville, I. V. Nikiforov, "Detection of Abrupt Changes: Theory and Application", *Information and System Science, Prentice-Hall, New York*, 1993.

[43] L. Berec, "A Multi-model Method to Fault Detection and Diagnosis: Bayesian Solution. an Introductory Treatise", *Int. J. of Adaptive Contr. and Signal Processing*, Vol. 44, No. 6, pages 1009−1016, 1998.

[44] S. G. Tzafestas, K. Watanabe, "Modern Approaches to System/Sensor Fault Detection and Diagnosis", *Journal A. IRCU Lab*, Vol. 31, No. 4, pages 42 − 57, 1990.

[45] J. Chen, H. Y. Zhang, "Parity Vector Approach for Detecting Failures in Dynamic Systems", *Int. J. Sys. Sci.*, Vol. 21, No. 4, pages 765 − 770, 1990.

[46] J. Gertler, "Fault Detection and Isolation using Parity Relations", *Control Engineering Practice*, Vol. 5, No. 5, pages 653 − 661, 1997.

[47] J. J. Gertler, "Fault Detection and Diagnosis in Engineering Systems", *Marcel Dekker, New York/Basel/Hong Kong*, 1998.

[48] J. F. Magni, P. Mouyon, "On Residual Generation by Observer and Parity Space Approaches", *IEEE Trans. Autom. Control*, Vol. 39, No. 2, pages 441 − 447, 1994.

[49] R. J. Patton, P. M. Frank, R. N. Clark, "Fault Diagnosis in Dynamic Systems, Theory and Applications", *Control Engineering series, Prentice-Hall, New York*, 1989.

[50] R. J. Patton, P. M. Frank, R. N. Clark, "Issues of Fault Diagnosis for Dynamic Systems", *Springer-Verlog, London*, 2000.

[51] J. Chen, R. J. Patton, "Robust Model-based Fault Diagnosis for Dynamic Systems", *Kluwer Academic Publishers, Boston/Dordrecht/London*, 1999.

[52] R. Isermann, "Process Fault Detection Based on Modeling and Estimation Methods: A Survey", *Automatica*, Vol. 20, No. 4, pages $387 - 404$, 1984.

[53] P. M. Frank, "Fault Diagnosis in Dynamics System using Analytical and Knowledgebased Redundancy- A survey and some new results", *Automatica*, Vol. 26, No. 3, pages $459 - 474$, 1990.

[54] C. Edwards, S. K. Spurgeon, and R. J. Patton, "Sliding Mode Observers for Fault Detection and Isolation", *Automatica*, Vol. 36, No. 4, pages $541 - 553$, 2000.

[55] B. Jiang, M. Staroswiecki, V. Cocquempot, "Fault Estimation in Nonlinear Uncertain Systems using Robust/Sliding-mode Observers", *IEE Proceedings on Control Theory Application*, pages 2937, 2004.

[56] X. Yan, C. Edwards, "Nonlinear Robust Fault Reconstruction and Estimation using a Sliding Mode Observer", *Automatica*, Vol. 43, No. 9, pages $1605 - 1614$, 2007.

[57] H. Yang, M. Saif, "Nonlinear Adaptive Observer Design for Fault Detection", *Proceedings of the American Control Conference*, pages $1136 - 1139$, 1995.

[58] W. Chen, M. Saif, "A Sliding Mode Observer-based Strategy for Fault Detection, Isolation, and Estimation in a Class of Lipschitz

Nonlinear Systems", *International Journal of Systems Science*, Vol. 38, No. 12, pages 943 – 955, 2007.

[59] V. Venkatasubramanian, R. Rengaswamy, K. Yin, S. Kavuri, "A Review of Process fault Detection and Diagnosis-Part I: Qualitative Model Baed Methods, "*Computer & Chemical Engineering*, Vol. 27, No. 3, pages 293 – 313, 2003.

[60] V. Venkatasubramanian, R. Rengaswamy, K. Yin, S. Kavuri, "A Review of Process Fault Detection and Diagnosis-Part II: Qualitative Models and Search Strategies", *Computer & Chemical Engineering*, Vol. 27, No. 3, pages 313 – 326, 2003.

[61] V. Venkatasubramanian, R. Rengaswamy, K. Yin, S. Kavuri, "A Review of Process Fault Detection and Diagnosis-Part III: Process History Based Methods", *Computer & Chemical Engineering*, Vol. 27, No. 3, pages 327 – 346, 2003.

[62] P. Frank, B. Koppen-Seliger, "Fuzzy Logic and Neural Network Application to Fault Diagnosis", *Automatica*, Vol. 1, pages 67 – 88, 1997.

[63] R. Patton, F. Uppal, C. Lopez-Toribio, "Soft Computing Approaches to Fault Diagnosis for Dynamic Systems: A survey", *4th IFAC Symposium on Fault Detection Supervision and Safety for Technical Process*, Budapest, Vol. 1, pages 298 – 311, 2000.

[64] S. Leonhardt, M.Ayoubi, "Methods of Fault Diagnosis", *Control Engineering Practice*, Vol. 5, No. 5, pages 683 – 692, 1997.

[65] K. Narendra, K. Parthasarathy, "Identification and Control of Dynamical Systems using Neural Networks", *IEEE Trans. Neural Network*, Vol. 1, pages 4 – 27. 1990.

[66] A. Yazdizadeh, K. Khorasani, "Nonlinear System Identification using Embeded Dynamic Neural Network Structures", *IEEE International Joint Conference on World Congress on Computational Intelligence*, Vol. 1, pages 378 − 383, 1998.

[67] T. Sorsa, H. Koivo, "Application of Artificial Neural Network in Process Fault Diagnosis", *Automatica*, pages 843 − 849, 1993.

[68] A. Alesandri, "Fault Diagnosis for Nonlinear Systems using a Bank of Neural Estimators", *Computers in Industry*, Vol. 52, No. 3, pages 271 − 289, 2003.

[69] M. Ayoubi, "Nonlinear Dynamic Systems Identification with Dynamic Neural Networks for Fault Diagnosis in Technical Processes", *IEEE International Conference on System, Man and Cybernetics, Humans, Information and Technology*, Vol. 3, pages 2120 − 2125, 1994.

[70] A. Yazdizadeh, K. Khorasani, "Adaptive Time Delay Neural Network Structures for Nonlinear System Identification", *Neurocomputing*, Vol.47, pages 207 − 240, 2002.

[71] A. Yazdizadeh, K. Khorasani, "Identification of a Class of Nonlinear Systems using Dynamic Neural Network Structures", *IEEE International Joint Conference on Neural Networks*, Vol. 1, pages 194 − 198, 1997.

[72] R. Hornero, D. E. Abasolo, P. Espino, "The Use of Wavelet Entropy to Compare the EEG Background Activity of Epileptic Patients and Control Subjects", *Proceedings of 7th Int Symposium on Signal Processingand Its Applications*, vol. 2, pages 5 − 8, 2003

[73] Z. Y. He, S. B. Gao, X. Q. Chen, J. Zhang, Z. Q. Bo., Q. Qian, "Study of a New Method for Power System Transients Classifica-

tion Based on Wavelet Entropy and Neural Network", *Int. J. Elect. Power*,pages 402 – 410, 2011.

[74] T. Jayasree, D. Devaraj, R. Sukanesh, "Classification of Transients using Wavelet Based Entropy and Radial Basis Neural Networks", *International Journal of Computer and Electrical Engineering* Vol. 1, No. 5, pages 1793 – 8163, 2009.

[75] B. Yu, D. Liu, T. Zhang, "Fault Diagnosis for Micro-Gas Turbine Engine Sensors via Wavelet Entropy", *Journal of Sensors* Vol. 11, No. 10, pages 9928 – 9941.

[76] L. Guo, D. Rivero, J. Seoane, A. Pazos, "Classification of EEG Signals using Relative Wavelet Energy and Artificial Neural Networks", *Proceedings of the first ACM/SIGEVO Summit on Genetic and Evolutionary Computation*, pages 177 – 184, 2009.

[77] E. K. Lada, J. C. Lu, J. R. Wilson, "A Wavelet-based Procedure for Process Fault Detection", *IEEE Trans. on Semiconductor Manufacturing*, Vol. 15, No. 1, pages 79 – 90, 2002.

[78] D. Chanda, N. K. Kishore, A. K. Sinha, "Application of Wavelet Multiresolution Analysis for Identification and Classification of Faults on Transmission Lines", *Electric Power Systems Research*, Vol. 73, No. 3, pages 323 – 333, 2005.

[79] N. Venkateswaran, M. S. Silva, P. S. Goel, "Analytical Redundancy Based Fault Detection of Gyroscopes in Spacecraft Applications", *International Astronautical Federation, Acta Astronautica*, Vol. 50, No 9, pages 535 – 545, 2002.

[80] E. C. Larson, B. E. Parker, B. R. Clark, "Model-Based Sensor and Actuator Fault Detection and Isolation", *Proceedings of the American Control Conference*, 2002.

[81] T. Yairi, Y. Kawahara, R. Fujimaki, Y. Sato, K. Machida, "Telemetry-mining: A Machine Learning Approach to Anomaly Detection and Fault Diagnosis for Space Systems", *2nd IEEE International Conference on Space Mission Challenges for Information Technology*, 2006.

[82] E. Wilson, D. W. Sutter, D. Berkovitz, B. J. Betts, R. del Mundo, E. Kong, C. R. Lages, R. Mah, R. Papasin, "Motion-based System Identification and Fault Detection and Isolation Technologies for Thruster Controlled Spacecraft", *Proceedings of the JANNAF 3rd Modeling and Simulation Joint Subcommittee Meeting*, 2005.

[83] A. Barua, "A Fault-tree Approach for Identifying Causes of Actuator Failure in Attitude Control Subsystem of Space Vehicles", *Msc Thesis, Concordia University*, 2004.

[84] C. Zhao-hui, W. Jiao-long, J. Rui, L. Xiong, "Real-time Fault Diagnosis of Satellite Attitude Control System Based on Sliding-Window Wavelet and DRNN", *IEEE Control and Decision Conference (CCDC)*, pages 1218-1222, 2010.

[85] Z. Li, "Fault Detection and Isolation in Reaction Wheels by Using Neural Network Observers", *Msc Thesis, Concordia University*, 2005.

[86] S. Zhao, "A Recurrent Adaptive Time Delay Neural Network For Fault Detection and Isolation For the Satellite Attitude Control System", *Msc Thesis, Concordia University*, 2007.

[87] O. Durou, V. Godet, L. Mangane, D. Perarnaud, R. Roques, "Hierarchical Fault Detection, Isolation and Recovery Applied to COF and ATV Avionics", *Acta Astronautica*, Vol.50, No 9, pages. 547 – 556, 2002.

[88] J. R. Wertz, W. J. Larson, "Space Mission Analysis and Design", *Kluwer academic publishers*, 1999.

[89] P. C. Hughes, "Spacecraft Attitude Dynamics", *John Wiley & Sons*, 1961.

[90] J. R. Wertz, "Spacecraft Attitude Determination and Control", *D.Reidel Publishing Co.*,1980.

[91] W. Ren, R. W. Beard, "Distributed Consensus in Multi-vehicle Cooperative Control", *Sringer*, 2008.

[92] B. Bialke, "High Fidelity Mathematical Modeling of Reaction Wheel Performance", *21st Annual American Astronautical Society Guidance and Control Conference*, pages $483 - 496$, 1998.

[93] Z. Y. He, X. Q. Chen, G. M. Luo, "Wavelet Entropy Definition and Its Application for Transmission fault Detection and Identification (Part I: Definition and Methodology)", *Proceedings of International Conference on Power System Technology, Chongqing*, pages $1 - 5$, 2006.

[94] S. Mallat, "A Theory for Multiresolution Signal Decomposition: The Wavelet Representation", *IEEE Trans. Pattern Anal. Mach. Intell.* , Vol. 11, No. 7, pages $673 - 693$, 1989.

[95] K. T. Alfriend, S. R. Vadali, P. Gurfil, J. P. How, L. S. Breger, "Spacecraft Formation Flying: Dynamics, Control and Navigation", *Elsevier Astrodynamics Series,* 2010.

[96] J. K. Eyer, "A Dynamics and Control Algorithm for Low Earth Orbit Precision Formation Flying Satellites", *PhD thesis, University of Toronto*, 2009.

[97] http://sci.esa.int/science-e/www/area/index.cfm?fareaid=8

[98] http://www.csr.utexas.edu/grace/

[99] http://www.lsespace.com/?sid=9028

[100] http://www.esa.int/Our_Activities/Technology/Proba_Missions/Proba-3_precision_formation-flyer_takes_next_step_to_space

[101] http://lisa.nasa.gov/

[102] http://mms.gsfc.nasa.gov/

[103] http://hires.gsfc.nasa.gov/si/

[104] http://asd.gsfc.nasa.gov/Gerald.Skinner/massim_proposal.pdf

[105] http://maxim.gsfc.nasa.gov/

[106] "Computer Science 831: Knowledge Discovery in Databases", http://www2.cs.uregina.ca/ dbd/cs831/notes/confusion matrix/confusion matrix.html

[107] C. K. Chui, "Wavelets: A Mathematical Tool for Signal Analysis", *SIAM*, 1997.

[108] O. Durou, V. Godet, L. Mangane, D. Perarnaud, R. Roques, "Hierarchical Fault Detection, Isolation and Recovery Applied to COF and ATV Avionics", *Acta Astronautica*, Vol. 50, No. 9, pages $547 - 556$, 2002.

[109] A. Joshi, V. Gavriloiu, A. Barua, A. Garabedian, P. Sinha, K. Khorasani, "Intelligent and Learning-based Approaches for Health Monitoring and Fault Diagnosis of RADARSAT-1 Attitude Control System", *IEEE International Conference on System, Man and Cybernetics ISIC*, October 2007.

[110] M. Lavagna, G. Sangiovanni, A. Da Costa, "Modelization, Failures Identification and High-level Recovery in Fast Varying Non-linear

Dynamical Systems for Space Autonomy", *6th International Conference on Dynamics and Control of Systems and Structures in Space,* July 2004.

[111] A. M. Salkham, "Fault Detection, Isolation and Recovery (FDIR) in On-Board Software", *Master's Thesis, Department of Computer Science and Engineering,* Chalmers University of Technology, 2005.

[112] A. Guiotto, A. Martelli, C. Paccagnini, "SMART-FDIR: Use of Artificial Intelligence in the Implementation of a Satellite FDIR", *Data Systems in Aerospace DASIA 2003*, June 2003.

[113] N. Holsti, M. Paakko, "Towards Advanced FDIR Components", *Proceedings of the DASIA 2001 Conference*, June 2001.

[114] P. S. Morgan, "Fault Protection Techniques in JPL Spacecraft", *International Forum on Integrated System Health Engineering and Management in Aerospace ISHEM,* November 2005.

[115] J. R. Carnes, A. Misra, "Model-Integrated Toolset for Fault Detection, Isolation and Recovery (FDIR)", *IEEE Symposium and Workshop on Engineering of Computer-Based Systems*, March 1996.

[116] I. Daubechies, "Ten Lectures on Wavelets", *SIAM*, 1992.

[117] N. Meskin, K. Khorasani, "Fault Detection and Isolation: Multi-Vehicle Unmanned Systems", *Springer*, 2011.

[118] http://celestrak.com/columns/v02n01/

[119] S. Mohammed et al., "Simulation of Microsatellite Attitude using Kalman Filtering in Orbit Results", *Simulation Modelling Practice and Theory*, Vol. 16, Issue 3, pages 257 – 277, March 2008.

[120] T. Höfling, R. Isermann, "Fault Detection Based on Adaptive Parity Equations and Single-parameter Tracking", *Control Engineering Practice*, Vol. 4, No. 10, pages 1361 – 1369, 1996.